NUMERICAL MODELING AND EXPERIMENTAL INVESTIGATION OF MASONRY STRUCTURES

by

FEI ZENG

A dissertation submitted to the Graduate Faculty in Civil Engineering
in partial fulfillment of the requirements for the degree of
Doctor of Philosophy, The City University of New York

2010

Approval Sheet

This manuscript has been read and accepted for the

Graduate faculty in Engineering in satisfaction of the

dissertation requirements for the degree of Doctor of Philosophy.

Date

Professor Feng-Bao Lin
Chair of Examining Committee

Date

Dean Mumtaz K. Kassir
Executive Officer

Supervisory Committee:

Professor Anil Kumar Agrawal

Professor Kolluru V. Subramaniam

Professor Huabei Liu

Professor Benjamin Liaw

THE CITY UNIVERSITY OF NEW YORK

Acknowledgments

I would like to thank Professor Feng-Bao Lin, for his guidance and support throughout the entire work. This work would have been impossible to be complete without his help.

I also want to thank Professor Michel Ghosn for carefully following my work and providing lots of invaluable suggestion. I am grateful to Professor Kolluru V. Subramaniam for the tremendous help in experimental techniques and approaches. The comments from the members of the examining committee: Professors Anil Kumar Agrawal, Huabei Liu, and Benjamin Liaw are also gratefully appreciated.

I would like to express my thanks to my colleagues Xiaojun Wang, Mohamad Ali-Ahmad, Tarendra Lakhankar, Zhou Xu, MingDong Bi, Zhihua Yi and Weimin, Nian, at City College of New York for all the discussions and cooperation. Special thanks go to Hadi Kamyab for the help with the experimental setup and ensuring that my experiments were never delayed. Thanks also go to Professor Marek-Jerzy Pindera and Dr. Linfeng Chen at University of Virginia for the help with developing the FVDAM model. Partial financial support from CUNY Collaborative Research Program Grant No. 80209-0211 is also acknowledged.

I am very grateful for the help and encouragement of my parents, brothers and in laws.

Last but not least, I would like to express my loving gratitude to my wife, Fen, for her patience, understanding and support throughout this study, and to my daughter, Janice, who is a never-ending source of love, pride and inspiration to me.

Abstract

NUMERICAL MODELING AND EXPERIMENTAL INVESTIGATION
OF MANSONRY STRUCTURES

by

Fei Zeng

Advisor: Professor Feng-Bao Lin

The need of structural rehabilitation and strengthening of masonry structures motivated this study to better understand the deformation and failure mechanism of masonry structures. Although the behavior of masonry under uniaxial and biaxial compressive loading has been investigated by many researchers, experimental studies on how the crack propagates in the masonry are rarely seen in the literature. In this study, quantitative measures of strain localization in masonry are presented for the first time in both deformation and failure modes by using an in-situ optical technique called Digital Image Correlation (DIC). It was found that cracks initiated and propagated through the mortar joints; and finally the stone unit split, which is due to the action of biaxial tension in the stone unit when masonry specimen is compressed. Two stage modeling strategy was adopted to model the seismic behavior of large-scale masonry structure. First, homogeneous equivalent material properties are obtained by using micro-modeling approaches. Then, the equivalent material properties are used to macro-model the seismic behavior of the large scale masonry structure with the finite element software ABAQUS. Elasto-plastic analyses were carried out on the granite masonry structure to compare with experimental results. The well experimental-analytical correlation confirmed the capability of the FVDAM model in predicting the response of masonry structure if the individual mechanical behavior of its constituents (i.e., unit and mortar) is known. Extensive parametric analysis was performed to understand the effect of the mesh size, cell texture, mortar elastic modulus and mortar volume fraction on the equivalent elastic properties. Finally, the obtained homogeneous equivalent material properties were used to seismic assessment of the masonry tower of the Brooklyn Bridge. It was found that the whole tower can retain global structural stability but extensive damages appear in the arch-base connection regions under the design earthquake excitation.

Table of Contents

List of Figures

List of Tables

Chapter 1: Introduction

1.1 Background

Masonry is composed of two very different materials, masonry units (stone, bricks, or blocks) and cement mortar. As one of the oldest building materials, masonry was not only used in many magnificent historical structures all over the world but is still used in various new constructions. The need of structural rehabilitation and strengthening of ancient masonry structures motivated studies to better understand the deformation and failure mechanism of masonry structures. Unreinforced masonry structures are particularly vulnerable to earthquake excitations due to the fact that the integrity of these structures relies mainly on the joining material between masonry blocks which is apt to crack when subjected to tension caused by earthquake lateral forces. The recent earthquakes in various countries have caused great damage and destruction to masonry bridges, religious temples, and other monumental buildings. Some example of the collapse of masonry building and churches after an earthquake are shown in Figure 1.1 (Klingner and Ferguson 2006). In the North America, the 1994 Northridge Earthquake has revealed that the masonry structures experienced the worst damage during the earthquake. Past earthquakes have also revealed that the collapse of masonry structures is responsible for more than 80% of the casualties during these events (Meguro, Uehan et al. 2004). These incidents further enlightened the need to have a better understanding of the behavior of masonry structure through experimental and numerical studies.

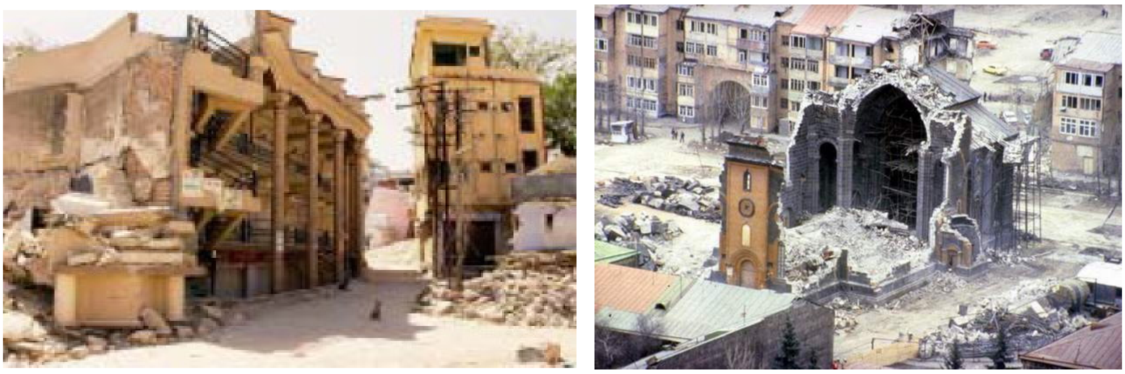

Figure 1.1: Collapse of masonry buildings and churches during the earthquake

The practical motivation for this research is from the project about seismic assessment and retrofitting of the East River Bridges, which was initiated by the New York City Department of Transportation (NYCDOT). In the City of New York, lots of unreinforced masonry structures can be seen in many existing bridges, ranging from the towers of long-span bridges such as the Brooklyn Bridge to the piers of short-span bridges such as 145th street Bridge in Manhattan (see Figure 1.2). New York City Department of Transportation owns about 750 bridges among a total of more than 2,100 bridges in the city. Soon after the 1989 Loma Prieta earthquake in San Francisco, many states in the central and eastern United States including New York adopted provisions for seismic design of highway bridges. Most of the bridges in New York City were built before the seismic requirements for the city were implemented. To fulfill these later adopted seismic requirements, the existing bridges must be evaluated and it is predictable that most of these bridges have to be retrofitted for seismic resistance enhancement. The practical need motivated this research work to perform experimental investigation of masonry structure and develop appropriate numerical model to predict the seismic performance of masonry structure.

Figure 1.2: The Brooklyn Bridge with unreinforced masonry tower (left) and the 145th street Bridge in Manhattan with masonry piers (right)

As so far, the behavior of masonry under uniaxial and biaxial compressive loading has also been investigated by a number of researchers (Hilsdorf 1969; Page 1981; Dhanasekar, Page et al. 1985; Binda, Mirabella et al. 1996; Roca, Oliveira et al. 2001; Sarangapani, Reddy et al. 2005). However, experimental studies on how the crack evolution and propagation in the masonry are rarely seen in the literature. In this study, the technique of Digital Image Correlation (Sutton, Wolters et al. 1983; Sutton, Cheng et al. 1986) is used to quantitatively construct the full-field strain maps of masonry specimens at various loading increments. The experimental investigation, which includes uniaxial compression test, vibrational resonance frequency test, and digital image correlation test, was performed on the granite masonry as well as its constituent components, granite stone units and cement mortar.

In spite of the simplicity associated with building in masonry, the analysis of the mechanical behavior of masonry constructions remains a true challenge. Masonry is a heterogeneous medium which shows an inhomogeneous nature. The inhomogeneity is due to the different mechanical properties of its constituents, mortar and block unit; and the different masonry patterns since the mechanical response is affected by the geometrical arrangement of the constituents.

Basically, two different approaches have been used to model the masonry behavior: the “micro-modeling” and the “macro-modelling” or ‘equivalent-material approach’. Selection of the approach depends upon the level of accuracy and the objective sought. The former approach models the actual geometry of both the blocks and mortar joints, adopting different constitutive models for the two components. Although this approach may appear very straightforward, its major disadvantage comes from the extremely large number of elements are required and the requirement of knowing the precise layout of each brick. A three-dimensional micro-modeling analysis of a masonry panel with only a very simple geometry would require a large number of elements in order to enable accurate modeling of each joint and block unit. Hence, the use of micro-models is impossible / impractical for the global analysis of entire buildings or bridges. In addition, the actual distribution of blocks and joints might be impossible to detect unless many investigations are performed.

To overcome this computational difficulty, the macro-modeling approach, in which masonry is modeled by an equivalent continuous material, is used for structural analysis. The macro-models do not make a distinction between individual blocks and mortar joints, smearing the effect of joint presence through the formulation of the constitutive relations of an equivalent material. Such a constitutive model has to reproduce an average mechanical behavior of small masonry panel. The main advantages of the macro approach are the enormous reduction of the computational cost, which makes possible the numerical analyses of complex structures such as bridges and buildings. The macro approach makes it feasible to analyze any masonry structure without detailed knowledge of the layout of individual bricks.

Based on the above comparison for the both micro-modeling and macro-modeling approaches, a two stage modeling strategy is suitable for analyzing the seismic behavior of large-scale masonry structure in this study. First, homogeneous equivalent material properties are obtained by using micro-modeling approaches. Specifically, the micromechanics model called Finite-Volume Direct Averaging Micromechanics (FVDAM) will be used to achieve the equivalent continuous material for small masonry panel. Then, the equivalent material properties are used to macro-model the seismic behavior of the large scale masonry structure such as the tower of the Brooklyn Bridge with the commercially available FEM software ABAQUS. Once the critical region is identified by the macro-modeling and local detail micro model can be established to

1.2 Objectives

The primary intent of this study is to have a better understanding of the behavior of the two-phase masonry material through experimental and numerical studies. The main objectives of this thesis are:

- Characterize the compressive behavior of the masonry materials and examine the effects of granite units and cement mortar on the strength and elastic constants of the granite masonry.
- Develop an appropriate plastic numerical algorithm based on the micromechanics-based FVDAM model for elasto-plastic analysis of Mohr-Coulomb material.

- Examine the predictability of the FVDAM model by comparing the predicted numerical -response with the behavior measured in experiments.
- Perform parametric analysis to understand the effect of the mesh size, cell texture, mortar elastic modulus and mortar volume fraction on the homogenized/effective elastic properties
- Make a seismic assessment of large-scale masonry structure using macro-modeling strategy and provide the retrofitted scheme for seismic renovation for masonry structure.

1.3 Outline

This dissertation presents an experimental and numerical study of the masonry structure. This study involves: (a) a review of the literature on the experimental and numerical analysis; (b) an experimental investigation of granite masonry structure under uniaxial compression; (c) development of a micromechanics-based model to simulate the elastic-plastic behavior of masonry structure; and (d) the macro FEM analysis of masonry structures under seismic excitation. The general description of the dissertation is summarized in the following:

In Chapter 1, an introduction and research objectives, scope and outline of the research was provided.

In Chapter 2, a general overview about the experimental and numerical analysis of masonry structures is given. The different modeling strategies including micro and macro modeling are also discussed.

In Chapter 3, experimental results on granite masonry specimens were presented.

The adopted procedure for testing is described and the experimental results are discussed in detail. By using an in-situ optical technique called Digital Image Correlation, quantitative measurements of strain evolution of granite masonry are achieved in both deformation and failure modes for the first time.

In Chapter 4, a new plastic algorithm based on the Mohr-Coulomb failure criterion was developed in the FVDAM model to simulate the constituents of the masonry, i.e., cement mortar and granite unit, by updating the corresponding plastic strain increment during the different loading stages. The FVDAM theory is first validated through comparison with finite-element results, demonstrating that FVDAM can predict macroscopic behavior of composite material and local stress fields with accuracy approaching that of the finite-element method. Then the FVDAM model was applied to masonry structure and the extensive parametric analysis was performed to understand the effect of the mesh size, cell texture, mortar elastic modulus and mortar volume fraction on the homogenized/effective elastic properties Finally, elastic-plastic analyses were carried out on the granite masonry structure to compare with the experimental results.

In Chapter 5, Large-scale masonry structure, i.e., unreinforced masonry tower of the Brooklyn Bridge, was macro modeled as a homogeneous material and its seismic behavior was investigated using the Finite Element software ABAQUS. Modal analysis and the nonlinear time-history analysis were performed on the masonry tower with the seismic ground motions represented by three different historical earthquake records. The tower drift under the design seismic excitation was also determined to compare with the requirement of the code for seismic performance design objective.

In Chapter 6, the major and specific conclusions obtained from the experimental as well as modeling studies are included.

Chapter 2: Literature Review

2.1. Introduction

Masonry is the oldest building material that is still currently used in the building industry. Masonry is a heterogeneous material composed of units and mortar joints. Irregular stones, ashlars, adobes, bricks and blocks have been used as units. The units can be joined together using mortar (commonly clay, lime or cement based mortar) or just by simple superposition. With these two components, a large number of arrangements can be accomplished, generated from the different combinations of units and joints. A possible classification of stone masonry is shown in Figure 2. 1 and the most used combinations are illustrated in Figure 2. 2.

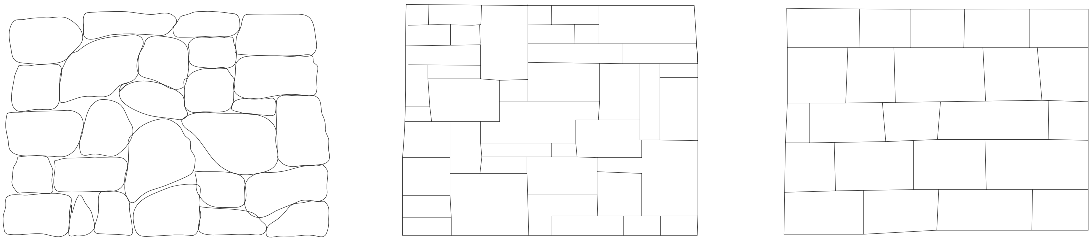

(a) (b) (c)

Figure 2.1: Different kinds of stone masonry: (a) rubble masonry; (b) ashlar masonry; (c) coursed ashlar masonry (Lourenço, 1998).

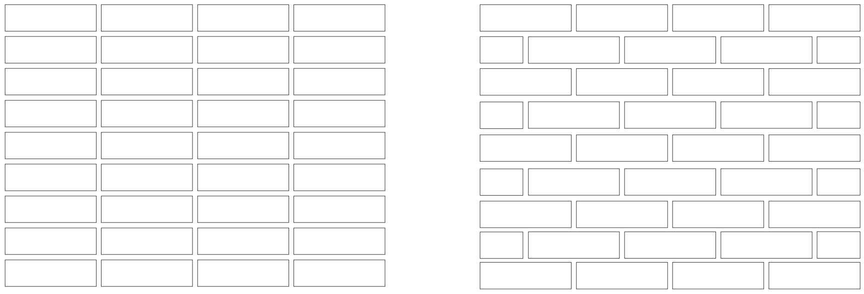

(a) (b)

Figure 2.2: Different arrangements for brick masonry: (a) stack bond; (b) stretcher bond

Achieving good characterization of ancient structures and materials is a very demanding task, both in time and cost. On the one hand, the possibility of performing non-destructive and minor destructive tests is very interesting since it allows one to obtain valuable data. Unfortunately it does not provide enough information about the characterization of the structural material required by advanced modelling. On the other hand, the feasibility of performing destructive tests on ancient constructions, either in-situ or by removing samples large enough to be representative may be seen almost as an idealistic hypothesis since it is most of the times not possible. So, usually the option is to carry out laboratory tests on masonry specimens representative of real constructions. However, this possibility turns out to be very complicated due to the enormous variations of masonry and to the impossibility of reproducing all its features in a specimen. Consequently, most of the effort devoted to experimental research in masonry has been directed towards brick and block masonry.

In spite of the simplicity associated with building in masonry, the analysis of the mechanical behavior of masonry constructions remains a true challenge. Masonry is a material that exhibits distinct directional properties due to the mortar joints, which act as planes of weakness. Consequently, masonry structures display shows an anisotropic and inhomogeneous nature. In particular, the inhomogeneity is due to the different mechanical properties of its constituents, mortar and unit. The anisotropy is due to the different masonry patterns since the mechanical response is affected by the geometrical arrangement of the constituents. In general, the approach towards its numerical representation can focus on the micro-modeling of the individual components, i.e., unit (brick, block, etc.) and mortar, or the macro-modeling of masonry as a composite (Rots 1991). Depending on the level of accuracy and the simplicity desired, it is possible to use the following modeling strategies, see Figure 2.3:

- Micro-modeling - units and mortar in the joints are represented by continuum elements.
- Macro-modeling – units and mortar are smeared out in the continuum.

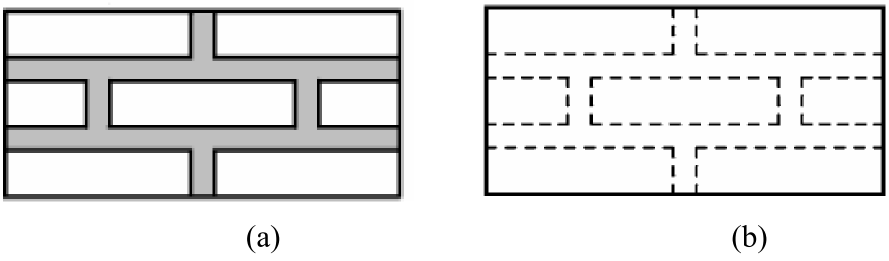
(a) (b)

Figure 2.3: Modeling strategies for masonry structures: (a) detailed micro-modeling; and (b) smeared macro-modeling

In the first approach, Young's modulus, Poisson's ratio and inelastic properties of both unit and mortar are taken into account. Additionally, micromodelling can be accurately used for the calibration of the mechanical parameters of macromodels. The second approach does not make a distinction between individual units and joints but treats masonry as a homogeneous continuum. One modeling strategy cannot be preferred over the other because different application fields exist for micro- and macro-models. Micro-modeling studies are necessary to give a better understanding about the local behavior of masonry structures. The second approach is a phenomenological approach. When the structure has sufficiently large dimensions, macro-models are more practice oriented due to the reduced time and memory requirements as well as a user-friendly mesh generation.

In the following sections, experimental tests capable of providing a comprehensive description of masonry, both in uniaxial and biaxial behaviour, are reviewed first. Then various micro-modeling and macro-modeling techniques are reviewed. Especially, the theoretical development of the FVDAM model proposed by Pindera and Bansal (2005) is reviewed in detail since the FVDAM model will be used to study the elasto-plastic behavior of masonry structure.

2.2 Experimental Research on Masonry Structures

2.2.1 Uniaxial compressive behavior

The uniaxial behaviour, obtained under displacement-controlled tests, is usually characterized by the establishment of a stress-displacement diagram. It is commonly accepted that the uniaxial compressive strength of masonry in the direction normal to the bed joints can be obtained from the so-called RILEM test, see Wesche and Ilantis (1980), shown in Figure 2.4.

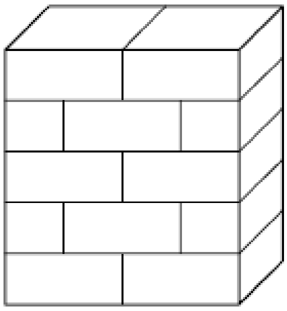

Figure 2.4: Schematic representation of masonry specimen for uniaxial compressive test

Uniaxial compression of masonry leads to a state of triaxial compression in the mortar and of compression/biaxial tension in the unit. The mortar tends to expand laterally more than the units due to their different elastic properties. The continuity between units and mortar creates a lateral confinement to the mortar (Mann and Betzler 1994) observed that, initially, vertical cracks appear in the units along the vertical joint. Upon increasing deformation additional cracks appear and lead to failure by splitting of the prism. Examples of load-displacement diagrams for masonry compressive test are shown in Figure 2.5, where three samples with different mortar compressive strength were plotted in the same figure (Binda, Fontontana et al. 1988). Following the pioneer study of (Hilsdorf 1969), many researchers (e.g. Hendry, Sinha et al. 1981; CEN 1995) have tried to derive a relation between the compressive strength of masonry and the compressive strength of its single components, units and mortar. It has been shown that the behaviour of masonry prisms under uniaxial compressive loading is clearly influenced by both the size of the specimen and the boundary conditions (Vermeltfoort 1997).

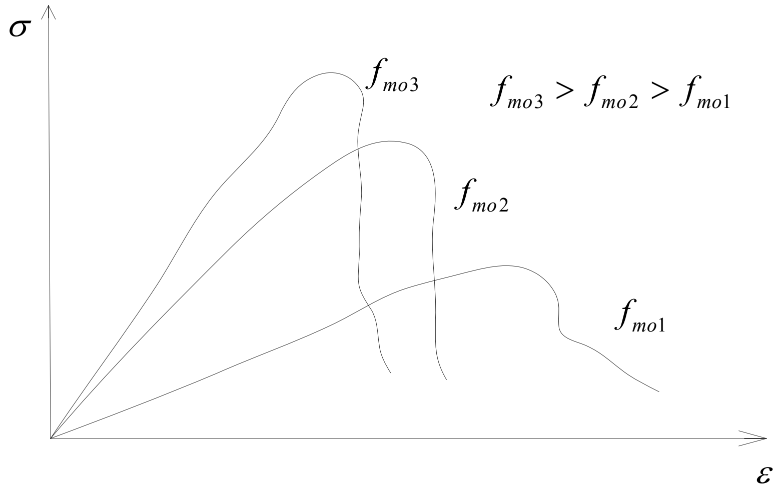

Figure 2.5: Typical experimental stress-displacement diagrams for masonry under uniaxial compressive loading.

2.2.2 Uniaxial tensile behavior

Tensile strength of masonry plays an important role in the failure of the masonry structure. Some researchers have attempted to investigate the true tensile strength of unreinforced masonry. Different types of tests have been used to evaluate the tensile strength. Basically, tensile bond strength tests can be divided into two main categories (Jukes and Riddinton, 1998): direct tensile bond strength tests and flexural bond strength tests, see Figure 2.6 for a schematic representation.

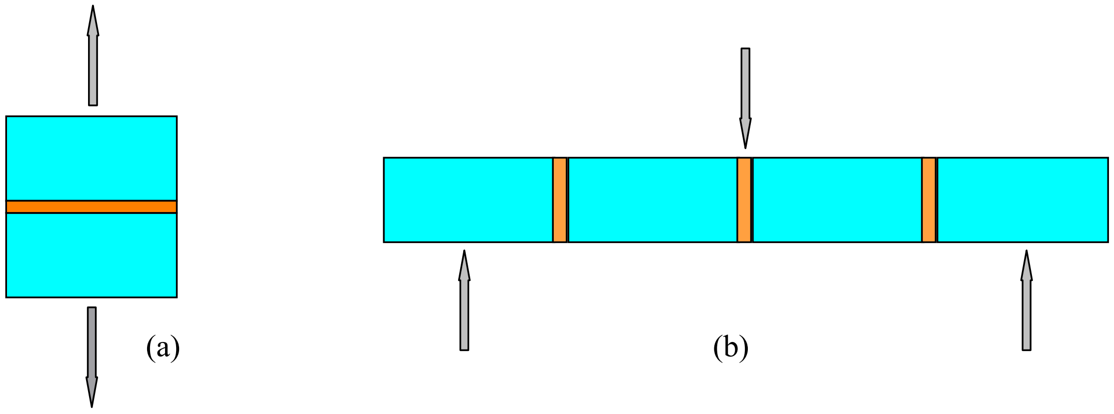

Figure 2.6: Possible bond strength tests: (a) direct tensile bond strength test; (b) flexural bond strength test

In the direct tensile test, it is required that the testing apparatus should be able to apply a uniform stress distribution at the unit- mortar interface, which is not easy to ensure. Flexural tests can also be used to obtain tensile bond strength data. The principle of this approach is to impose bending onto a masonry wallet until failure is achieved. In this way, flexural tests measure the bond strength at the edge of the mortar joint, but the strength at that point may not be representative of the strength of the all joint. Therefore, tensile strength values derived from flexural tests need to be adjusted by a correction factor.

For tensile loading perpendicular to the bed joints, failure is generally caused by failure of the relatively low tensile bond strength between the bed joint and the unit However, tension failure was usually affected by the type of the mortar and the masonry units. For stronger mortar and weaker masonry units the tension cracks passed along the head mortar joints and through the centre of the bricks at the intervening courses as shown in Fig. 2.7(a). For weaker mortar joints and stronger masonry units, the tension crack passed along the head joints of the masonry units and the length of bed joints between staggered head joints as shown in Fig. 2.7(b).

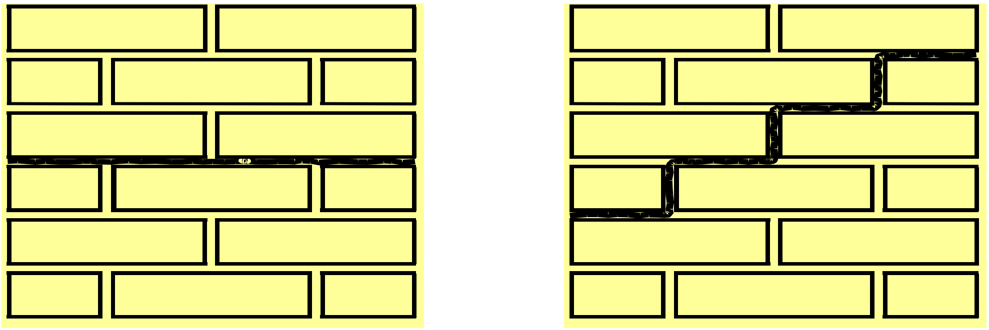

(a) Through type

(b) Zigzag type

Figure 2.7: Modes of tension failure of masonry walls under direct tension (Backes, 1985)

2.2.3 Shear behavior

Shear has been identified as the governing mode of failure in masonry constructions subjected to lateral loads like wind and earthquakes, see e.g. (Mann and Muller 1982). So it is important to understand its shear behavior, bur direct shear tests are very demanding experiments because the test setup should generate a uniform state of stress on the joint. These requisites are very difficult to attain since most of the time the shear load cannot be applied in line with the join and consequently an undesirable overturning moment creates a non- uniform normal stress state in the joint.

Different test methods have been proposed, see (Jukes and Riddington 1997) for a detailed description. The most common test configurations are the direct shear test, or couplet test (two units and one joint), and the triplet test (three units and two joints), see Fig. 2.8.

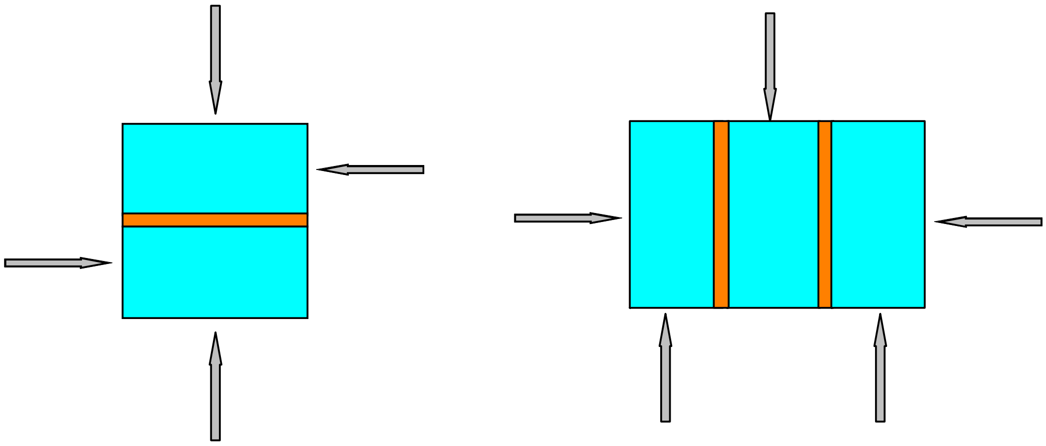

Figure 2.8: Test set- ups for shear loading: (a) couplet test; (b) triplet test

It was observed that the shear strength of the masonry specimen is strongly related to the applied compressive load (see Figure 2.9 for a schematic representation of the results). For lower compressive stresses normal to the joint, the shear strength of the joint t is derived from a combination of bond shear strength (or cohesion) C and friction angle ϕ

between the unit and the mortar, being expressed by the Coulomb friction law:

$$\tau = c + \sigma \tan \phi \qquad (2.1)$$

Where ϕ is the friction angle of the joint.

Besides the strength of mortar, the influence of joint thickness was experimentally detected on the shear strength and failure mechanisms at the unit- mortar interface. Binda et al. (1996b) demonstrated that the shear strength of the specimens decreases with the increase of the joint thickness.

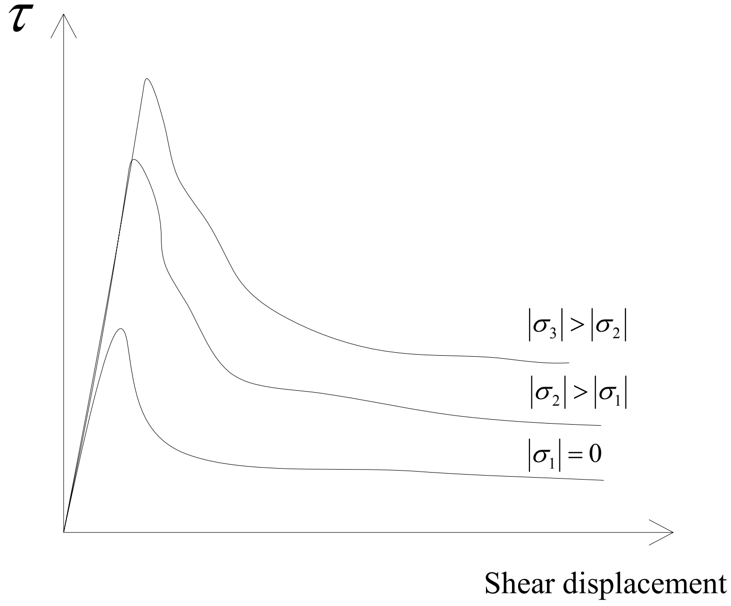

Figure 2.9: Typical experimental shear stress-displacement diagrams

2.2.4 Biaxial behaviour

Since the strength of masonry is highly dependent on the orientation of the principal stresses with respect to the material axes, the constitutive behavior of masonry under biaxial states of stress cannot be completely described from the constitutive behavior under uniaxial loading conditions. Only few attempts were performed to obtain the complete experimental in-plane strength envelope for masonry. The most complete set of experimental data of masonry subjected to proportional biaxial loading is shown in Figure 2.10 (Page 1981; Page 1983). The tests were carried out with half scale solid clay units, submitted to proportional biaxial loading. Both the orientation of the principal stresses with regard to the material axes and the principal stress ratio considerably influence the failure mode and strength. The different modes of failure are illustrated in Figure 2.11. In all uniaxial loading cases, failure was brittle and occurred in planes normal to the panel, by cracking either the mortar joints alone or in a combined mechanism involving both brick and joints. In biaxial compression, failure occurred by splitting of the specimen, in a plane parallel to its free surface, independent of the orientation of the principal stresses. Due to testing complexities, experimental results in the biaxial tension range were not performed.

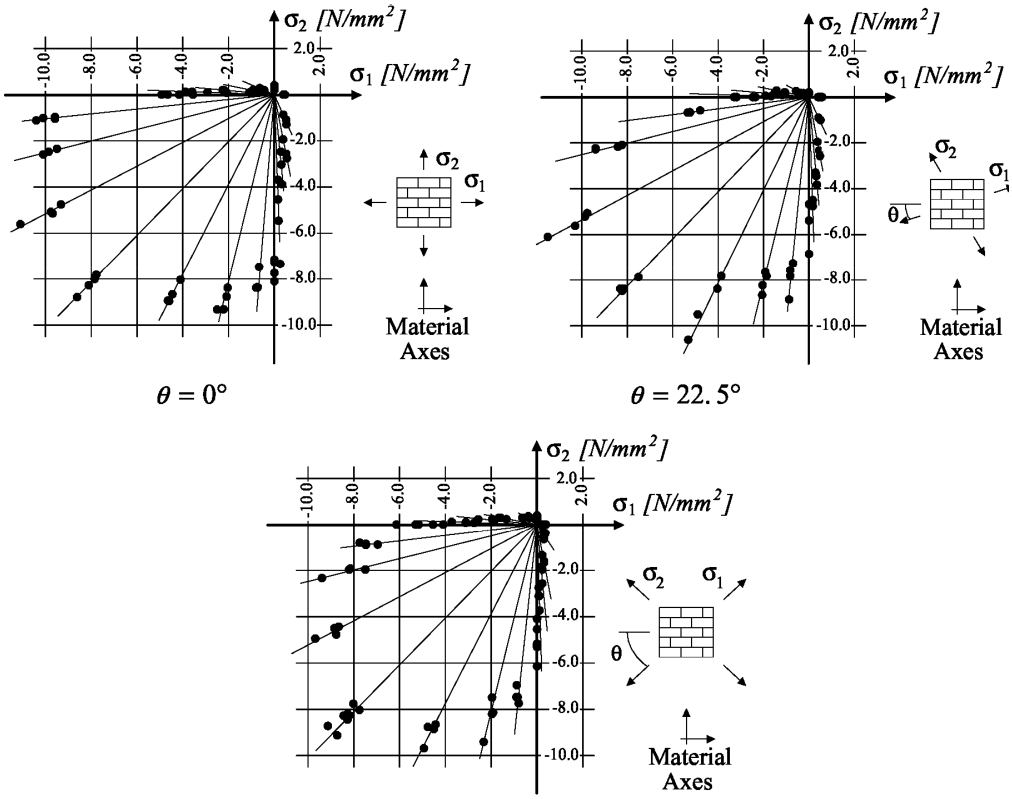

$\theta = 0°$

$\theta = 22.5°$

Figure 2.10: Biaxial strength of solid clay masonry, Page (1981, 1983)

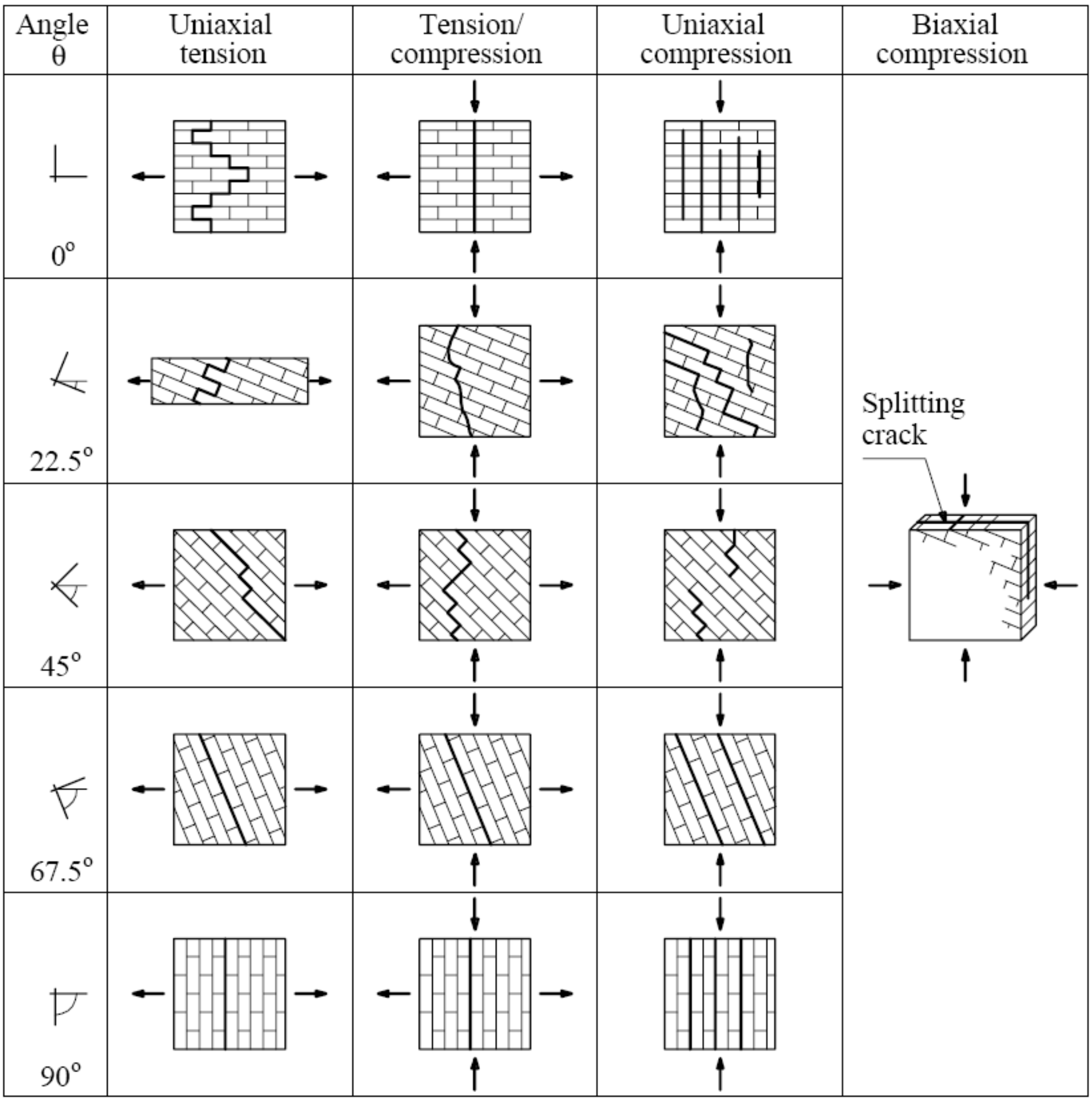

Figure 2.11: Modes of failure of solid cla units masonry under biaxial loading (Dhanasekar et al., 1985)

In addition, it is noted that the biaxial strength envelope obtained by Page (1981, 1983) is of limited applicability for other types of masonry. Most likely, different biaxial strength envelopes and different failure modes may be obtained for different materials, shapes and geometry. A comprehensive program to characterize the biaxial strength of different masonry types has been carried out in Switzerland using full scale specimens, see (Ganz and Thurlimann 1982) for hollow clay units masonry, (Guggisberg and Thurlimann 1987) for clay and calcium-silicate units masonry and (Lurati, Graf et al. 1990) for concrete units masonry.

As shown above, the behavior of masonry under uniaxial and biaxial compressive loading has also been investigated by a number of researchers. However, experimental studies on how the crack evolution and propagation in the masonry are rarely seen in the literature. In this study, the technique of Digital Image Correlation (Sutton, Wolters et al. 1983; Sutton, Cheng et al. 1986) is used to quantitatively construct the full-field strain maps of masonry specimens at various loading increments. These strain maps provide a means to observe crack propagation, strain localization, and failure mechanism of the masonry. The main purposes of this experimental study are to characterize the compressive behavior of the masonry materials, examine the effects of granite units and cement mortar on the strength and elastic constants of the granite masonry, and simultaneously examine the predictability of the FVDAM model on computing the homogenized elastic constants of the masonry from the properties of its constituent components.

2.3. Numerical Modeling of Masonry Structures

2.3.1 Micro modeling

A masonry structure is a two-phase composite medium composed of mortar and unit (stone, brick, or block), normally arranged periodically. For the multiphase composite materials, the homogenisation techniques represent a powerful tool and are getting more and more attention among the masonry community in the last 20 years. The homogenization techniques derive average homogenized properties of masonry from the behaviour of each constitutive material. Usually, three types of approaches have been developed for the micro-modeling of the masonry composites. The first approach is to use a simplified layer geometry to represent the basic cell and so that a close-form solution of the homogenization problem is possible (Pande, Liang et al. 1989; Pietruszczak and Niu 1991). The homogenization has generally been performed in two steps, head (vertical) and bed (horizontal) joints being introduced successively , however its result depends on the sequence of the successive steps (Papa 1996), which means that the procedure is not objective.

The second approach is based on the micromechanics theory and to employ a representative volume element (RVE) to calculate the equivalent elastic constants and failure modes of masonry material with the help of finite element software (Ma, Hao et al. 2001; Wu and Hao 2006). The representative volume element in a composite body is illustrated in Figure 2.12. Both the units and mortar joints are idealized as isotropic material having their own properties such as stiffness, strength, and damage characteristics. Based on the numerical results, the equivalent material properties are used as the homogenized material properties in numerical simulation of a full masonry structure based on the continuum approach. However, the approach is not analytical and relies on the commercially available FEM software. In fact, the plastic behavior for the individual brick and mortar are still not well known very well and lot of scattering have been observed in the mechanical test of masonry specimens. Thus the applicability of the continuum model based on the RVE model is still limited.

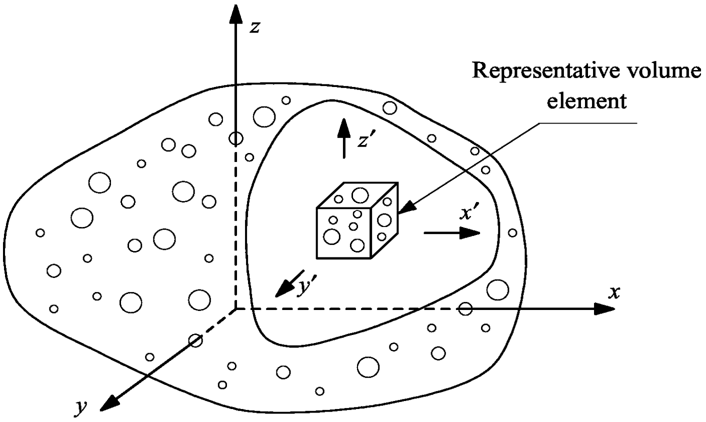

Figure 2.12: Representative volume element (RVE) in a composite body

The third approach is also based on a micromechanics concept, in which a repeating unit cell (RUC) containing all the individual components is employed (Aboudi 1989; Anthoine 1995; Anthoine 1997), see Figure 2.13.

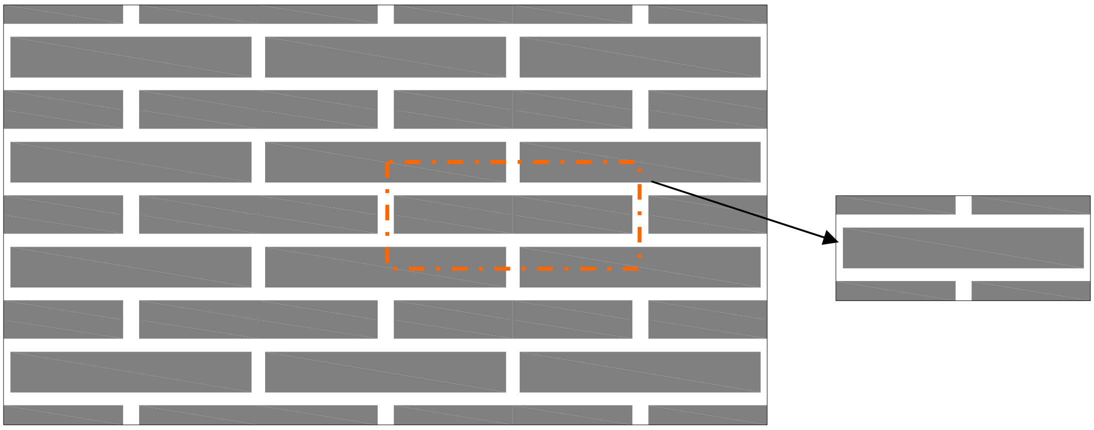

Figure 2.13: Repeating Unit Cell (RUE) in the periodic composite

These two concepts (RVE and RUC) are based on different geometric representations of heterogeneous microstructures and require different boundary conditions in the micromechanical analysis of the smallest material subvolume. In particular, micromechanical analysis of an RVE is based on the homogeneous traction and displacement boundary conditions, while micromechanical analysis of an RUC is based on periodic displacement and traction boundary conditions. Recently, (Bansal and Pindera 2006) reconstructed a micromechanics model called Finite-Volume Direct Averaging Micromechanics (FVDAM), which was developed from the higher-order theory for periodic heterogeneous materials (Aboudi, Asme et al. 2001). The analytical framework of the FVDAM model is based on the local/global stiffness matrix approach and closed-form expressions have been derived. The FVDAM model shares some similarities with the finite-element method, while also possessing distinct differences. The formation of local and global stiffness matrices is common to both approaches. The continuity of displacements and forces imposed at the nodes in the finite-element technique is replaced by the continuity of displacements and tractions imposed at the subcell interfaces in the FVDAM model. The FVDAM model has simplified the theoretical framework and substantially increased its computational efficiency, enabling analysis of unit cells with realistic multiphase microstructures previously unattainable in the original formulation developed by (Aboudi, Asme et al. 2001). The capability of the FVDAM model predicting macroscopic and microscopic response of metal composites such as boron/aluminum composites has also been verified through experimental data (Bansal and Pindera 2006). However, currently the plastic analysis of FVDAM is still limited to the bilinear hardening materials such as metals. In this study, the plastic modeling capacity of the FVDM also has been further extended to the more complex material such as piece-wise continuous materials by updating the corresponding plastic strain increment during the different loading stages. In the following sections, the theoretical development of the FVDAM model will be reviewed in detail since the FVDAM model will be used to study the elasto-plastic behavior of masonry structure in this study. Elastic theory for FVDAM model is introduced in the following section. Plastic theory development for the FVDAM based on the Mohr-Coulomb material failure criteria will be addressed in Chapter 4.

2.3.1.1 FVDAM model

Displacement, stress and strain field

The FVDM model combines concepts from the homogenization theory and the higher-order theory for functionally graded materials. The displacement and strain field of multiphase material are established in the repeating unit cell (RUC) which represents the periodic material's microstructure, as shown in Figure 2.14.

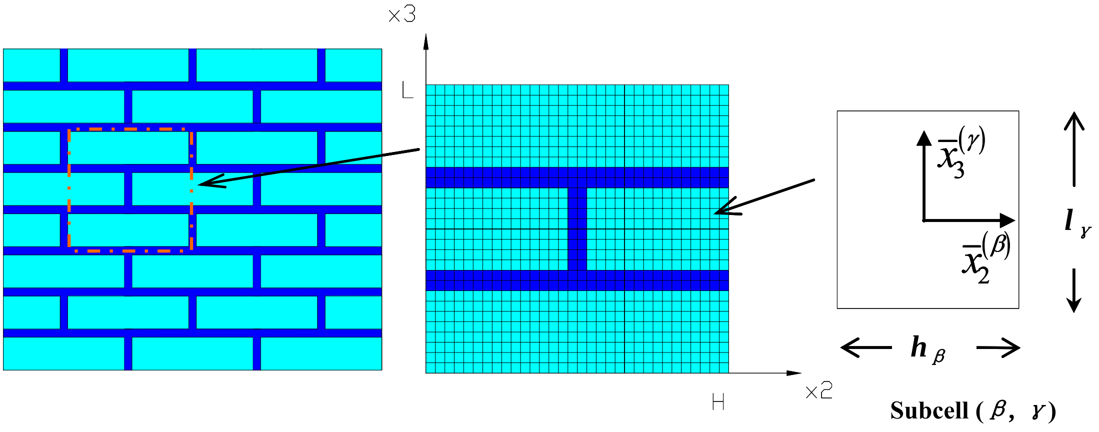

(a) (b) (c)

Figure 2.14: (a) A multiphase composite with a periodic microstructure built up with repeating unit cells; (b) discretization of the repeating unit cell into fundamental subcells; and (c) subcell composed of one material

The fundamental subvolume of the unit cell construction is a single subcell (β,γ) shown in Fig. 1(c), where β = 1,..., N_β and γ = 1,..., N_γ along the x$_2$ and x$_3$ axes, respectively. The subcell dimensions along these axes are h_β and l_γ such that

$$H=\sum_{\beta=1}^{N_\beta} h_\beta \text{ and } L=\sum_{\gamma=1}^{N_\gamma} l_\gamma \tag{2.2}$$

where H and L are the overall unit cell dimensions shown in Fig. 1(b).

The displacement filed representation in each (β,γ) subcell $u_i^{(\beta,\gamma)}$ is decomposed of the average displacement and the fluctuating displacement as follows:

$$u_i^{(\beta,\gamma)}(\mathbf{x})=\bar{u}_i+u_i'^{(\beta,\gamma)}(\mathbf{x}) \tag{2.3}$$

where $\bar{u}_i$ is the macroscopic average displacement components for the RUC; $u_i'^{(\beta,\gamma)}$ is the fluctuating displacement for each subcell.

Similarly, the strain field for each subcell cell is decomposed of the average strain and fluctuating strains:

$$\varepsilon_{ij}^{(\beta,\gamma)}(\mathbf{x})=\bar{\varepsilon}_{ij}+\varepsilon_{ij}'^{(\beta,\gamma)}(\mathbf{x}) \tag{2.4}$$

where $\bar{\varepsilon}_{ij}$ is the average strain in the RUC and $\varepsilon_{ij}'(X)$ is the local fluctuating strain for each subcell, which are derived from the corresponding fluctuation displacement component u_i', as follows:

$$\varepsilon_{ij}'(\mathbf{x})=\frac{1}{2}\left(\frac{\partial u_i'(\mathbf{x})}{\partial x_j}+\frac{\partial u_j'(\mathbf{x})}{\partial x_i}\right) \tag{2.5}$$

The fluctuating displacement components $u_i'^{(\beta,\gamma)}$ are approximated in each subcell (β,γ) by the second-order, Legendre-type polynomial expansion (Aboudi, Asme et al. 2001):

$$u_i'^{(\beta,\gamma)} = W_{i(00)}^{(\beta,\gamma)} + \bar{x}_2 W_{i(10)}^{(\beta,\gamma)} + \bar{x}_3 W_{i(01)}^{(\beta,\gamma)} + \frac{1}{2}\left(3(\bar{x}_2)^2 - \frac{h_\beta^2}{4}\right) W_{i(20)}^{(\beta,\gamma)} + \frac{1}{2}\left(3(\bar{x}_3)^2 - \frac{l_\gamma^2}{4}\right) W_{i(02)}^{(\beta,\gamma)} \quad (2.6)$$

where i = 1, 2, 3 and $W_{i(mn)}^{(\beta,\gamma)}$ are unknown microvariables associated with each subcell (β,γ).

Now we will derive the kinematic equations using the standard axial constraint condition, i.e., $\bar{\varepsilon}_{11}^{(\beta,\gamma)} = \bar{\varepsilon}_{11}$. Plug Equations (2.5) and (2.6) into Equation (2.4), we obtained:

$$\begin{aligned}
\varepsilon_{11}^{(\beta,\gamma)} &= \bar{\varepsilon}_{11} \\
\varepsilon_{22}^{(\beta,\gamma)} &= \bar{\varepsilon}_{22} + W_{2(10)}^{(\beta,\gamma)} + 3\bar{x}_2 W_{2(20)}^{(\beta,\gamma)} \\
\varepsilon_{33}^{(\beta,\gamma)} &= \bar{\varepsilon}_{33} + W_{3(01)}^{(\beta,\gamma)} + 3\bar{x}_3 W_{3(02)}^{(\beta,\gamma)} \\
\varepsilon_{12}^{(\beta,\gamma)} &= \bar{\varepsilon}_{12} + \frac{1}{2}\left[W_{1(10)}^{(\beta,\gamma)} + 3\bar{x}_2 W_{1(20)}^{(\beta,\gamma)}\right] \\
\varepsilon_{13}^{(\beta,\gamma)} &= \bar{\varepsilon}_{13} + \frac{1}{2}\left[W_{1(01)}^{(\beta,\gamma)} + 3\bar{x}_3 W_{1(02)}^{(\beta,\gamma)}\right] \\
\varepsilon_{23}^{(\beta,\gamma)} &= \bar{\varepsilon}_{23} + \frac{1}{2}\left[W_{2(01)}^{(\beta,\gamma)} + 3\bar{x}_3 W_{2(02)}^{(\beta,\gamma)} + W_{3(10)}^{(\beta,\gamma)} + 3\bar{x}_2 W_{3(20)}^{(\beta,\gamma)}\right]
\end{aligned} \quad (2.7)$$

The subcell stress components $\sigma_{ij}^{(\beta,\gamma)}$ are then expressed in terms of the stiffness and strain components for each subcell (β,γ) using generalized Hook's law, and inelastic subcell stress components:

$$\sigma_{ij}^{(\beta,\gamma)} = C_{ijkl}^{(\beta,\gamma)} \varepsilon_{kl}^{(\beta,\gamma)} - \sigma_{ij}^{in(\beta,\gamma)} \quad (2.8)$$

where

$$\sigma_{ij}^{in(\beta,\gamma)} = 2\mu^{(\beta,\gamma)}\varepsilon_{ij}^{in(\beta,\gamma)} \tag{2.9}$$

where $\mu^{(\beta,\gamma)}$ is the shear modulus and $\varepsilon_{ij}^{in(\beta,\gamma)}$ is the inelastic stain components for each subcell (β,γ).

The inelastic stress components $\sigma_{ij}^{in(\beta,\gamma)}$ are approximated using a sufficiently large number of Legendre polynomials by expanding as follows

$$\sigma_{ij}^{in(\beta,\gamma)} = \sum_{n=0}^{\infty}\sum_{m=0}^{\infty}\sqrt{(1+2m)(1+2n)}\tau_{ij(mn)}^{in(\beta,\gamma)}P_m(\xi_2)P_n(\xi_3) \tag{2.10}$$

where $-1 \le \xi_2, \xi_3 \le 1$ and the non-dimensionalized coordinates ξ_2, ξ_3 are defined as $\xi_2 = \bar{x}_2/(h_\beta/2)$, and $\xi_3 = \bar{x}_3/(h_\gamma/2)$. Using orthogonal properties of Legendre polynomials, the coefficients are $\tau_{ij(mn)}^{in(\beta,\gamma)}$ obtained in terms of inelastic strain distributions

$$\tau_{ij(mn)}^{in(\beta,\gamma)} = \frac{\mu^{(\beta,\gamma)}\sqrt{(1+2m)(1+2n)}}{2}\int_{-1}^{1}\int_{-1}^{1}\varepsilon_{ij}^{in(\beta,\gamma)}P_m(\xi_2)P_n(\xi_3)\,d\xi_2 d\xi_3 \tag{2.11}$$

Local stiffness matrix

The local stiffness matrix will be constructed to relate the surface-averaged tractions to the surface-averaged fluctuating displacements directly, which are defined as below.

The surface – averaged fluctuating displacements are the basic unknowns in the integrated systems of equation. The surface-averaged fluctuating displacements are defined at the rectangular boundaries of each subcell and are expressed as:

$$\overline{u}'^{(2\pm)(\beta,\gamma)}_{i} = \frac{1}{l_\gamma}\int_{-l_\gamma/2}^{l_\gamma/2} u'^{(\beta,\gamma)}_{i}(\pm\frac{h_\beta}{2},\overline{x}_3^{(\gamma)})\ d\overline{x}_3^{(\gamma)} \tag{2.12}$$

$$\overline{u}'^{(3\pm)(\beta,\gamma)}_{i} = \frac{1}{h_\beta}\int_{-h_\beta/2}^{h_\beta/2} u'^{(\beta,\gamma)}_{i}(\overline{x}_2^{(\beta)},\ \pm\frac{l_\gamma}{2},)\ d\overline{x}_2^{(\beta)} \tag{2.13}$$

In the above equations, $u_i'^{(j\pm)(\beta,\gamma)}$ is the fluctuating surface-averaged displacement in the i^{th} direction evaluated on the face of the (β,γ) subcell with normal in the $+j^{th}$ direction or $-j^{th}$, Figure 2.15.

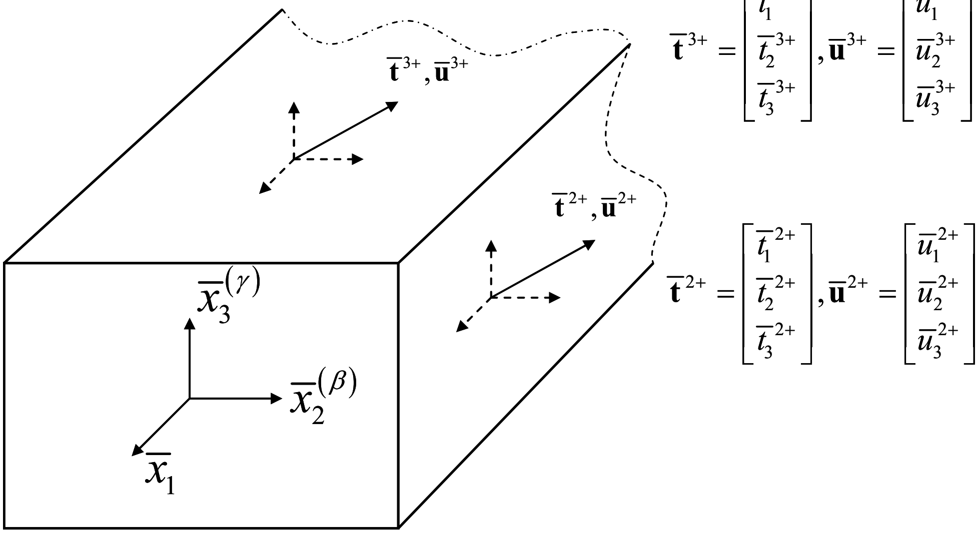

Figure 2.15: The surface-averaged displacement and traction components defined in a subcell

Performing the above averaging procedure yields the following equations in terms of subcell microvariables:

$$\overline{u}'^{(2\pm)(\beta,\gamma)}_{i} = W^{(\beta,\gamma)}_{i(00)} \pm \frac{h_\beta}{2} W^{(\beta,\gamma)}_{i(10)} + \frac{h_\beta^2}{4} W^{(\beta,\gamma)}_{i(20)} \tag{2.14}$$

$$\overline{u}'^{(3\pm)(\beta,\gamma)}_{i} = W^{(\beta,\gamma)}_{i(00)} \pm \frac{l_\gamma}{2} W^{(\beta,\gamma)}_{i(01)} + \frac{l_\gamma^2}{4} W^{(\beta,\gamma)}_{i(02)}, i = 1,2,3 \tag{2.15}$$

Similar to the definition of the surface-averaged fluctuating displacements, the surface-averaged tractions is defined as follows:

$$\overline{t}^{(2\pm)(\beta,\gamma)}_{i} = \frac{1}{l_\gamma} \int_{-l_\gamma/2}^{l_\gamma/2} t_i^{(\beta,\gamma)} (\pm \frac{h_\beta}{2}, \overline{x}_3^{(\gamma)}) \; d\overline{x}_3^{(\gamma)} \tag{2.16}$$

$$\overline{t}^{(3\pm)(\beta,\gamma)}_{i} = \frac{1}{h_\beta} \int_{-h_\beta/2}^{h_\beta/2} t_i^{(\beta,\gamma)} (\overline{x}_2^{(\gamma)}, \; \pm \frac{l_\gamma}{2},) \; d\overline{x}_2^{(\beta)} \tag{2.17}$$

Surface traction components are expressed in terms of stress components through Cauthy's relations for a particular subcell face:

$$t_i^{n(\beta,\gamma)} = \sigma_{ji}^{(\beta,\gamma))} n_j^{(\beta,\gamma)} \tag{2.18}$$

where $n_i^{(\beta,\gamma)}$ is the unit normal to a given face of the (β,γ) subcell.

Employing Equation (2.18) and Equations (2.7) - (2.10) into Equations (2.16) and (2.17), and performing some algebraic manipulations, the surface-averaged tractions can be expressed in terms of the subcell microvariables and applied macroscopic strains, and inelastic contributions, as shown in Appendix A. In order to construct the local stiffness matrix, which relates the surface-averaged tractions to the surface-averaged fluctuating displacements directly, the first and second order microvariables in the Appendix A must be expressed in terms of the surface-averaged fluctuating displacements. This is achieved by inverting Equations (2.6) and (2.7) which allow us to express the first and second order microvariables in terms of surface-averaged fluctuating displacements, as shown in Appendix B.

Global stiffness matrix

Continuity and periodic boundary conditions

The solution for the unknown surface-averaged interfacial displacement field for the RUC are obtained by applying interfacial traction and displacement continuity conditions at each interior subcell interface, and periodic boundary conditions at the boundary subcells. At the β^{th} interface separating (β,γ) and $(\beta+1,\gamma)$ subcells, the surface-averaged traction components associated with the particular subcell face must be continuous, as shown in Figure 2.16

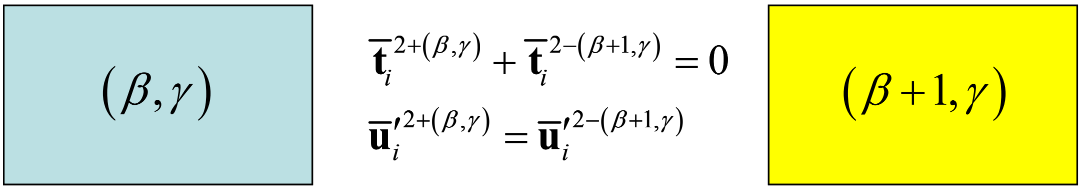

$$\overline{\mathbf{t}}_i^{2+(\beta,\gamma)} + \overline{\mathbf{t}}_i^{2-(\beta+1,\gamma)} = 0$$

$$\overline{\mathbf{u}}_i'^{2+(\beta,\gamma)} = \overline{\mathbf{u}}_i'^{2-(\beta+1,\gamma)}$$

Figure 2.16: Application of traction and fluctuating displacement continuity at the vertical interfaces between the adjacent subcells

The same holds true for the γ^{th} interface separating (β,γ) and $(\beta,\gamma+1)$ subcells. These conditions are ensured by

$$\begin{aligned} \bar{t}_i^{(2+)(\beta,\gamma)} + \bar{t}_i^{(2-)(\beta+1,\gamma)} &= 0 \\ \bar{t}_i^{(3+)(\beta,\gamma)} + \bar{t}_i^{(3-)(\beta,\gamma+1)} &= 0 \qquad i = 1,\ 2,\ 3 \end{aligned} \tag{2.19}$$

Similarly, the three fluctuating surface-averaged displacements on either side of the β^{th} and γ^{th} interfaces must be equal. These continuity conditions are enforced by setting the corresponding displacement components to common unknown quantities as shown below:

$$\begin{aligned} \bar{u}_i'^{(2+)(\beta,\gamma)} &= \bar{u}_i'^{(2-)(\beta+1,\gamma)} = \bar{u}_i'^{2\,(\beta+1,\gamma)} \\ \bar{u}_i'^{(3+)(\beta,\gamma)} &= \bar{u}_i'^{(3-)(\beta,\gamma+1)} = \bar{u}_i'^{3\,(\beta,\gamma+1)} \end{aligned} \tag{2.20}$$

The above equations hold true at $\beta = 1, \ldots, \quad N_{\beta-1}$ and $\gamma = 1, \ldots, \quad N_{\gamma-1}$ subcell interfaces, respectively.

In addition, the periodic boundary conditions satisfy between the adjacent repeating unit cells (RUC), Figure 2.17.

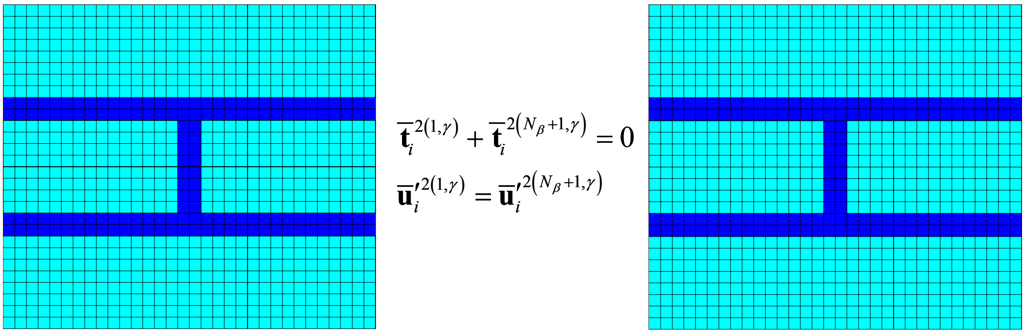

Figure 2.17: Application of periodicity conditions at the boundaries of the unit

$$\bar{t}_i^{2(1,\gamma)} + \bar{t}_i^{2(N_\beta+1,\gamma)} = 0, \qquad \bar{t}_i^{3(\beta,1)} + \bar{t}_i^{3(\beta,N_\gamma+1)} = 0 \tag{2.21}$$

$$\overline{u}_i'^{2(1,\gamma)} = \overline{u}_i'^{2(N_\beta+1,\gamma)}, \qquad \overline{u}_i'^{3(\beta,1)} = \overline{u}_i'^{3(\beta,N_\gamma+1)} \quad (i = 1,2,3) \tag{2.22}$$

Assembly of global stiffness matrix

Assembling the continuity and periodicity equations, we obtain final systems of equations relating surface-averaged interfacial displacements to applied macroscopic strain, as shown in the following:

$$\begin{bmatrix} \mathbf{L}_{11} & \mathbf{L}_{12} \\ \mathbf{L}_{21} & \mathbf{L}_{22} \end{bmatrix} \begin{bmatrix} \overline{\mathbf{u}}_1^2 \\ \overline{\mathbf{u}}_1^3 \end{bmatrix} = \begin{bmatrix} \Delta\mathbf{c}_{11} & 0 \\ 0 & \Delta\mathbf{c}_{22} \end{bmatrix} \begin{bmatrix} \overline{\varepsilon}_{12} \\ \overline{\varepsilon}_{13} \end{bmatrix} + \begin{bmatrix} \Delta\mathbf{G}_{o1} \\ \Delta\mathbf{G}_{o2} \end{bmatrix} \tag{2.23}$$

$$\begin{bmatrix} \mathbf{K}_{11} & 0 & \mathbf{K}_{13} & \mathbf{K}_{14} \\ 0 & \mathbf{K}_{22} & \mathbf{K}_{23} & \mathbf{K}_{24} \\ \mathbf{K}_{31} & \mathbf{K}_{32} & \mathbf{K}_{33} & 0 \\ \mathbf{K}_{41} & \mathbf{K}_{41} & 0 & \mathbf{K}_{44} \end{bmatrix} \begin{bmatrix} \overline{\mathbf{u}}_2'^2 \\ \overline{\mathbf{u}}_3'^2 \\ \overline{\mathbf{u}}_2'^3 \\ \overline{\mathbf{u}}_3'^3 \end{bmatrix} = \begin{bmatrix} \Delta\mathbf{c}_{11} & \Delta\mathbf{c}_{12} & \Delta\mathbf{c}_{13} & 0 \\ 0 & 0 & 0 & \Delta\mathbf{c}_{24} \\ 0 & 0 & 0 & \Delta\mathbf{c}_{34} \\ \Delta\mathbf{c}_{41} & \Delta\mathbf{c}_{42} & \Delta\mathbf{c}_{43} & 0 \end{bmatrix} \begin{bmatrix} \overline{\varepsilon}_{11} \\ \overline{\varepsilon}_{22} \\ \overline{\varepsilon}_{33} \\ \overline{\varepsilon}_{23} \end{bmatrix} + \begin{bmatrix} \Delta\mathbf{G}_{i1} \\ \Delta\mathbf{G}_{i2} \\ \Delta\mathbf{G}_{i3} \\ \Delta\mathbf{G}_{i4} \end{bmatrix} \tag{2.24}$$

where

$$\overline{\mathbf{u}}_i'^2 = \left[\overline{\mathbf{u}}_i'^{2(1)}, \ldots, \overline{\mathbf{u}}_i'^{2(N_\gamma)} \right] \text{ with } \overline{\mathbf{u}}_i'^{2(\gamma)} = \left[\overline{u}_i'^{2(1,\gamma)}, \ldots, \overline{u}_i'^{2(N_\beta,\gamma)} \right]$$

$$\overline{\mathbf{u}}_i'^3 = \left[\overline{\mathbf{u}}_i'^{3(1)}, \ldots, \overline{\mathbf{u}}_i'^{3(N_\beta)} \right] \text{ with } \overline{\mathbf{u}}_i'^{3(\beta)} = \left[\overline{u}_i'^{3(\beta,1)}, \ldots, \overline{u}_i'^{3(\beta,N_\gamma)} \right]$$

Homogenized stiffness matrix

Once the solution for the displacement field for each $\overline{\mathrm{U}}'$ is obtained by Equations (2.23) and (2.24), the average strain $\overline{\varepsilon}^{(\beta,\gamma)}$ in each subcell are related to the average macroscopic strains through the localization relation by Equations (2.4) and (2.5), which can be symbolically written as:

$$\overline{\boldsymbol{\varepsilon}}^{(\beta,\gamma)} = \mathrm{A}^{(\beta,\gamma)}\overline{\boldsymbol{\varepsilon}} \tag{2.25}$$

where $\mathrm{A}^{(\beta,\gamma)}$ are called Hill's elastic strain concentration matrices.

The average composite stress in the RUC is related to the average stress in all the subcells through the expression

$$\overline{\boldsymbol{\sigma}} = \frac{1}{HL}\sum_{\beta=1}^{N_\beta}\sum_{\gamma=1}^{N_\gamma} h_\beta l_\gamma \overline{\boldsymbol{\sigma}}^{(\beta,\gamma)} \tag{2.26}$$

where the average stress $\overline{\sigma}^{(\beta,\gamma)}$ is related to the average strain $\overline{\varepsilon}^{(\beta,\gamma)}$ in each homogeneous subcell through the Hook's law

$$\overline{\boldsymbol{\sigma}}^{(\beta,\gamma)} = \mathbf{C}^{(\beta,\gamma)}\overline{\boldsymbol{\varepsilon}}^{(\beta,\gamma)} \tag{2.27}$$

Substituting Equations (2.25) and (2.27) into Equation (2.26), the average composite stress $\overline{\boldsymbol{\sigma}}$ can be related to average composite strain $\overline{\boldsymbol{\varepsilon}}$:

$$\overline{\boldsymbol{\sigma}} = \left(\frac{1}{\mathbf{HL}}\sum_{\gamma=1}^{\mathbf{N}_\gamma}\sum_{\beta=1}^{\mathbf{N}_\beta} \mathbf{h}_\beta \mathbf{l}_\gamma \mathrm{C}^{(\beta,\gamma)}\mathrm{A}^{(\beta,\gamma)}\right)\overline{\boldsymbol{\varepsilon}} \tag{2.28}$$

where the coefficients in the brackets are called effective (homogenized) stiffness matrix C^*, i.e.,

$$\mathbf{C}^* = \frac{1}{HL}\sum_{\gamma=1}^{N_\gamma}\sum_{\beta=1}^{N_\beta} h_\beta l_\gamma \mathbf{C}^{(\beta,\gamma)}\mathbf{A}^{(\beta,\gamma)} \tag{2.29}$$

For the orthotropic material such as regular masonry structures, there are only nine independent constants in effective stiffness matrix C^* (Jones 1999), i.e.

$$\mathrm{C}^* = \begin{bmatrix} C_{11}^* & C_{12}^* & C_{13}^* & 0 & 0 & 0 \\ C_{21}^* & C_{22}^* & C_{23}^* & 0 & 0 & 0 \\ C_{31}^* & C_{32}^* & C_{33}^* & 0 & 0 & 0 \\ 0 & 0 & 0 & C_{44}^* & 0 & 0 \\ 0 & 0 & 0 & 0 & C_{55}^* & 0 \\ 0 & 0 & 0 & 0 & 0 & C_{66}^* \end{bmatrix} \tag{2.30}$$

The homogenized compliance matrix is the inversion of the stiffness matrix, i.e.

$$\mathrm{S}^* = \mathrm{C}^{*-1} \tag{2.31}$$

For any orthotropic material, the compliance matrix is related to the engineering constants,

$$\mathrm{S}^* = \begin{bmatrix} \frac{1}{E_1^*} & -\frac{\nu_{21}^*}{E_2^*} & -\frac{\nu_{31}^*}{E_3^*} & 0 & 0 & 0 \\ -\frac{\nu_{21}^*}{E_2^*} & \frac{1}{E_2^*} & -\frac{\nu_{32}^*}{E_3^*} & 0 & 0 & 0 \\ -\frac{\nu_{31}^*}{E_3^*} & -\frac{\nu_{32}^*}{E_3^*} & \frac{1}{E_3^*} & 0 & 0 & 0 \\ 0 & 0 & 0 & \frac{1}{G_{23}^*} & 0 & 0 \\ 0 & 0 & 0 & 0 & \frac{1}{G_{31}^*} & 0 \\ 0 & 0 & 0 & 0 & 0 & \frac{1}{G_{12}^*} \end{bmatrix} \tag{2.32}$$

Once the homogenized compliance matrix S^* is obtained, all the engineering constants for the homogenized composites can be determined by Equation (2.32)

$$\begin{aligned}
&E_1^* = 1/S_{11}^*, E_2^* = 1/S_{22}^*, E_3^* = 1/S_{33}^*;\\
&G_{23}^1 = 1/S_{44}^*, G_{31}^* = 1/S_{55}^*, G_{12}^* = 1/S_{66}^*;\\
&\nu_{21}^* = -E_2^* \times S_{12}^*, \nu_{31}^* = -E_3^* \times S_{13}^*, \nu_{32}^* = -E_3^* \times S_{32}^*.
\end{aligned} \tag{2.33}$$

<u>2.3.2. Macro modeling of masonry structure</u>

In the traditional continuous theory, masonry can also be analyzed like a continuum homogeneous media. This approach is called macro-modelling approach. The macro-models don’t make distinction between units and mortar joints and treat the masonry structure as a single material with the average properties. When the global behaviour of the structure is of prime importance, macro modelling of masonry is advantageous over micro modeling. The macro-modeling can reduce the enormous computational cost compared with micromodelling, which makes possible the numerical analyses of complex structures such as bridges and buildings. Currently the most important macro-modeling techniques for the analysis of masonry structures are towards the use of finite element method and discrete element method. These two approaches for macro modeling of the masonry structure from literature were reviewed as following.

2.3.2.1 Finite element method (FEM)

The finite element method is a powerful numerical method for the structural analysis and it has been extensively used for analyzing the behavior of masonry structures in the last decade. A two-phase nonhomogeneous finite element model (micromodeling of brick and mortar) of masonry has been used by (Page 1978; Lotfi and Shing 1994; Lourenco, Rots et al. 1998). To simplify the problem, a homogeneous one-phase material (macro-) model has been used by some investigators, such as (Samarasinghe 1980; Dhanasekar, Kleeman et al. 1985). (Loo and Yang 1991) consider the combined nonlinear stress–

strain properties of mortar and brick masonry units to develop a simplified approach to the failure of masonry in cracking or crushing, and the post-failure behaviour. They settled on a von Mises failure criterion in compression and a complete loss of normal and shear stiffness in the principal stress direction after reaching a failure strain. (Ng, Fairfield et al. 1991) applied a two dimensional nonlinear finite element code to the analysis of some of the arch bridges. The masonry is modeled as a von Mises material, with differing tensile and compressive strength, while a Coulomb–Mohr failure criterion is applied to the filled bricks. (Molins and Roca 1998) proposed the use of a flexibility model, implemented into a finite element code. Using this method, they modeled a prototype arch bridge. They are able to reproduce localized damage that does not spread far beyond the location of the original cracking.

Dhanasekar et al. (1985a) proposed a macro model for solid masonry, which was capable of reproducing the effects of material nonlinearity and progressive local failure. URM was modelled as a continuum with average properties of brick and mortar with appropriate nonlinear behaviour of mortar included. Each element in the finite element mesh encompassed several masonry units and joints. The effects of local brick or joint failure were smeared across the portion governed by the Guassian integration points of the finite element. This technique enabled the efficient analysis of large panels but could not be used for the analysis of local effects.

To incorporate strain softening effects (in other words to avoid potential sudden redistribution of stresses), Ali and Page (1988) defined a descending branch of stress strain curve of masonry assemblage in their finite element model. They showed that an ultimate strain equal to six times the cracking strain predicted the softening behaviour accurately. Ghosh et al. (1994) also used a value of ultimate strain equal to six times the cracking strain to match the experimental ultimate load.

Shing et al. (1993b) have concluded that for modelling the brittle shear behaviour of masonry walls; a discrete crack approach is essential, in which the mortar joint interface captures the development of the dominant shear crack. Hence they adopted the discrete crack approach to model the major diagonal crack by means of interface elements and secondary cracks by smeared crack elements. This approach requires knowledge on the crack path as a priori.

Riddington and Naom (1994) modelled mortar joints as interface elements with nonlinear material characteristics to predict the compressive strength of masonry panels. Khattab and Drysdale (1994) also formulated a homogeneous model of masonry with considerations of mortar joints as planes of weakness.

Lourenco et al. (1997) modelled masonry units as continuum elements while mortar joints and potential cracks in units were represented as zero-thickness interface elements. Interface elements were modelled with an interface cap model to include all possible failure mechanisms of masonry structures. These mechanisms included cracking in the joints, sliding along the bed and the head joints, cracking of masonry units in direct tension, diagonal tension cracking of masonry units at values of normal stress sufficient to develop friction in joints, and splitting of units in tension as a result of mortar dilatancy at high values of normal stress. This model reproduced the complete path of load-displacement until total degradation with minimal numerical difficulties.

Sayed-Ahmed and Shrive (1995) analyzed face-shell bedded hollow masonry prisms subjected to concentrated loads by modelling face shells as discrete shell elements with orthotropic material characteristics using the smeared crack method, and web cracking and splitting as interface elements using the discrete cracking method. The smeared crack model for orthotropic material was used to simulate the nonlinear material behaviour in the failure process. Cracking in units and mortar was modelled using the Mohr-Coulomb criterion. Interface elements were modelled using the Lagrange multiplier technique. Multipoint constraint equations were used to provide compatibility between continuum and shell elements. To define crack detection surface for units and mortar, material constants such as relationships of uniaxial tensile stress and uniaxial compressive strength, biaxial compression and biaxial tension-compression and ratio of tensile and compressive strengths were used in this study.

Ghosh et al. (1994) used ABAQUS to model solid masonry walls subjected to vertical and/or horizontal loads. Masonry was treated as a two-phase material in which the bricks and the mortar were modelled as a continuum and the contact between the bricks and mortar was modelled by interface elements. They used the inelastic constitutive model of concrete available in ABAQUS for both brick and mortar.

Due to lack of biaxial test results on brick and mortar, Ghosh et al. (1994) used the values of the ratio of ultimate strength in biaxial compression to ultimate strength in uniaxial compression (ao) and the ratio of the total plastic strain in uniaxial compression to total plastic strain in biaxial compression (co) of concrete for both brick and mortar. For concrete these values are 2.16 and 2.28 respectively. Once values of ‘ao’ and ‘co’ are selected, the values of yield stress in the state of pure shear stress (τp) and the hardening parameter (λc) can be determined from uniaxial test data. The fracture energies for bricks and mortar were obtained from Van der Pluijm (1992). Tensile strength of bricks and mortar were obtained from Ali and Page (1988).

Zhuge (1995) developed a two-dimensional plane stress element model for the non-linear analysis of URM shear walls. This model was developed using a homogeneous material model to predict the detailed load-deflection characteristics and critical limit states of URM walls under inplane earthquake ground acceleration. Later Zhuge and Thambiratnum (1998) combined a two dimensional finite element model for nonlinear joint behaviour with an isotropic material model developed for reinforced concrete to analyze masonry subjected to inplane static and dynamic loading.

In spite of many efforts made by previous researchers, however, reference to seismic/dynamic modeling and analysis of masonry has been rare in engineering literature. A review of previous studies on dynamic behavior of masonry has revealed that most research work has focused on experimental investigations (Klopp and Griffith 1994; Tomazevic, Lutman et al. 1996). For finite element modeling of masonry under dynamic loads, a single degree-of-freedom model is still commonly used (Lankulovski and Parsanejad 1994). This model can be used to study the global behavior of a building system, but the local response of masonry walls, such as cracking, crack propagation, and crushing cannot be represented by the model. A two-dimensional finite element model has been employed by some investigators to study the cyclic behavior of masonry (Larovere 1990; Vratsanou 1991). However, the analyses were under pseudodynamic loads, which essentially mean that a static analysis was performed with cyclic stress-strain relations.

The above survey of the literature reveals that recently some research about the numerical analysis of the masonry structure were initiated, the seismic behavior of masonry structure has not been explored despite the urgent need to develop effective methods for seismic analysis of masonry structure. It is this gap that the author intends to fill in this study through analytical developments.

Constitutive law for masonry: Mohr-Coulomb model

The Mohr-Coulomb failure or strength criterion has been widely used for geotechnical applications. Indeed, a large number of the routine design calculations in the geotechnical area are still performed using the Mohr-Coulomb criterion.

The Mohr-Coulomb criterion assumes that failure is controlled by the maximum shear stress and that this failure shear stress depends on the normal stress. This can be represented by plotting Mohr's circle for states of stress at failure in terms of the maximum and minimum principal stresses. The Mohr-Coulomb failure line is the best straight line that touches these Mohr's circles (Figure 2.18). Thus, the Mohr-Coulomb criterion can be written as

$$\tau = c + \sigma \tan \phi \tag{2.34}$$

where τ is the shear stress, σ is the normal stress (negative in compression), c is the cohesion of the material, and ϕ is the material angle of friction.

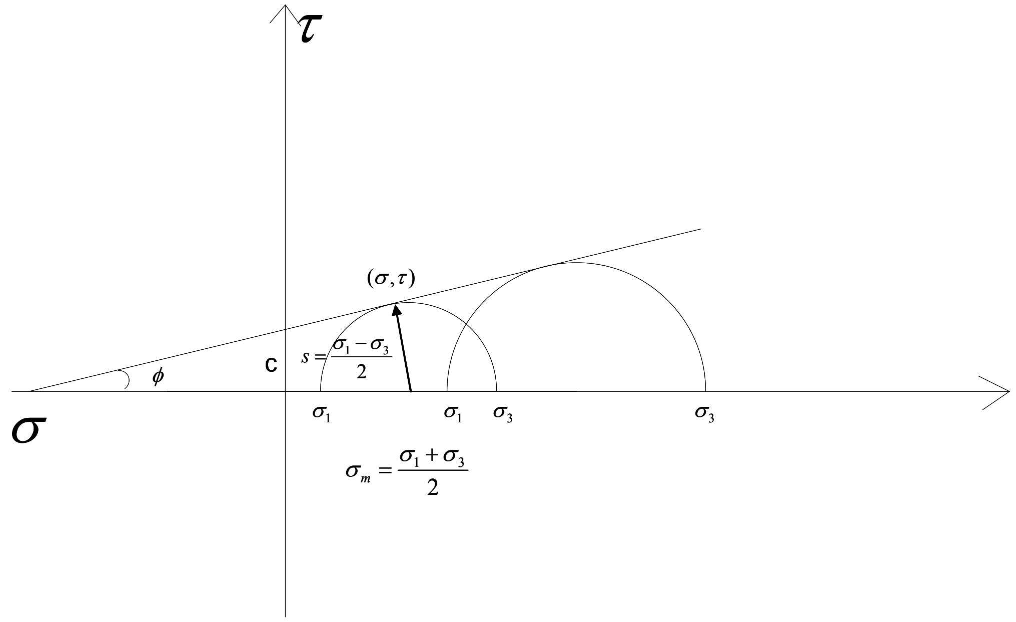

Figure 2.18: Mohr-Coulomb failure criterion

From Mohr's circle,

$$\tau = s\cos\phi \tag{2.35}$$

$$\sigma = \sigma_m + s\sin\phi \tag{2.36}$$

Substituting for τ and σ, the Mohr-Coulomb criterion can be rewritten as:

$$s + \sigma_m \sin\phi - c\cos\phi = 0 \tag{2.37}$$

where $s = \frac{1}{2}(\sigma_1 - \sigma_3)$ is half of the difference between the maximum and minimum principal stresses (and is, therefore, the maximum shear stress) and $\sigma_m = \frac{1}{2}(\sigma_1 + \sigma_3)$ is the average of the maximum and minimum principal stresses (the normal stress). The failure of typical geotechnical materials generally includes some small dependence on the intermediate principal stress, but the Mohr-Coulomb model is generally considered to be sufficiently accurate for most applications. This failure model has vertices in the deviatoric stress plane (see Figure 2.19).

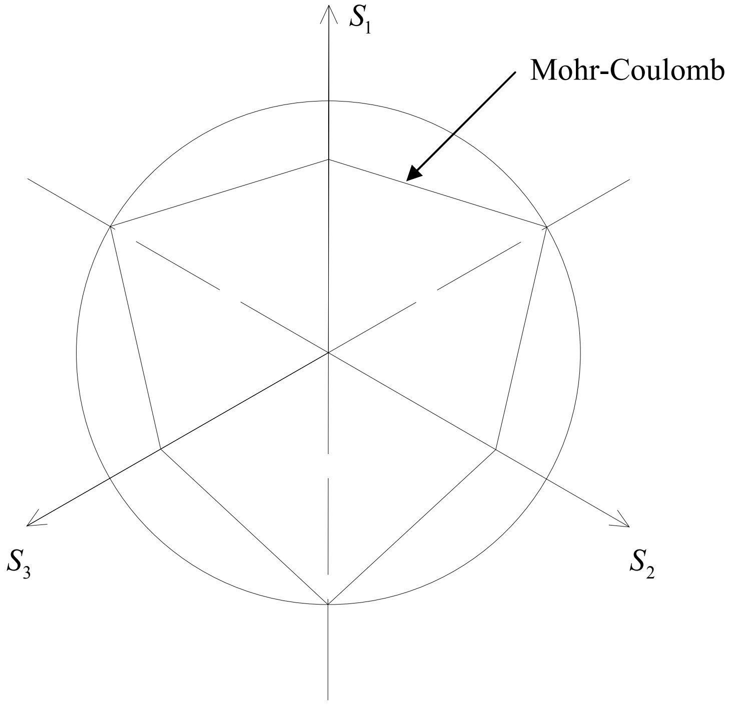

Figure 2.19: Mohr-Coulomb model in the deviatoric plane

2.3.2.2 Discrete element method (DEM)

The conventional finite element programs based upon continuum mechanics can simulate the non-linear constitutive behavior, but are difficult to represent discontinuities. Currently there are several boundary element and finite difference programs available, which have interface elements that enable them to model a discontinuous material to some extent. However, their formulation is usually restricted since these formulations can not have an automatic scheme for recognizing new contacts and the formulation is limited to small displacements and rotation. The discrete element method proposed by (Cundall 1971) overcomes these limitations and allows displacements and rotations of discrete bodies, including complete detachment, and can recognizes new contacts automatically as the calculation progresses.

A discontinuous medium is distinguished from a continuous one by the existence of contacts or interfaces between the discrete bodies that comprise the system. The distinct element method was originally created as a two-dimensional representation of a jointed rock mass, but the method has also been extended to applications in granular material (Cundall 1979), and crack development in rocks and concrete (Plesha and Aifantis. 1983; Lorig 1984). The most recent two-dimensional program, *UDEC - Universal Distinct Element Cod*e (Itasca Consulting Group 1996), was first developed to represent both rigid and deformable bodies (blocks) separated by discontinuities (Lemos, Hart et al. 1985). This code can perform either static or dynamic analyses.

Recently various discrete element application to masonry structures have been reported for both static (Lemos 1995)and dynamic analysis (Shabawi and Verdel 1995; Panantonopoulos, Psycharis et al. 1998). Several researchers have used the discrete element methods to study the in-plane behavior of unreinforced masonry (Rots 1991; Lofti and Shing 1994; Shabawi and Verdel 1995; Azevedo, Erri et al. 2000), but there has been little application of out-of-plane effects. The researches about the seismic response of masonry structure are still very rare.

In the distinct element method, a rock mass is represented as an assembly of discrete blocks. Joints are viewed as interfaces between distinct bodies (i.e., the discontinuity is treated as a boundary condition). The contact forces and displacements at the interfaces of a stressed assembly of blocks are found through a series of calculations which trace the movements of the blocks. The dynamic behavior is represented numerically by a timestepping algorithm which is the identical solution scheme as the explicit finite-difference method for a continuum analysis.

The calculations performed in the distinct element method alternate between application of a force-displacement law at all contacts and Newton's second law at all blocks. The force-displacement law is used to find contact forces from known displacements. Newton's second law gives the motion of the blocks resulting from the known forces acting on them. Then, the application of the block material constitutive relations gives new stresses within the elements.

After reviewed both the popular approach of Marco-modeling the masonry structure, it was found that the both approach has its advantage and disadvantages. The choice of the numerical modeling technique depends on the objectives of the study and the sought information. Moreover, this choice of numerical modeling technique is also constrained by the existing experimental data, required by numerical modelling. It is possible that different methods lead to different results, depending on the adequacy of the numerical tool to the sought information. The best method might be defined as the method that provides the sought information in a reliable manner, i.e. within an acceptable error. In this study, the finite element method will be used to investigate the seismic behavior of the unreinforced masonry tower since experimental data is available for the Mohr-Coulomb model. Macro modeling using finite element models also provides cost effective solutions compared to the experimental alternative.

2.4 Summary

As so far, the behavior of masonry under uniaxial and biaxial compressive loading has been investigated by a number of researchers, however, experimental studies on how the crack evolution and propagation in the masonry are rarely seen in the literature. In this study, the technique of Digital Image Correlation will be used to quantitatively construct the full-field strain maps of masonry specimens at various loading increments. The experimental investigation, which includes uniaxial compression test, vibrational resonance frequency test, and digital image correlation test, will be performed on the granite masonry as well as its constituent components, granite stone units and cement mortar. The obtained material properties such as elastic properties and yielding strength for the masonry constituents, i.e. granite units and cement mortar, will be used for numerical modeling for masonry structure.

After comparing the both micro-modeling and macro-modeling approaches from the literature review, two stage modeling strategy will be adopted to model the seismic behavior of large-scale masonry structure in this study. First, homogeneous equivalent material properties are obtained by using micro-modeling approaches, i.e. FVDAM model. Then, the equivalent material properties are used to macro-model the seismic behavior of the large scale masonry structure such as the tower of the Brooklyn Bridge with the commercially available FEM software ABAQUS.

Among the various micro-modeling approaches proposed by many researchers (Pande, Liang et al. 1989; Pietruszczak and Niu 1991, Ma, Hao et al. 2001; Wu and Hao 2006, Bansal and Pindera 2006), the finite-volume direct averaging micromechanics (FVDAM) Model by Bansal and Pindera (2006) has been received extensively concern and verified thorough the experimental data. However, the plastic analysis capabilities of the FVDAM model are limited to model the bilinear hardening materials such as metals in the composite constituents and can not be directly used to masonry structures since mortar joints and block units as constituents of masonry structures are usually modeled as Mohr-Coulomb material. Hence, a plastic algorithm based on the Mohr-Coulomb failure criterion will be developed in the FVDAM model to simulate the constituents of the masonry, i.e., cement mortar and granite unit. Elasto-plastic analyses will be also carried out on the granite masonry structure to compare with the experimental results.

Although this micro-modeling approach may appear very straightforward, its major disadvantage comes from the extremely large number of elements to be generated as the structure increases in size and complexity. Hence, the use of micro-models becomes unlikely to use for the global analysis of entire buildings or bridges. To overcome this computational difficulty, the macro-modeling approach will be used to simulate the large-scale structure. The macro-models don't make distinction between blocks and mortar joints and smear the effect of joint presence through the formulation of the constitutive modeling of the equivalent material. The equivalent material properties obtained from the small masonry panel will be used to macro-model the seismic behavior of the large scale masonry structure with the FEM software ABAQUS.

Chapter 3: Experimental Investigation of Granite Masonry Structures

---

3.1 Overview

This Chapter presents experimental investigation of granite masonry structure, which includes uniaxial compression test, vibrational resonance frequency test, and digital image correlation test. These experimental tests are performed on the granite masonry as well as its constituent components, granite stone units and cement mortar. The main purposes of these compressive tests are to characterize the compressive behavior of the masonry materials, examine the effects of granite units and cement mortar on the strength and elastic constants of the granite masonry, and simultaneously examine the predictability of the FVDAM model on computing the homogenized elastic constants of the masonry from the properties of its constituent components.

3.2. Introduction

Masonry is composed of two very different materials, masonry units (stone, bricks, or blocks) and cement mortar. As one of the oldest building materials, masonry was not only used in many magnificent historical structures all over the world but is still used in various new constructions. The need of structural rehabilitation and strengthening of ancient masonry structures motivated studies to better understand the deformation and failure mechanism of masonry structures. Unreinforced masonry structures are particularly vulnerable to earthquake excitations due to the fact that the integrity of these structures relies mainly on the joining material between masonry blocks which is apt to crack when subjected to tension caused by earthquake lateral forces. The recent earthquakes in various countries have caused great damage and destruction to masonry bridges, religious temples, and other monumental buildings. These incidents further enlightened the need to have a better understanding of the behavior of the two-phase composite material through experimental and numerical studies.

One key aspect in the numerical analysis of masonry structures is to create a sound finite element model and carry out a reliable analysis. Probably the most accurate finite element modeling is to treat the masonry as a two-phase material and model masonry units and mortar joints separately. However, this detailed modeling would not be practical for the analysis of large-scale masonry structures. For instance, in the seismic assessment of the Brooklyn Bridge in New York City, when a global analysis of the entire bridge including the masonry towers, decks, and cables is considered, a detailed modeling may not be possible because of a huge number of degrees of freedom and an enormous demand of the computer memory and running time involved. One feasible way for this type of analysis is to analyze the overall masonry structure assuming the masonry units and mortar joints are smeared out and the masonry is treated as a homogeneous anisotropic continuum to identify the critical regions. These regions are then analyzed with a detailed modeling by treating the masonry units and mortar joints separately to capture the detailed behavior such as damage evolution and crack propagation in the regions. A reliable way to find the equivalent homogenized elastic constants of the masonry plays an essential role in this two-level analysis involving the overall and detailed modeling. The main focuses of the study presented in this paper are to investigate the behavior of the masonry units, mortar, and masonry composite including their crack formation and propagation under uniaxial compression as well as to verify a micromechanics-based homogenization model for computing the equivalent homogenized equivalent constants of masonry.

The capacity of masonry in compression is strongly related to the compressive strengths of the masonry units and the cement mortar. Usually, the mortar exhibits a much softer behavior than the units. The stacked bond prisms, such as the RILEM test specimen (RILEM 1994), are frequently used to assess the uniaxial compressive strength of masonry. Following a pioneering study of Hilsdorf (1969), various researchers (e.g., Hilsdorf 1969; CEN 1995) have tried to derive a relationship between the compressive strength of masonry and the compressive strengths of its individual components. The behavior of masonry under uniaxial and biaxial compressive loading has also been investigated by a number of researchers (Hilsdorf 1969; Page 1981; Dhanasekar, Page et al. 1985; Binda, Mirabella et al. 1996; Roca, Oliveira et al. 2001; Sarangapani, Reddy et al. 2005). However, experimental studies on how the crack evolution and propagation in the masonry are rarely seen in the literature. In this study, the technique of Digital Image Correlation (Sutton, Wolters et al. 1983; Sutton, Cheng et al. 1986) is used to quantitatively construct the full-field strain maps of masonry specimens at various loading increments. These strain maps provide a means to observe crack propagation, strain localization, and failure mechanism of the masonry.

A number of homogenization techniques have been developed in the past to derive numerically the equivalent homogenized elastic constants from the properties of each constitutive material of the composite (Pande, Liang et al. 1989; Pietruszczak and Niu 1991; Luciano and Sacco 1997). Recently, Bansal and Pindera (2005 and 2006) proposed a micromechanics-based model for SiC/Titanium composites called Finite-

Volume Direct Averaging Micromechanics (FVDAM). The analytical framework of the FVDAM model is based on the local/global stiffness matrix approach and the closed-form expressions derived from the homogenization theory for periodic materials (Paley and Aboudi 1992; Aboudi, Asme et al. 2001). The FVDAM model is modified and used in this study to calculate the homogenized elastic constants of masonry using the elastic moduli of the masonry units and cement mortar obtained from the compression tests. The computed equivalent elastic constants are then compared with those obtained from the experiment to verify the homogenization model.

In this paper, the uniaxial compression tests on granite units, cement mortar, and masonry composite, the vibrational resonance frequency tests on granite units and cement mortar, and the digital image correlation tests on masonry are described. The theoretical development of the FVDAM model is introduced, and then the results obtained from the experiments and from the FVDAM modeling are compared and presented.

3.3. Specimen Preparation

3.3.1 Granite stone

The granite stones chosen for the tests were based on its similarity with the granite used in the masonry towers of the Brooklyn Bridge in New York City (Weidlinger Associates 1996). The granite stones were mechanically cut into a cubic shape (2×2×2 in^3) and a prismatic shape (2×2×6 in^3) in the laboratory. It was reported that the height/width (h/w) ratio of the specimen influences its peak strength. Generally the peak strength decreases with the increase of the h/w ratio. According to Binda, Mirabella et al. (1996) and Fairhurst and Hudson (1999), an h/w ratio between two and three are recommended so as to secure a uniform stress distribution in the center of the specimen. In this study, one group of granite specimens is $2\times2\times6$ in^3 single prismatic pieces (Figure 3.1a). The other group of specimens is built by superposition of three $2\times2\times2$ in^3 cubic stone pieces (see Figure 3.1b) to reduce the confined effect for the middle cubic stone piece, which has no direct contact with the testing equipment. No additional surface treatment was made for the middle stone piece and the silicon glue was placed between the stones for better stone alignments. Both groups of specimens have the same h/w ratio of 3. All the granite specimens were tested with their natural water content. These granite stones were also used in the construction of granite masonry specimens later.

Figure 3.1: Granite stone specimens: (a) superposition of three cubic units ($2\times2\times2$ in^3), (b) prismatic unit ($2\times2\times6$ in^3)

3.3.2 Cement Mortar

The cement mortar used was made from a pre-mix Portland cement and fine aggregates. The same mortar was used to make the granite masonry specimens later. Two groups of mortar specimens with different geometries were made from the same mix. One group of specimens is cylindrical with 2″ diameter and 4″ long, and the other group is prismatic with dimensions of 2×2×6 in^3. All the specimens were stored and cured at a controlled temperature of 77 ^{o}C and humidity of 75% for more than 28 days following the ASTM specifications (ASTM 2000). Figure 3.2 shows the photos of the mortar specimens.

Figure 3.2: Mortar specimens: (a) cylindrical specimen with 2 in diameter and 4 in long, (b) prismatic specimen of 2×2×6 in^3

3.3.3 Granite masonry specimens

The same granite units and mortar described in the previous sections were used to build up the granite masonry specimens. Each granite masonry specimen has the dimensions of 8×7×5 in^3 which consists of granite units having the dimensions of 8×5×2 in^3 and 5×3.75×2 in^3 (Figure 3.3a). During the construction of the masonry specimens, the joints were filled with mortar and kept at a uniform thickness of 0.5 in. The top and bottom surfaces of the specimens were carefully grinded for a better surface planarity.

These stack bonded masonry prisms were stored and cured at the same environmental conditions as the mortar specimens. The picture of a granite masonry specimen is shown in Figure 3.3b.

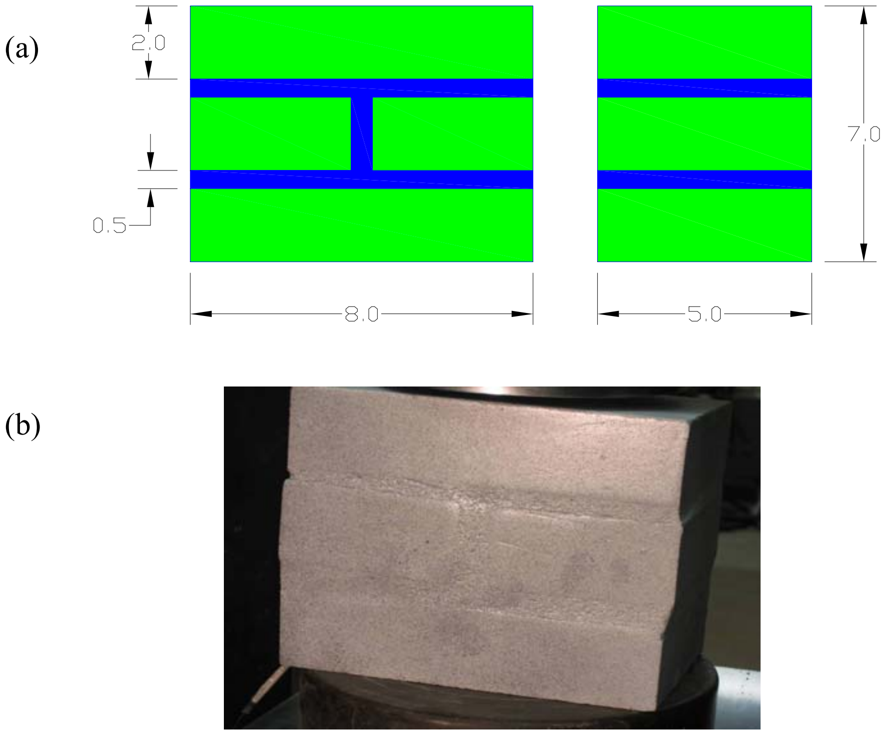

Figure 3.3: Granite masonry specimens tested: (a) geometry (b) actual specimen

3.4. Test Procedure

3.4.1 Compression test

All types of specimens mentioned above were tested using a closed-loop servo-controlled Instron machine as shown in Figure 3.4. An axial LVDT (linear voltage displacement transformer) was placed between the machine platens for the displacement measurement. Before the test, the dimensions of each specimen were measured and recorded. The specimen was then put into the lower platen and carefully centered. This platen has a hinge to prevent any unfavorable effect due to non-parallelism between the top and bottom faces of the specimen. No interposition material between the machine platens and specimen was used. In order to adjust the upper platen to act on the top surface of the specimen, a small compressive preload was applied. The displacement rate was kept at 5×10^{-3} in/s during the test. The axial strain was calculated by dividing the measured change in axial length by the initial axial length of the specimen. The axial compressive stress was computed as the applied load divided by the initial cross-sectional area. In addition to the monotonic increment of the loading, a few samples were also tested under a series of unloading-reloading cycles before reaching the peak stress to acquire more reliable elastic modulus. The unloading branch was performed under displacement control at the same displacement rate.

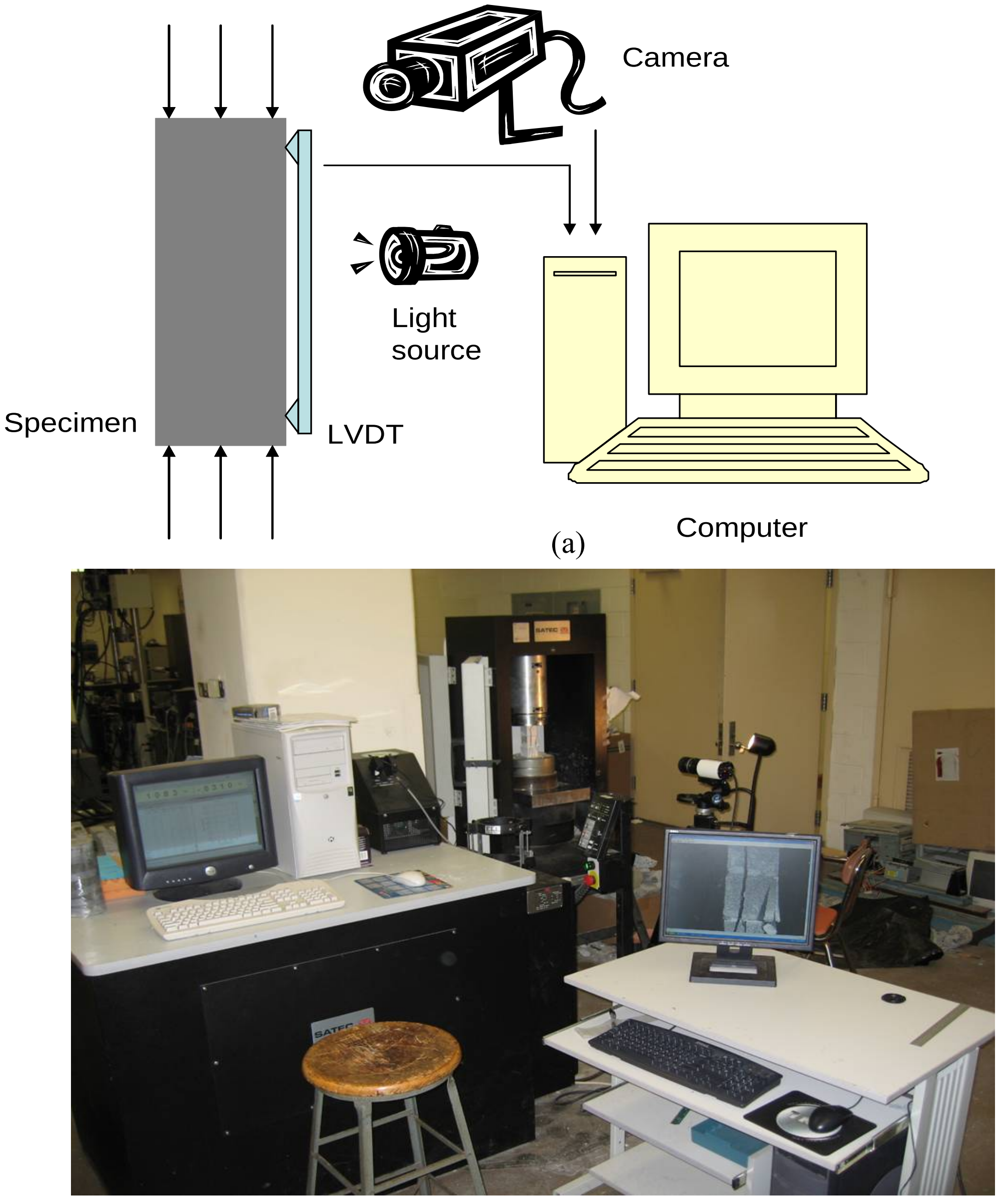

(a)

(b)

Figure 3.4: Experimental setup used in the compression test: (a) schematic setup and (b) photo

3.4.2 Digital Image Correlation Technique

In order to measure the strains in the two-phase granite masonry specimens, the Digital Image Correlation (DIC) technique (Sutton, Wolters et al. 1983; Sutton, Cheng et al. 1986) was applied. The DIC technique is an in-situ optical correlation method used to measure the displacement and strain fields on the surface of an object by tracking a random pattern on the sample surface. Before the test, the pattern was applied by first coating the specimen surface in white paint and then spraying a light mist of black paint in a fine speckle pattern. In the progress of the test, the specimen surface was illuminated using normal white light to provide uniform light intensity across the surface. The camera was placed perpendicular to the specimen surface at a distance of about 6 feet (see Fig. 4b). A reference image was recorded prior to the start of the applied loading. Images were recorded at an equal displacement increment using a 1280 x 1024 pixel CCD camera focused on the specimen surface and linked to a computer for data acquisition. Post-processing of the images was achieved with the software Vic-2D developed by Correlated Solutions (Correlated Solutions) to extract two-dimensional strain fields by comparing every two subsequent image patterns. The accuracy of the measured strain using the DIC method is about 5 x 10^{-5} (Sutton, Wolters et al. 1983; Sutton, Cheng et al. 1986).

3.4.3 Vibrational Resonance Frequency Test

Considering the need of careful equipment setup and surface preparation in obtaining an accurate estimate of the elastic constants (E and v) from the compression test as described in Section 3.4.1, we also conducted vibrational resonance frequency (VRF) tests (Subramaniam, Popovics et al. 2001) on the granite and mortar specimens to verify their elastic constants. This VRF technique requires no special preparation on the specimen surfaces and permits calculation of both E and v from one relatively simple measurement. A cylinder specimen with a length to diameter ratio (L/D) equal to 2 was used in the test. The longitudinal vibrations are introduced by the impact of a 0.2 in diameter steel sphere at the center of one end of the specimen. The resulting vibrations are monitored with a miniature accelerometer that is mounted at the center of the other end from the impact point. The transient signal is acquired from the accelerometer by a digital oscilloscope that is then transferred to a personal computer using the GPIB interface. Figure 3.5 displays the schematic and photo of the experimental setup.

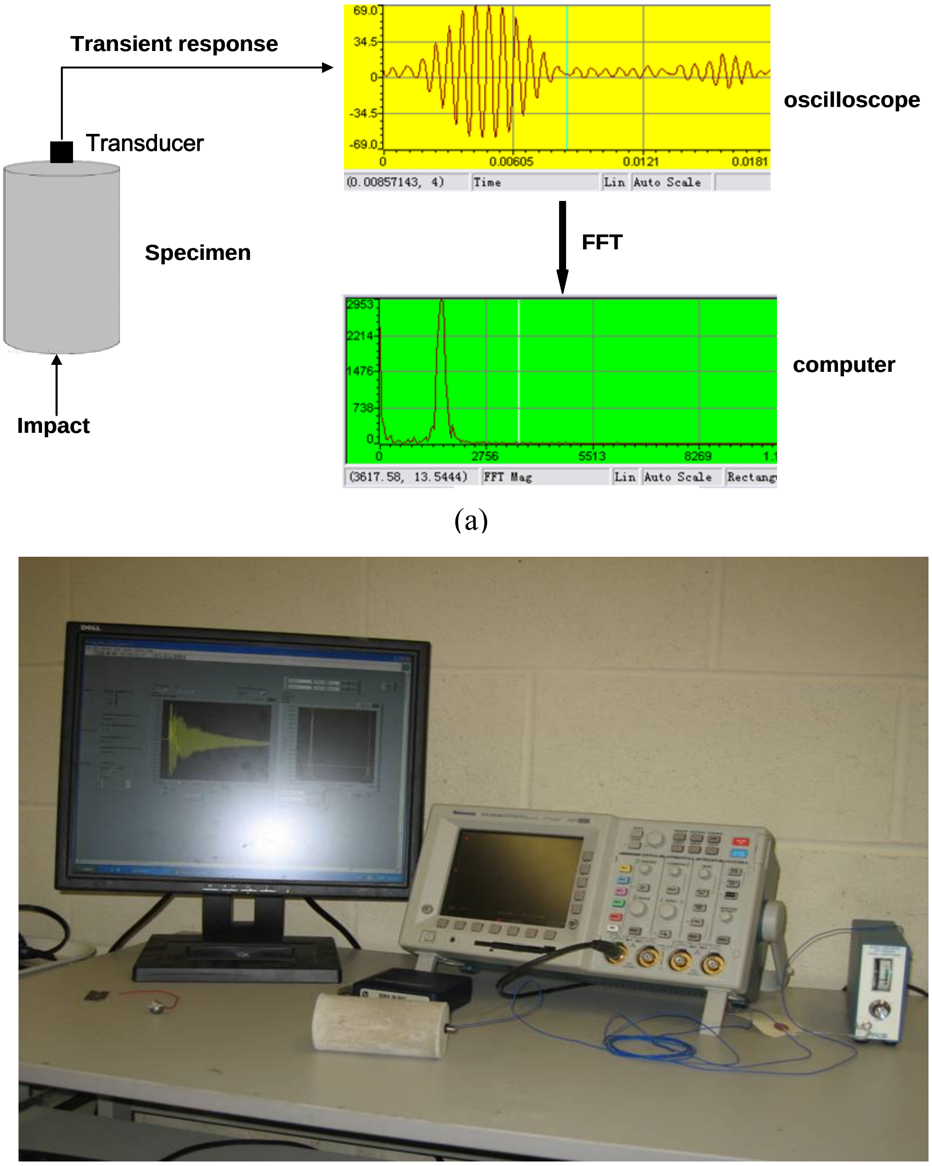

(a)

(b)

Figure 3.5: Experimental setup for vibration resonance frequency test: (a) schematic (FFT picture illustrated only) and (b) photo

The Fourier transform of the time signal is computed using a FFT algorithm. The Poisson's ratio (v) and elastic modulus (E) are functions of the ratio of the second longitudinal resonance frequency to the first longitudinal resonance frequency based on a three-dimensional vibration analysis of intermediate-length cylinders using the Rayleigh-Ritz method (So and Leissa 1997). The equations used are shown as follows (Subramaniam, Popovics et al. 2001):

$$\nu = A_1\left(\frac{f_2}{f_1}\right)^2 + B_1\left(\frac{f_2}{f_1}\right) + C_1 \tag{3.1}$$

$$E = 2(1+\nu)\rho\left(\frac{2\pi f_1 R_o}{f_n^1}\right)^2 \tag{3.2}$$

where f_1 and f_2 are the measured first and second longitudinal resonance frequencies. A_1, B_1 and C_1 are coefficients in terms of L/D ratio and are determined as 1.826, 8.875, and 10.504 respectively in this study. R_o is the radius of the accelerometer, ρ is the material density, and $f_n^1 = A_2\nu^2 + B_2\nu + C_2$, in which A_2, B_2 and C_2 are coefficients in terms of L/D ratio and are determined as 0.309, 0.544, and 1.112 in this study.

3.5. Experimental Results

3.5.1 Granite stone

Figure 3.6 presents a typical stress-strain diagram for granite stone specimens and its corresponding linear fit in the elastic part by the least-squares fitting (Bevington 1969). All the specimens exhibit a common initial adjustment between the specimen and the machine platens. After that, the specimens show a reasonable linear behavior almost until the peak. The stone specimens tested under compressive loading are characterized by high peak strength values and a pronounced fragile behavior. The specimens failed right after reaching the peak strength and the postpeak branch on the stress-strain curve was not observed.

The characterization of the mechanical property based on the results obtained from the compression tests on the granite stone specimens are presented in Table 3.1, where the Young's modulus and the compressive strength of each specimen are listed. It is found that the elastic moduli only have a slight scattering; however the peak strengths scatter more. This can be explained by the differences existing in the stone's nature even though the stones used were from the same delivery. It should also be pointed out that the average Young's modulus and compressive strength of granite found in this study are close to those in the report of (Weidlinger Associates 1996), in which the Young's moduli and the average compressive strength of the masonry towers of the Brooklyn Bridge are 5.8×10^{6} ksi and 7.25 ksi, respectively. The Young's modulus and Poisson's ratio for the granite specimens measured by the VRF test are shown in Table 3.2. Comparing Table 3.1 with Table 3.2, it is found that the obtained average Young's modulus from the VRF test is slightly higher than that from the compression test. In these tables, a small value of coefficient of variations (C.V.) for a measured elastic constant indicates that the property obtained from different samples has little scattering.

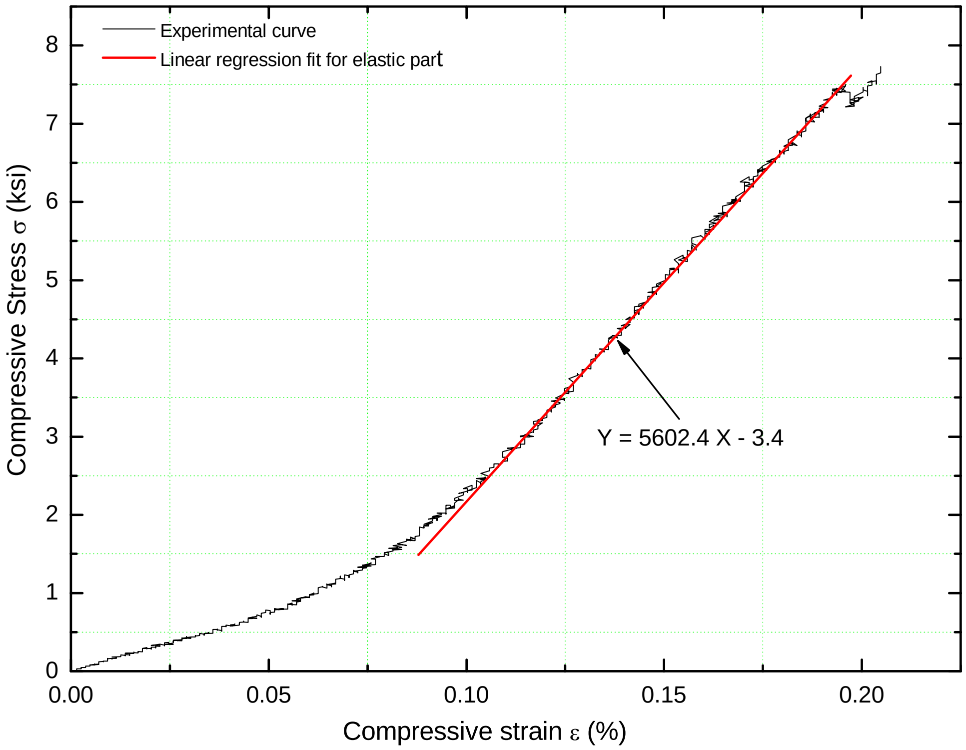
Experimental curve
Linear regression fit for elastic part
Y = 5602.4 X - 3.4
Compressive Stress σ (ksi)
Compressive strain ε (%)
0
1
2
3
4
5
6
7
8
0.00
0.05
0.10
0.15
0.20

(a)

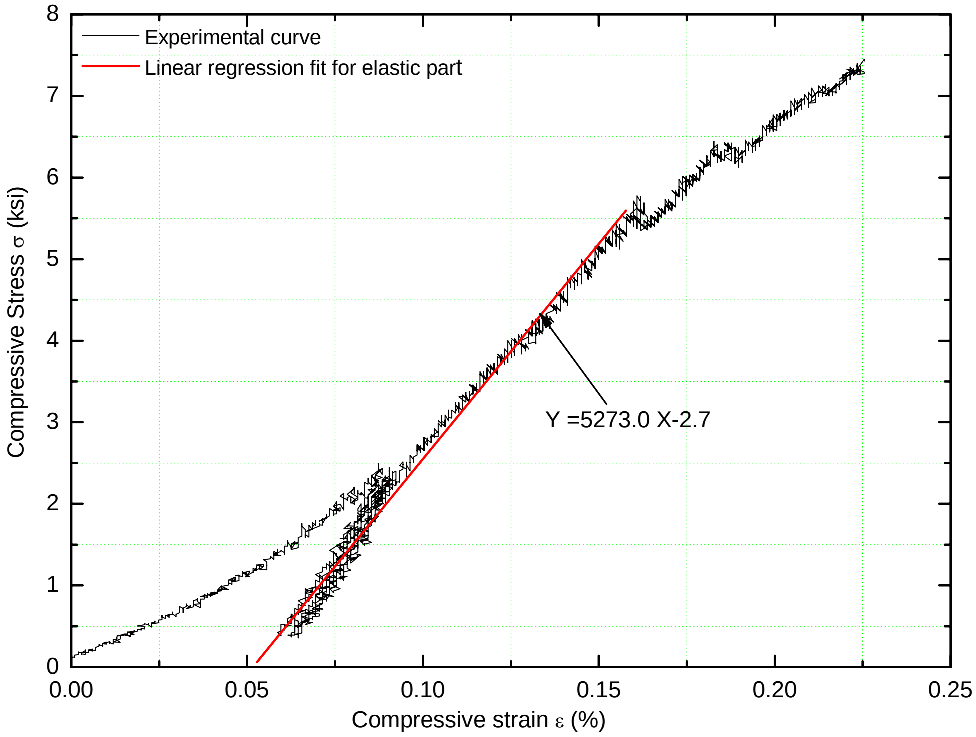
Experimental curve
Linear regression fit for elastic part
Y =5273.0 X-2.7
Compressive Stress σ (ksi)
Compressive strain ε (%)
0
1
2
3
4
5
6
7
8
0.00
0.05
0.10
0.15
0.20
0.25

(b)

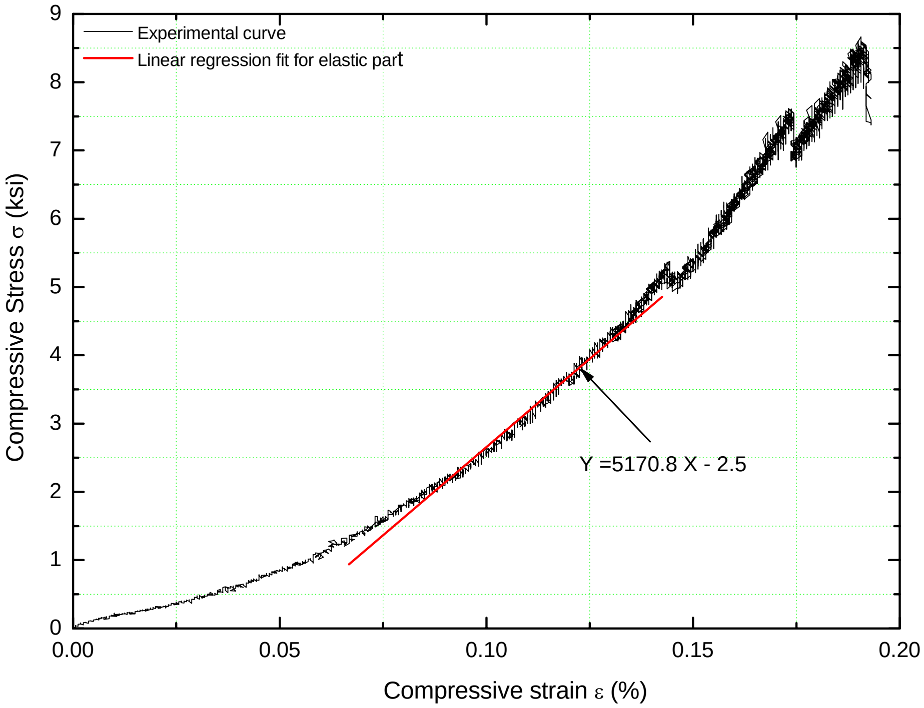

(c)

Figure 3.6: Stress-strain diagrams for three granite stone specimens

Table 3.1: Mechanical characterization of granite stone specimens under uniaxial compression test

Specimen	E (ksi)	σ_{peak} (ksi)
S1	5170.8	9.0
S2	5602.4	7.6
S3	5273.0	7.5
Average Value	5348.7	8.0
C.V.	225.5	0.8

Table 3.2: Poisson's ratio and elastic modulus of granite stone obtained from VRF test

Specimen	Frequency (hz)		Poisson Ratio (ν)	Elastic Modulus *E* (ksi)
	1st	2nd		
G1	17578.120	34545.900	0.113	5483.827
G2	17700.150	34790.040	0.113	5560.028
G3	17606.120	34654.040	0.108	5498.884
Average			0.112	5514.247
C.V.			0.003	40.357

Typical failure modes of the tested granite specimens are shown in Figure 3.7, where continuous vertical cracks from the top to the bottom can be observed from both types of specimens. The specimens composed of three cubic units behave as a whole unit. In some specimens, the cracks formed suddenly and were accompanied by a clear sound. The initial macroscopic cracks were visible only for a load very close to the peak load. In all the specimens tested, the formation of shear bands took place when the peak load was reached and the specimen collapse was due to the cracks developed in the vertical direction. The weak interfacial grain interfaces in the granite unit contributes to the initiation and propagation of the shear bands (Lajtai 1998; Eberhardt, Stead et al. 1999).

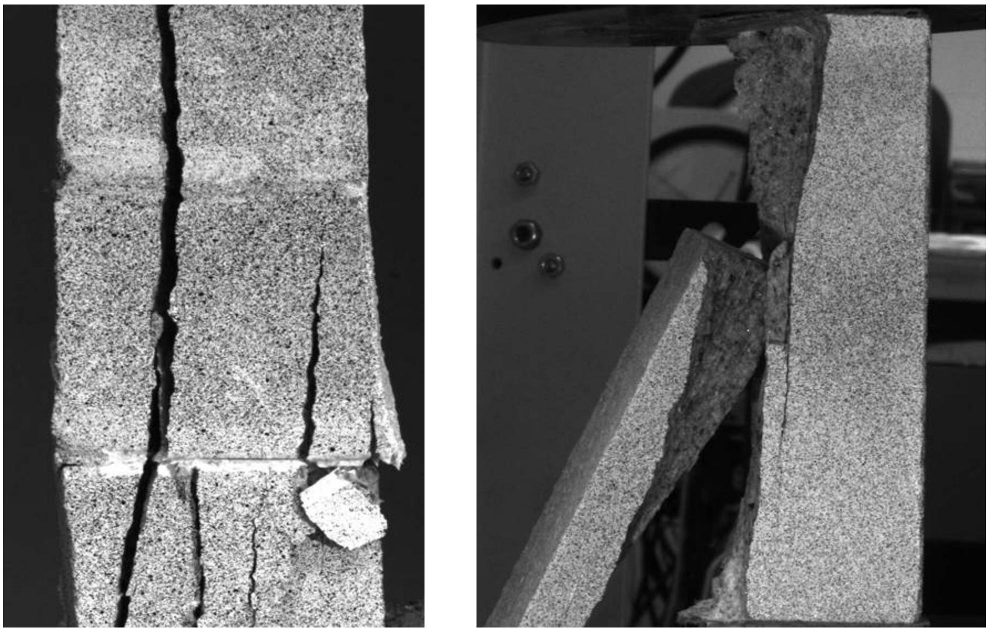

(a) (b)

Figure 3.7: Typical failure mode of granite stone specimens under compressive loading: (a) specimen made of superposition of three cubic units; (b) specimen made of one prismatic unit

3.5.2 Cement Mortar

Figure 3.8 (a-c) display compressive stress-strain curves for three cement mortar specimens and their corresponding linear fit for the elastic part and bilinear hardening part. As observed from Figure 3.8, mortar specimens have much lower peak strengths than the granite stones and exhibit a strain hardening behavior after the linear elastic limit, which indicate that mortar has much more ductile behavior than granite stone. It is noted that the elastic modulus and hardening modulus were obtained by the least squares fitting method with the help of software ORIGIN, in which the nonlinear least squares fitter can fit a function with many parameters. Below and above elastic limit, linear related functions with different slope parameters are assumed for the compressive stress-strain curve. By setting the fitting data range and specifying the confidence level, the nonlinear fitter can fit the data into the desired functions as shown in Figure 3.8.

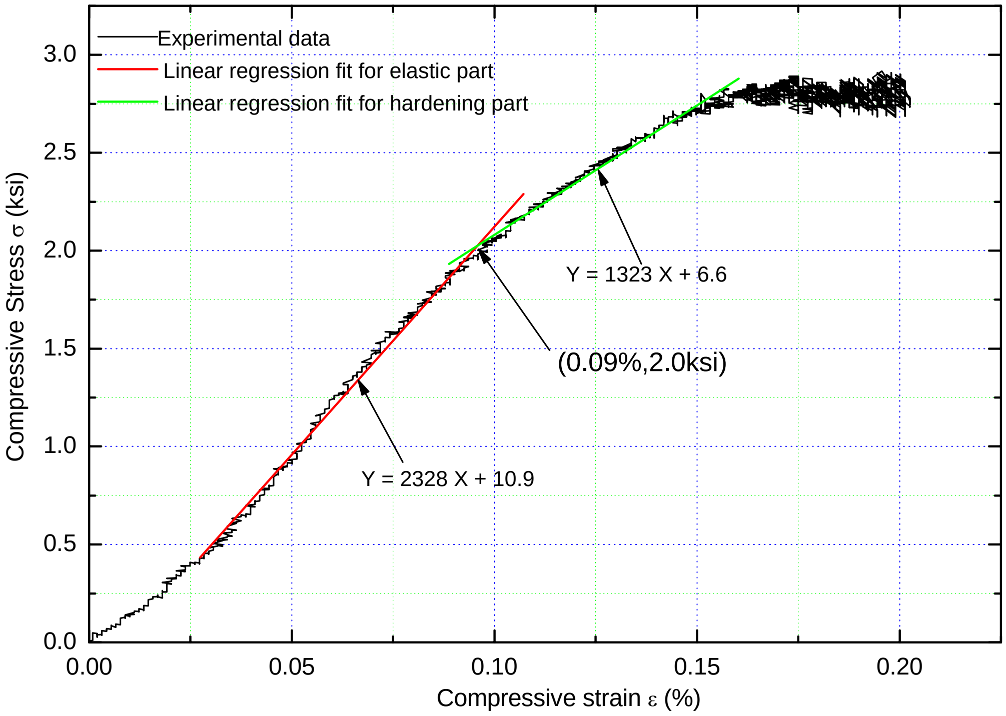

(a)

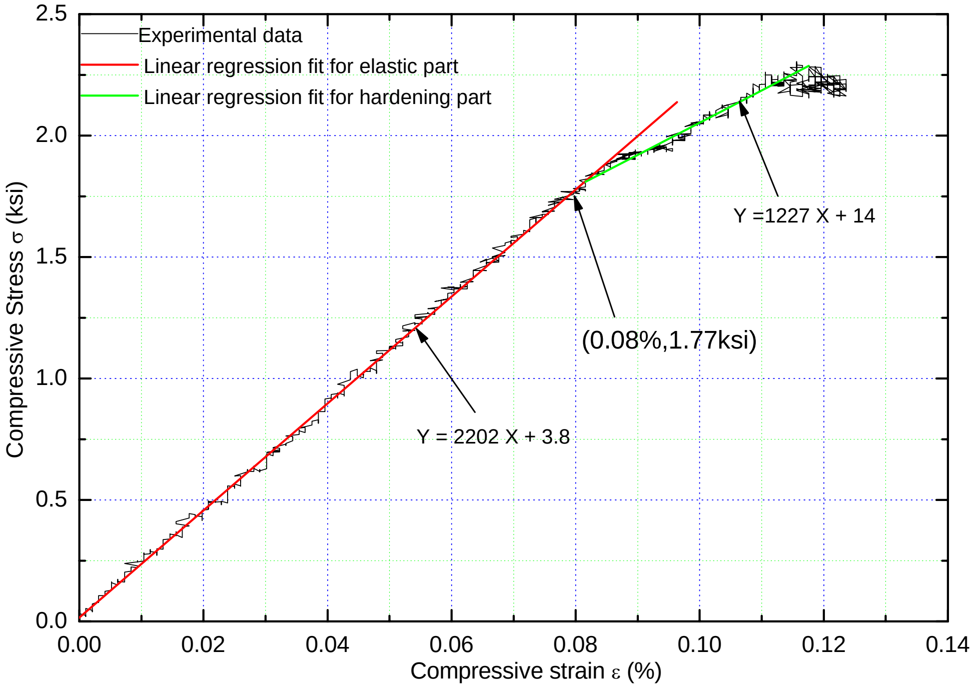

(b)

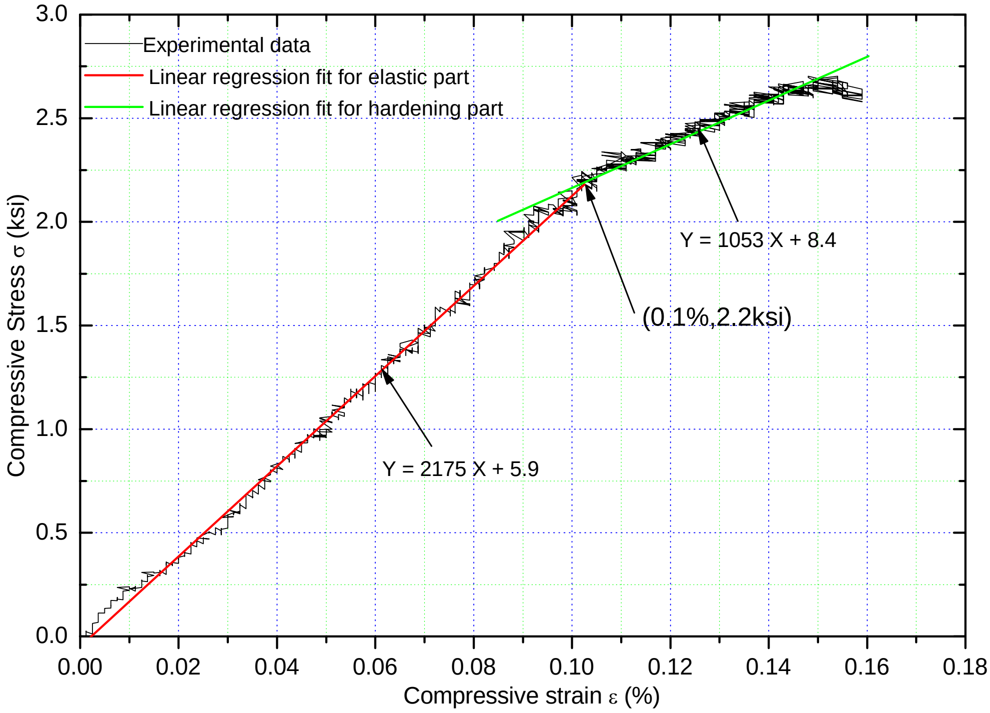

(c)

Figure 3.8: Stress-strain diagrams for three mortar specimens under compressive loading

Table 3.3 summarized the elastic modulus and the peak strength results for the mortar specimens tested under compression. It is noticed from Table 3.3 that less scattering is associated with the mortar specimens for the obtained elastic moduli and peak strength when compared with the results of granite stone (Table 3.1). This is because that the mortar specimens were cast from the same mix and cured at the same curing conditions. The Young's modulus and Poisson's ratio measured by the VRF test are shown in Table 3.4. Comparing the Young's moduli shown in Tables 3.3 and 3.4, similar values were obtained from both approaches, which further confirmed that VRF test is an effective test method for the elastic property measurements. The measured values of Young's modulus for mortar are not available in the report of (Weidlinger Associates 1996), where the Young's modulus is estimated by the formula $E_m = 750 f'_m$ provided by the masonry design code (ACI 1999), in which f'_m is the compressive strength of mortar. As seen in Table 3.3, the ratio of the average Young's modulus (2235ksi) to the peak strength 2.6 ksi) is found to be 860, which is about 15% greater than the coefficient of 750 used in the formula of the masonry design code.

Table 3.3: Mechanical properties of mortar specimens under compression tes**t**

Specimen	Elastic modulus (ksi)	Hardening modulus(ksi)	σ_{peak}(ksi)
S1	2328	1323	2.9
S2	2175	1053	2.7
S3	2202	1227	2.3
Average Value	2235	1201	2.6
C.V.	81.7	136.9	0.3

Table 3.4: Resonance frequencies and material constants of mortar specimens using VRF test

Specimen	Frequency (hz)		Poisson Ratio (ν)	Elastic Modulus E (ksi)
	1st	2nd		
M1	15236.720	29651.020	0.147	2129.2
M2	15402.930	29907.230	0.155	2241.7
M3	15380.860	29918.300	0.148	2151.3
Average			0.150	2174.1
C.V.			0.004	59.6

Typical failure modes of the cement mortar specimens are shown in Figure 3.9. It can be seen that cracks take place at different locations for different geometries. For the cylindrical specimens, diagonal cracks from the bottom to the top are observed. For the prismatic specimens, vertical cracks are visible, which is similar to the failure mode of granite stone. The top and bottom faces of the specimens present no cracks due to the confinement effect provided by the machine platens. The specimen collapse is also due to the occurrence of shear bands and then cracks in the diagonal or vertical direction along the tested specimens.

(a) (b)

Figure 3.9: Typical failure mode for mortar specimens under compressive loading: (a) cylindrical specimen and (b) prismatic specimen

3.5.3 Granite masonry specimens

A typical stress-strain diagram of the granite masonry specimens is presented in Figure 3.10. The stress-strain relation for the masonry specimens exhibits a bilinear, linear elastic and then strain hardening behavior, and present much more ductility than the granite stone and mortar specimens. An initial linear branch is followed by another branch with less stiffness up to a point near the peak. A linear regression fit of the elastic part is also shown in the figure.

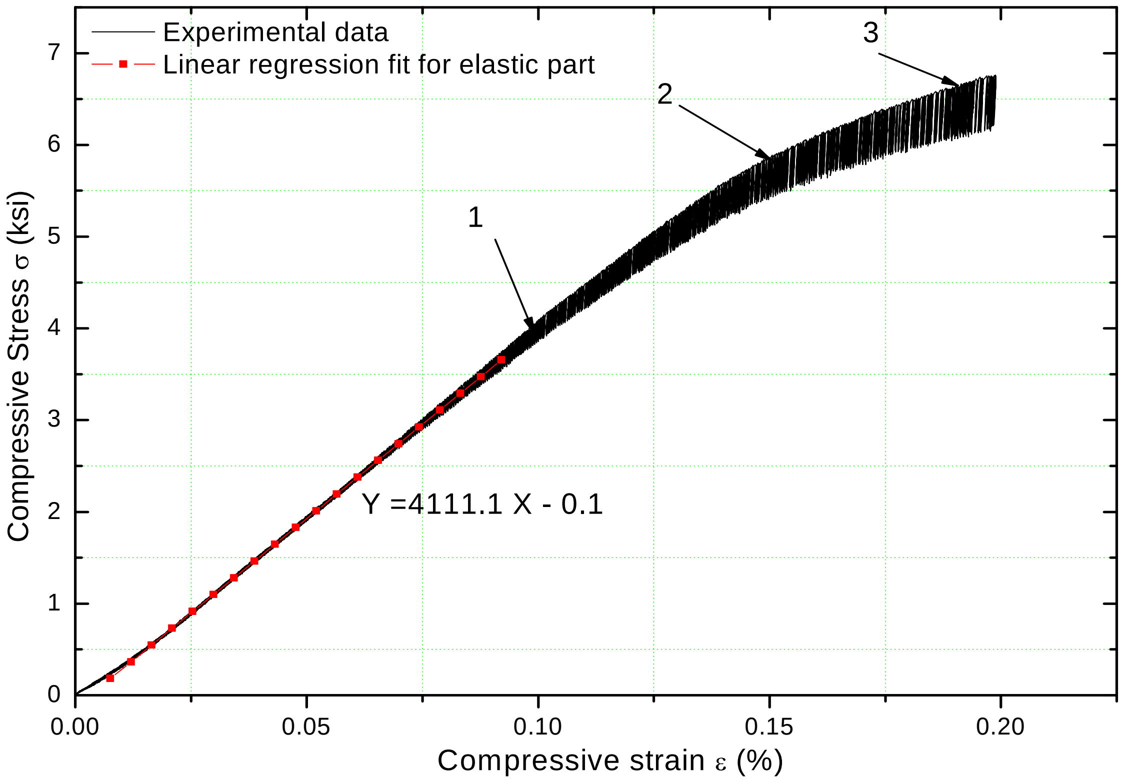

Figure 3.10: Typical stress-strain diagram of the granite masonry specimens under compressive loading

The characterization of the mechanical properties of the granite masonry specimens are tabulated in Table 3.5. The average elastic modulus and compressive strength of the masonry specimens are much less than those of the granite units. The average compressive strength of masonry is found to be 5.9 ksi, which is between the compressive strength of mortar (3.3 ksi) and the compressive strength of granite stone (8.0 ksi). The compressive strength of masonry is highly influenced by the characteristics of the constituent components, granite units and mortar. The increase in the compressive strength compared to the mortar is due to the confined effects provided by the granite units, and the reduction of the compressive strength compared to the granite units can be attributed to the biaxial tension state of the units induced by the shear stresses at the unit-mortar interface when compressive loading is applied.

Table 3.5: Mechanical characterization of granite masonry specimens under compressive loading

Specimen	Elastic modulus (ksi)	σ_{peak} (ksi)
S1	4111.1	6.8
S2	4409.0	5.0
S3	4534.3	5.8
Average Value	4351.5	5.9
C.V.	217.4	0.9

The failure modes obtained from the granite masonry specimens are shown in Figure 3.11. The failure was essentially due to a vertical splitting of the granite units instead of crushing of the mortar, as reported by other researchers (McNary and Abrams 1985; Atkinson, Noland et al. 1985; Binda, Mirabella et al. 1996). In the compression test, the mortar tends to expand laterally more than the granite units due to their different elastic properties. The continuity between the units and mortar, assured by cohesion and friction, creates a lateral confinement to the mortar. As a result, shear stresses develop at the mortar-unit interface, producing a triaxial compression stress state in the mortar and compression-laterally biaxial tension state in the granite units. Consequently, failure generally occurs by the development of cracks parallel to the loading direction in the granite units rather than crushing of the mortar. This is different from what is intuitively predicted.

(a) (b)

Figure 3.11 Failure modes of the granite masonry specimens under compressive loading: (a) perspective view, (b) back view

The Digital Image Correlation (DIC) technology made it possible to measure the strains in the two-phase granite masonry specimens and to record the crack evolution and propagation during the progress of the test. Figure 3.12 shows the DIC images of the tested specimen with the actual image of the specimen along the perimeter, where the contour plots of the strain components ε_{xx}, ε_{yy}, and ε_{xy} at stress states 1, 2, and 3 labeled in Figure 3.10 are presented. These three specific points fall in three different loading stages: linear elastic region, strain hardening region, and next-to-collapse region. Note that the compressive loading is applied in the vertical direction y.

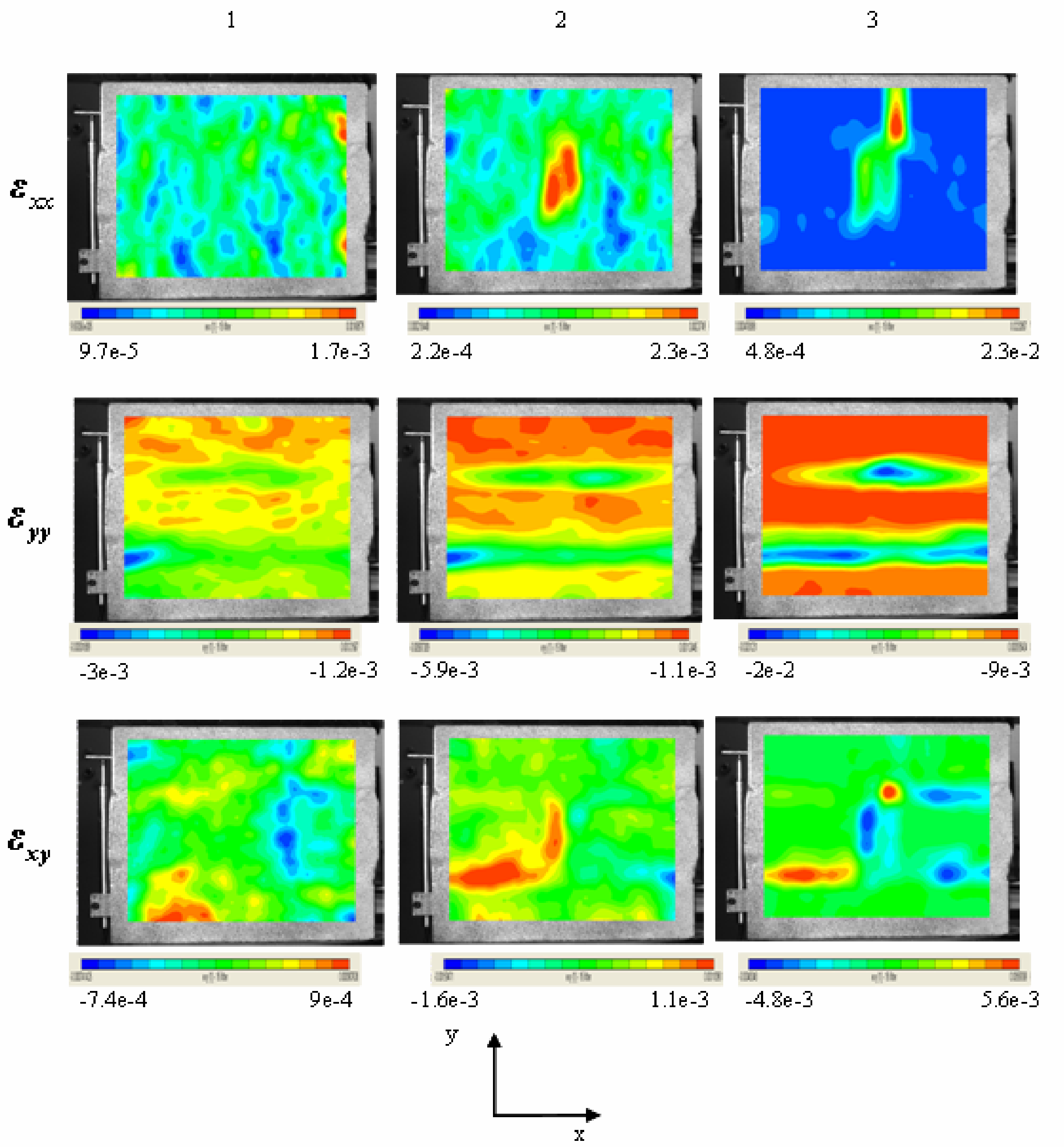

Figure 3.12: The DIC images of the ε_{xx}, ε_{yy}, and ε_{xy} strain components at stress states 1, 2, and 3 labeled in Fig. 10

As seen in Figure 3.12, horizontal stain ε_{xx} and shear strain ε_{xy} distribute irregularly in stage 1 since the masonry prism acts as a whole unit within the elastic range. With the loading increased gradually, we begin to see the appearance of a localized shear band with high shear strain ε_{xy} and horizontal strain ε_{xx} as seen in the strain contours of state 2.

These observations indicate that cracks initiated at the vertical mortar joint and propagated thereafter through the horizontal mortar joint. The initiation of these cracks is due to the formation of multiple shear bands in the mortar-unit interface. Further deformation occurs by extending the shear bands into all the mortar joint layers and finally the granite unit splits vertically due to the laterally biaxial tensile force induced by the mortar joints which are in a triaxial compressive stress state (see the strain contours of state 3).

The strain component ε_{yy} in the vertical direction (loading direction) is analyzed in more detail as shown in Figure 3.13, which displays the evolution of the average strains of ε_{yy} over the specimen width for the three stress states 1, 2, and 3 labeled in Figure 3.10. Average vertical strain ε_{yy} continues to increase throughout the specimen when loading is continuously applied, i.e., from stage 1 to stage 3. As can be seen from the figure, the two horizontal mortal layers in the masonry prism exhibit much higher ε_{yy} than the granite units in every loading stage since the mortar layers have much lower elastic stiffness than the granite units.

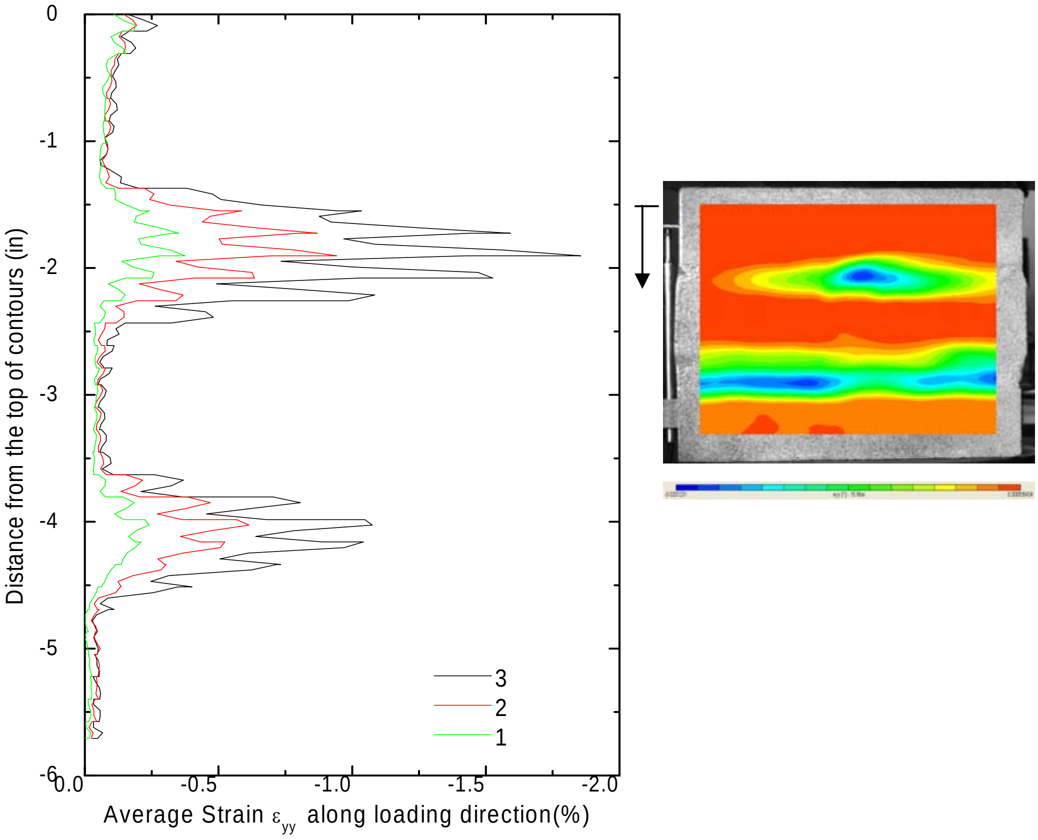

Figure 3.13: (a) Average strain ε_{yy} over the specimen width in three different loading stages, (b) ε_{yy} strain contour of state 3

3.5.4 Equivalent homogenized elastic constants of granite masonry

One of the main purposes of the current study is to find the equivalent homogenized elastic constants for the modeling of the masonry towels of the Brooklyn Bridge. Homogenization techniques are needed for the finite element analysis of large-scale masonry structures especially when seismic or explosive effects are considered because it would not be practical to model block units and mortar joints separately due to a huge amount of computer memory and running time involved. The Finite-Volume Direct Averaging Micromechanics (FVDAM) proposed recently by (Bansal 2005; Bansal and Pindera 2006) is a micromechanics-based model. The analytical framework of the

FVDAM model is based on the local/global stiffness matrix approach and the closed-form expressions derived from the homogenization theory for periodic materials (Paley and Aboudi 1992; Aboudi, Asme et al. 2001). Detail theoretical framework of the FVDAM theory is referred to the literature review in section 2.3.2.1.

To find the equivalent homogenized engineering constants, the geometry of the tested masonry specimens described in section 3.5.3 is divided into 896 subcells as shown in Figure 3.14. The individual material constants for granite stone and cement mortar obtained from the uniaxial compressive tests are input to the FVDAM program. Even though each constituent material, granite stone and cement mortar, is isotropic, the masonry composite after homogenization becomes orthotropic, which has nine independent elastic constants. The calculated homogenized elastic constants based on the FVDAM model are summarized in Table 3.6. The computed elastic constant E_{33} in the vertical direction is 4757 ksi, which is comparable with the value of 4351.5 ksi obtained from the compression test shown in Table 3.5. The experimental elastic modulus is slightly lower than that predicted from the FVDAM model. Inherent local defects in the natural material of the granite masonry, imperfect bonding between granite stones and cement mortar, and workmanship effects may contribute to the difference. Note that the FVDAM model provides elastic constants not only in the vertical direction but also in the other directions which are readily to be used in a finite element analysis of masonry structures.

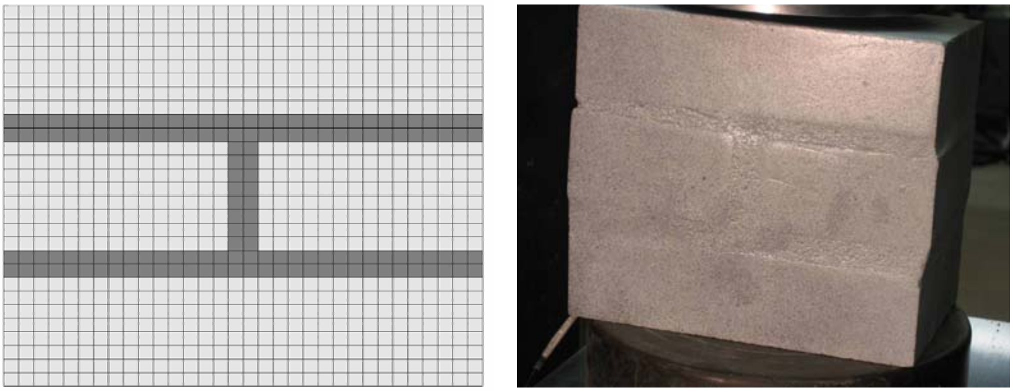

Figure 3.14: The tested masonry specimen (right) and the FVDAM model (left)

Table 3.6: Homogenized material properties obtained from the FVDAM model

E_{11}	E_{22}	E_{33}	G_{23}	G_{13}	G_{12}	v_{23}	v_{13}	v_{12}
5111	4937	4757	1925	1971	2059	0.2	0.2	0.2

Unit: ksi for E and G

3.6. Conclusion

Extensive compressive tests were conducted on granite stone masonry specimens and its constituent components, granite stone units and cement mortar. Vibrational resonance frequency tests were also conducted to measure the elastic constants of the granite units and cement mortar. With the Digital Image Correlation technique, the strain maps of the granite masonry specimens at different loading stages were generated to track crack initiation and propagation in the granite masonry. The conclusions on the results presented in this paper are summarized as follows:

1. The Granite units showed a high strength and fragile behavior with a linear stress-strain relation up to the peak. The specimens failed right after the peak load with

no postpeak branch. Typical failure was due to continuous vertical cracks from the top to the bottom of the specimens. The measured average Young's modulus from the compression tests is 5348.7 ksi and the average peak strength is 8.0 ksi. The average Young's modulus and Poisson's ratio obtained from the vibrational resonance frequency tests are 5514.2 ksi and 0.112 respectively.

2. The strength of the cement mortar is much less than the granite stone. The stress-stain relation includes a linear elastic, strain hardening, and postpeak branch. The failure was due to diagonal cracks for the cylindrical specimens and vertical cracks for the prismatic specimens. The average Young's modulus obtained from the compression tests is 2212.6 ksi which is close to the value measured from the vibrational resonance frequency tests. The measured peak strength is 3.3 ksi.

3. The granite masonry exhibits a bilinear stress-strain relation with an initial linear elastic response followed by a strain-hardening behavior. It presents more ductility than the granite units and mortar specimens. The measured average Young's modulus from the compression tests is 4351.5 ksi and the average peak strength is 5.9 ksi. The failure was essentially due to a vertical splitting of the granite units under the action of biaxial tension rather than crushing of the mortar which was subjected to triaxial compression. The strain contour images obtained from the digital image correlation technique at various loading stages indicate that cracks initiated at the vertical mortar joint and then propagated through the horizontal joints. Finally the granite unit split and the masonry specimen failed.

4. The material properties of the granite units and cement mortar obtained from the compression tests were input to the program developed based on the FVDAM model

to compute the homogenized elastic constants of the granite masonry. The computed Young's modulus in the loading direction is 4757 ksi, which is comparable with the average value obtained from the compression test. The FVDAM model gives also the other eight elastic constants which are required for an overall finite element analysis of a large-scale masonry structure when the masonry is modeled as a homogenized orthotropic material.

Chapter 4: Micro-modeling of Masonry Structures via Micromechanics Approach

---

4.1 Overview

In the last chapter, the individual mechanical behavior of masonry structure constituents (i.e., unit and mortar) was obtained by the compression test. These material properties including elastic properties and yielding will be used to examine the capability of the micro-mechanics based FVDAM model (Bansal and Pindera 2006) in predicting the macroscopic response of masonry structure if the individual mechanical behavior of its constituents (i.e., unit and mortar) is known. Currently, the plastic analysis capabilities of the FVDAM model are limited to model the bilinear hardening materials such as metals in the composite constituents. However, mortar joints and block units as constituents of masonry structures are usually modeled as Mohr-Coulomb material. Hence, a plastic algorithm based on the Mohr-Coulomb failure criterion was developed in the FVDAM model to simulate the constituents of the masonry, i.e., cement mortar and granite unit. The FVDAM theory is first validated through comparison with finite-element results, demonstrating that FVDAM can predict macroscopic behavior of composite material and local stress fields with accuracy approaching that of the finite-element method. Then the FVDAM model was applied to masonry structure, which is a two-phase composite composed of mortar and unit (stone, brick, or block), at the first time. The extensive parametric analysis was performed to understand the effect of the mesh size, cell texture, mortar elastic modulus and mortar volume fraction on the homogenized/effective elastic properties. It was found that mesh size and texture of the repeating unit cell (RUC) has little influence on the effective elastic properties of the masonry composites. However, the mortar elastic modulus and the mortar volume fraction affect the overall effective stiffness of the masonry composite significantly. Finally, elasto-plastic analyses were carried out on the granite masonry structure to compare with the experimental results. The well experimental-analytical correlation confirmed the capability of the FVDAM model in predicting the response of masonry structure. The initiation and evolution of effective plastic strain distributions was also obtained when the masonry structure is subjected to uniaxial compressive loading. It was found that plastic zone initiates and propagates through mortar layers and finally the masonry structure fails until mortar failure.

4.2. Introduction

A masonry structure can be considered as a two-phase composite medium composed of mortar and masonry units (stone, bricks, or blocks), normally arranged periodically. For periodic composite materials, the homogenization techniques represent a powerful tool and are getting more and more attention among the masonry community because the techniques are needed for the analysis of large-scale masonry structures, especially when seismic or explosive loads are involved. A number of homogenization techniques have been developed in the past to derive average homogenized properties of masonry from the behavior of each constituent material. In general, three types of approaches have been developed for homogenization. The first approach is to use a simplified layer geometry to represent the basic cell and use the volume ratio of masonry units to mortar joint to estimate the equivalent homogenized material properties (Pande, Liang et al. 1989; Pietruszczak and Niu 1991). The homogenization has generally been performed in two steps, head (vertical) and bed (horizontal) joints being introduced successively , however its result depends on the sequence of the successive steps (Papa 1996), which means that the procedure is not objective, even in a linear elastic analysis.

The second approach is based on the micromechanics theory and to employ a representative volume element (RVE) to calculate the equivalent elastic constants and failure modes of masonry material with the help of finite element software (Ma, Hao et al. 2001; Wu and Hao 2006). Both the units and mortar joints are idealized as isotropic material having their own properties such as stiffness, strength, and damage characteristics. Based on the numerical results, the equivalent material properties are used as the homogenized material properties in numerical simulation of a full masonry structure based on the continuum approach. However, the approach is not analytical and relies on the commercially available FEM software. In fact, the plastic behavior for the individual brick and mortar are still not well known very well and lot of scattering have been observed in the mechanical test of masonry specimens. Thus the applicability of the continuum model based on the RVE model is still limited.

The third approach is also based on a micromechanics concept, in which a repeating unit cell (RUC) containing all the individual components is employed (Aboudi 1989; Anthoine 1995; Anthoine 1997). These two concepts (RVE and RUC) are based on different geometric representations of heterogeneous microstructures and require different boundary conditions in the micromechanical analysis of the smallest material subvolume. In particular, micromechanical analysis of an RVE is based on the homogeneous traction and displacement boundary conditions, while micromechanical analysis of an RUC is based on periodic displacement and traction boundary conditions.

Recently, (Bansal and Pindera 2006) reconstructed a micromechanics-based model called Finite-Volume Direct Averaging Micromechanics (FVDAM), which was developed from the higher-order theory for periodic heterogeneous materials (Aboudi, Asme et al. 2001). The analytical framework of the FVDAM model is based on the local/global stiffness matrix approach and the closed-form expressions derived from the homogenization theory for periodic materials. The FVDAM model shares some similarities with the finite-element method, while also possessing distinct differences. The formation of local and global stiffness matrices is common to both approaches. The continuity of displacements and forces imposed at the nodes in the finite-element technique is replaced by the continuity of displacements and tractions imposed at the subcell interfaces in the FVDAM model. The FVDAM model has simplified the theoretical framework and substantially increased its computational efficiency, enabling analysis of unit cells with realistic multiphase microstructures previously unattainable in the original formulation developed by (Aboudi, Asme et al. 2001). The capability of the FVDAM model predicting macroscopic and microscopic response of metal composites such as boron/aluminum composites has also been verified through experimental data (Bansal and Pindera 2006). However, currently the plastic analysis of FVDAM is still limited to the bilinear hardening materials such as metals. In this study, the plastic modeling capacity of the FVDAM also has been further extended to the more complex material such as piece-wise continuous materials by updating the corresponding plastic strain increment during the different loading stages.

In the following sections, the plastic theoretical development of the FVDAM model will be introduced first. The accuracy and efficiency of the FVDAM model predicting mechanical behavior of composite material was validated by comparing with FEM results from the commercial software Femlab (Femlab 2004). Then the FVDAM model was applied to masonry structure composed of granite stone and cement mortar at the first time. The extensive parametric analysis was made to under the effect of the mesh size, cell texture, mortar elastic modulus and mortar volume fraction on the homogenized/effective elastic properties. Finally, elasto-plastic analyses were carried out on the granite masonry structure to compare with the experimental results.

4.3. Plastic Theory formulation for FVDAM model

The plastic strains are determined by solving Equations (2.23) and (2.24) of the applied macroscopic strain when classical incremental plasticity theory is employed (Mendelson 1983). The plastic strain field in the (*β*, *γ*) subcell at the current load level expressed in terms of the known initial distribution from the preceding loading state plus an increment that results from the imposed load increment:

$$\varepsilon_{ij}^{p(\beta,\gamma)}\left(\bar{x}_2,\bar{x}_3\right)|_{current}=\varepsilon_{ij}^{p(\beta,\gamma)}\left(\bar{x}_2,\bar{x}_3\right)|_{previous}+d\varepsilon_{ij}^{p(\beta,\gamma)}\left(\bar{x}_2,\bar{x}_3\right) \tag{4.1}$$

where the plastic strain increment $d\varepsilon_{ij}^{p(\beta,\gamma)}$ is proportional to the stress gradient of the yielding surface function ,which is termed the normality rule (Hill 1950) .

$$d\varepsilon_{ij}^{p}=d\lambda\frac{\partial f}{\partial\sigma_{ij}} \tag{4.2}$$

In which $d\lambda$ is the plastic multiplier derived from the yielding surface function $f\left(\sigma_{ij},\tau\right)=0$:

$$d\lambda = \frac{\frac{\partial f}{\partial \sigma_{ij}} C_{ijkl} d\varepsilon_{kl}}{\frac{\partial f}{\partial \sigma_{ij}} C_{ijkl} \frac{\partial f}{\partial \sigma_{kl}} - \frac{\partial f}{\partial \tau} \frac{\partial \tau}{\partial \varepsilon_{ij}^{p}} \frac{\partial f}{\partial \sigma_{ij}}} \tag{4.3}$$

Where

$$\frac{\partial \tau}{\partial \varepsilon_{ij}^{p}} = H' \cdot \frac{\sigma_{ij}}{\tau} \tag{4.4}$$

in which H' is the hardening function which can be determined experimentally from a simple uniaxial yield test.

In this study the plastic analysis capabilities of FVDAM is not just limited to von-Mise material and has been further extended to the Mohr-Coulomb material such as concrete, rock and soil materials by incorporating the yielding function of the Mohr-Coulomb criterion (Owen and Hinton 1980).

$$f = \frac{1}{3} I_1 \sin(\phi) + (J_2)^{\frac{1}{2}} \left(\cos(\theta) - \frac{1}{\sqrt{3}} \sin(\theta) \sin(\phi) \right) - c\cos(\phi) \tag{4.5}$$

where I_1 is the first stress invariants, J_2 is the second invariants of the deviatoric stress, angle θ is defined in the Mohr-Coulomb yield surface (see Figure 4.1), c is cohesion strength and ϕ is the frictional angle.

For the Mohr-Coulomb model, the hardening function is defined as:

$$H' = \left(\frac{1 - \sin(\phi)}{2} \right)^2 \cdot \frac{E_T}{1 - E_T / E} \tag{4.6}$$

where E_T is the tangent modulus, friction angle φ is obtained by:

$$\sin(\phi) = \frac{f_c' - f_t'}{f_c' + f_t'} \tag{4.7}$$

in which, f_c' is the compression yielding stress and f_t' is the tensile yielding stress.

The cohesion strength c is achieved by this expression:

$$c = \frac{f_c' f_t'}{f_c' - f_t'} \tan\phi \tag{4.8}$$

For the micro-modeling of the masonry structure in this study, granite unit and mortar joints are assumed to be homogeneous and isotropic material. Perfect bonding between granite unit and mortar joint is also assumed. In the FVDAM model, the granite units are regarded as elastic material throughout the compression loading process since the granite unit has much higher strength than the mortar joints. The mortar joints are modeled as Mohr-Coulomb material. The elastic moduli for both granite stone and mortar joints are obtained by the compression test as described in the last chapter and the Poisson's ratios for granite and mortar are assumed to be 0.2. The hardening modulus E_T and compressive yielding strength f_c' for the mortar joints are also obtained by the compressive test and its tensile yielding strength f_t' are assumed to be 10% of its compressive strength. Through this procedure, the plastic parameters *c*, ϕ and H' for the mortar joints can be obtained from Equations (4.6 - 4.8).

The convergence of the iterative process for updating the total plastic strains within each subcell is based on the convergence of the effective plastic strain increment $d\varepsilon_{ij}^{p(\beta,\gamma)}\left(\overline{x}_2,\overline{x}_3\right)$ evaluated at each subcell. Specifically, the difference in the effective plastic strain increments at the k_{th} and $(k+1)_{th}$ iterations at the same point $(\overline{x}_2,\overline{x}_3)$ in the (*β*, *γ*) subcell,

$$\Delta d\overline{\varepsilon}_k^{p(\beta,\gamma)}(\overline{x}_2,\overline{x}_3) = \left|d\overline{\varepsilon}_{k+1}^{p(\beta,\gamma)}(\overline{x}_2,\overline{x}_3) - d\overline{\varepsilon}_k^{p(\beta,\gamma)}(\overline{x}_2,\overline{x}_3)\right| \tag{4.9}$$

is used to determine the maximum difference $\Delta d\overline{\varepsilon}_{k,\max}^{p(\beta,\gamma)} = \max[\Delta d\overline{\varepsilon}_k^{p(\beta,\gamma)}(\overline{y}_2^{(\beta)},\overline{y}_3^{(\gamma)})]$ between two successive effective plastic strain increments at all the considered integration points within the (*β*, *γ*) subcell. This maximum difference $\Delta d\overline{\varepsilon}_{k,\max}^{p(\beta,\gamma)} = \max[\Delta d\overline{\varepsilon}_k^{p(\beta,\gamma)}(\overline{x}_2,\overline{x}_3)]$ is then compared with the average effective plastic strain increment $d\overline{\varepsilon}_{k,av}^{p(\beta,\gamma)}$=mean $[d\overline{\varepsilon}_k^{p(\beta,\gamma)}(\overline{y}_2^{(\beta)},\overline{y}_3^{(\gamma)})]$at the $(k+1)_{th}$ iteration. Convergence is assumed to be achieved when

$$\Delta d\overline{\varepsilon}_{k,\max}^{p(\beta,\gamma)} \leq 0.02\times\ d\overline{\varepsilon}_{k,av}^{p(\beta,\gamma)} \tag{4.10}$$

For the different material in the composites, the plastic strain increment in Equation (4.3) has to be updated in each iteration following its individual constitutive relationships. For bilinear hardening material, the effective stress $\overline{\sigma}(\overline{\varepsilon}^p)$ is given by

$$\overline{\sigma}(\overline{\varepsilon}^p) = \sigma_y + H'\overline{\varepsilon}^p \tag{4.11}$$

where σ_y is the yield stress and H' is the slope of the effective stress-plastic strain curve, related to the secondary modulus E_s in the bilinear stress-strain representation of the elastoplastic response as follows

$$H' = \frac{E\,E_s}{E - E_s} \tag{4.12}$$

For more complex material such as piece-wise continuous materials, the corresponding plastic strain increment during the different loading stages is updated according to the stress-strain relationship of the individual material.

4.4. Model validation

The mathematical formulation of the FVDAM model has been presented in the previous section. Validation of model's capability will be demonstrated in this section by comparing the results of masonry repeating unit cells with those obtained from finite-element analysis using software FEMLAB (Femlab 2004).

In order to use the FVDAM model to compute the mechanical properties of a masonry structure, the definition of an appropriate repeating unit cell (RUC) is required. An RUC of masonry should satisfy the following conditions (Ma, Hao et al. 2001): (1) including all the participant materials, (2) constituting the entire structure by periodic and continuous distribution, and (3) being the minimum unit satisfying the first two conditions. For the typical masonry structure shown in Figure 4.1 (a), two possible different cell textures (RUC I and RUC II), as shown in Figure 4.1(b) and 4.1(c), can be used to represent the masonry. In the figure, these two cell textures are divided into

40×40 subcells with equal dimensions. The cell texture effects on the homogenized material properties will be discussed in section 4.5.1.

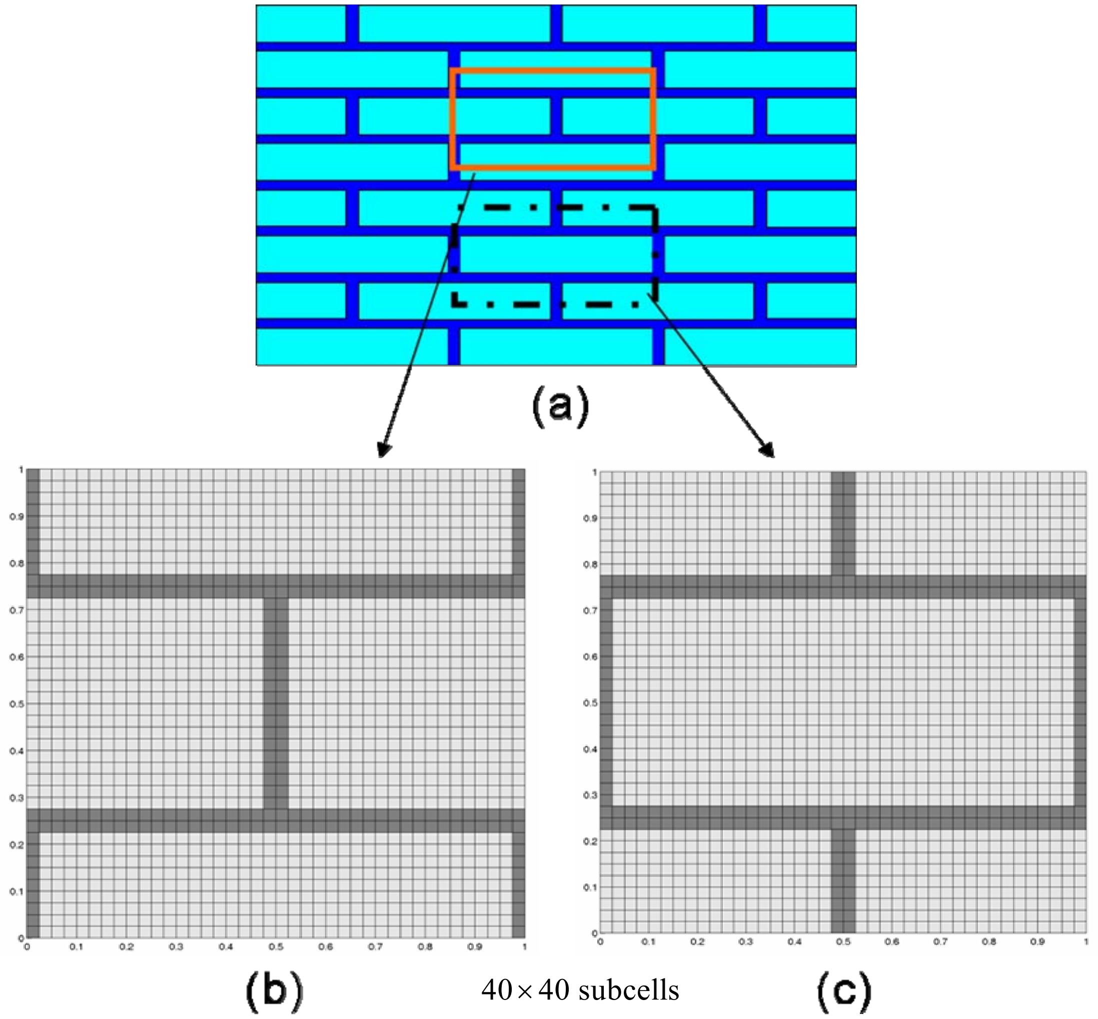

Figure 4.1: (a) Typical masonry structure composed of masonry unit and mortar, (b) Repeating unit cell I, and (c) Repeating unit cell II.

To verify the FVDAM model, RUC I is subject to a uniform vertical displacement with biaxial constraints in the other two directions such that ε_{33} = constant and $\varepsilon_{11} = \varepsilon_{22} = 0$. The mechanical properties of the granite stone and cement mortar used in the analysis are from the experimental results of (Zeng, Lin et al. 2009) and are given in Table 4.1. Figure 4.2 presents the comparison of macroscopic stress-strain curves obtained from the

FVDAM model and finite element analysis. As seen in the figure, the masonry unit experiences a hardening behavior following the elastic response, which is consistent with the experimental observation (Zeng, Lin et al. 2009). The macroscopic stress-strain responses predicted by the FVDAM and finite-element models are very close to each other. Figure 4.3 displays the comparison of the von-Mises stress field distributions within the unit cell obtained from the FVDAM and finite element models. It is observed that the von-Mise stress distribution from the FVDAM model approaches the result of the finite element prediction. If a more refined mesh of the unit cell is used, an even better match can be generated. The figure also shows that the internal stresses in the granite units are much higher than those in mortar layers, which is due to the larger stiffness of the granite stone. These comparisons confirm the accuracy of the FVDAM model in predicting the elasto-plastic behavior of the multiphase composite material and demonstrate that the FVDAM model provides a powerful tool which can be used in understanding mechanical behavior of multiphase materials

Table 4.1: Input elastic and plastic parameters of granite stone and cement mortar

Material	E (ksi)	ν	G (ksi)	σ_y (ksi)	E_s (ksi)
Granite	5602.4	0.2	2334.3	8.0	N/A
Mortar	2212.6	0.2	921.9	2.2	542

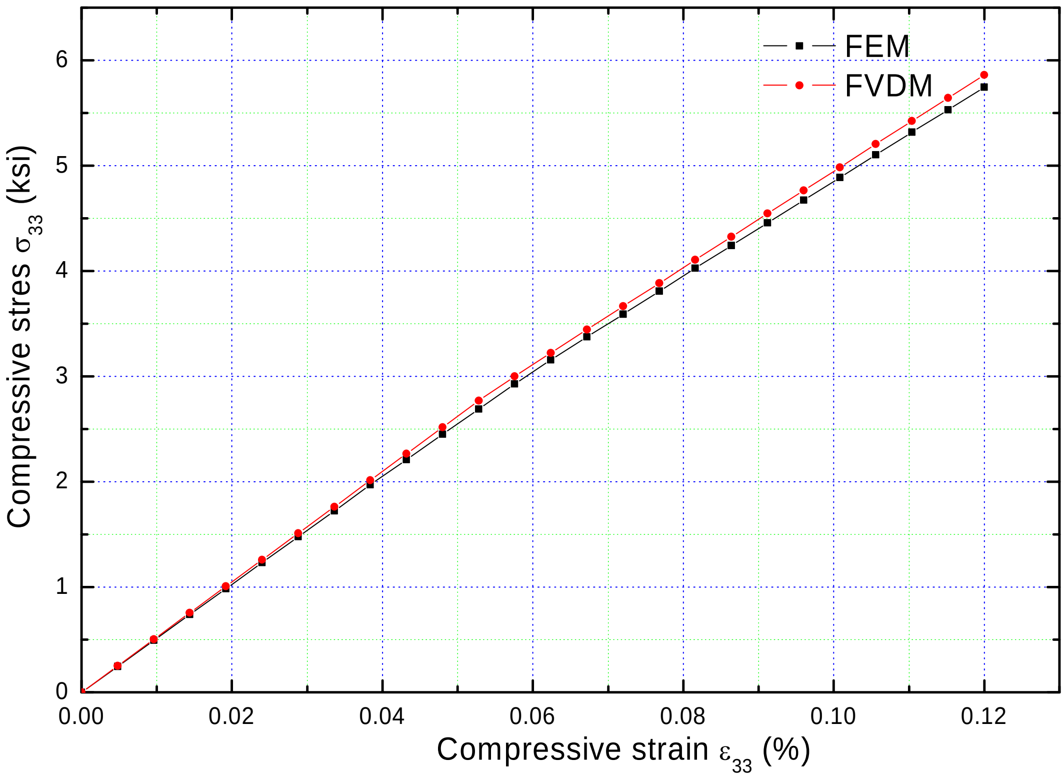

Figure 4.2: Comparison of macroscopic stress-strain response of masonry unit cell using the FVDAM model and finite element analysis. The unit cell is subject to a vertical uniform displacement with the other two directions constrained.

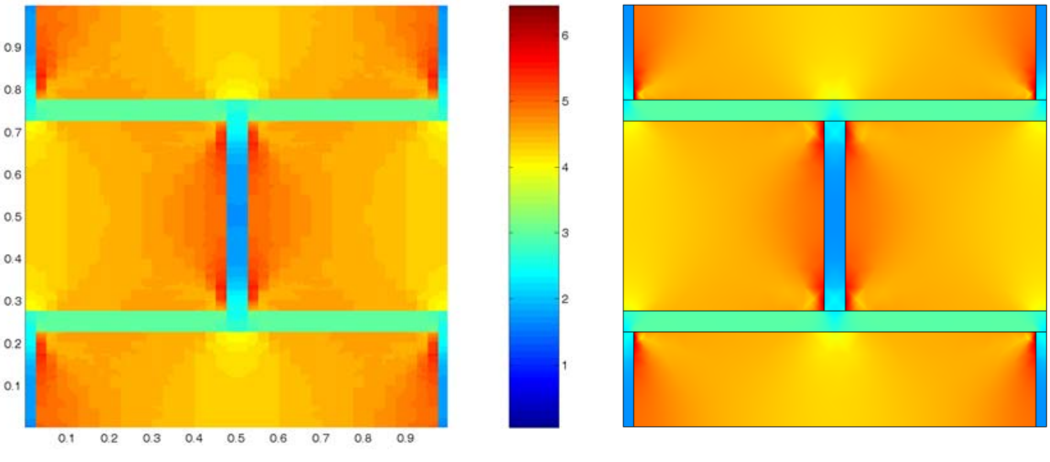

FVDAM unit:ksi FEM

Figure 4.3: Comparison of von-Mise stress distributions in a masonry unit cell using the FVDAM model and finite element analysis at $\varepsilon_{33} = 0.12\%$ and $\varepsilon_{11} = \varepsilon_{22} = 0$.

To check the size effect of RUC on the local field quantities, a 2X2 matrix formed by the RUC I is employed, as shown in Figure 4.4. Same boundary conditions are applied. It is found from Figure 4.4 that same effective stress contours from the Unit I was observed (see Figure 4.3) and periodic mechanical behavior exhibits for the periodic microstructure.

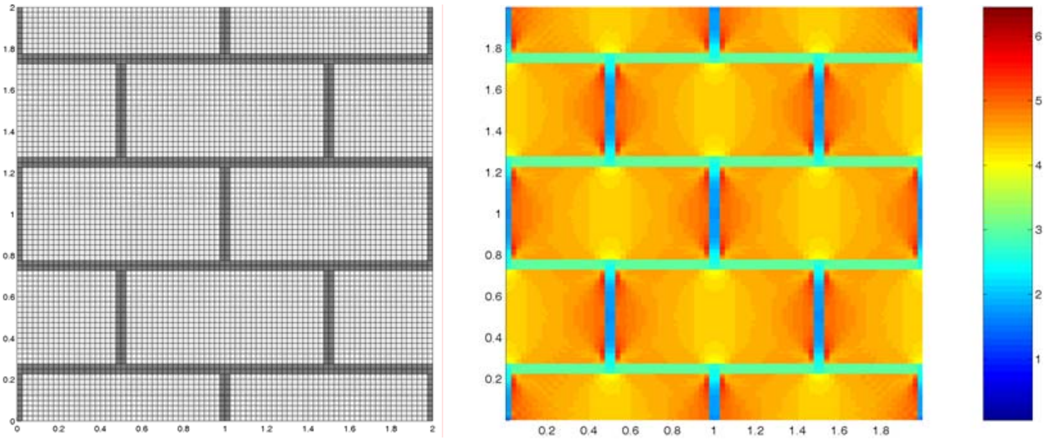

Figure 4.4 (a) A 2×2 matrix formed by RUC I, and (b) its von-Mises stress distribution at $\varepsilon_{33} = 0.12\%$ and $\varepsilon_{11} = \varepsilon_{22} = 0$.

4.5. Application to masonry structures

Extensive parametric analyses of the repeating unit cells are performed to understand the effects of mesh size, cell texture, material elastic modulus, and mortar volume fraction on the homogenized equivalent elastic properties. Elasto-plastic analyses are also carried out on the masonry unit cell to have the results compared with experimental data.

4.5.1 Mesh size sensitivity and cell texture effect

In order to investigate the effects of mesh size and texture of the unit cell on the homogenized equivalent elastic properties, both RUC I and RUC II are analyzed with a discretization of 40×40 subcells (Figure 4.1) and a finer discretization of 80×80 subcells as shown in Figure 4.5. The individual elastic material properties for granite stone and cement mortar are listed in Table 4.1. Even though each constituent material, granite stone and cement mortar, is isotropic, the masonry composite after homogenization becomes orthotropic, which has 9 independent elastic constants. The calculated homogenized elastic constants based on the FVDAM model using RUC I and RUC II are summarized in Table 4.2.

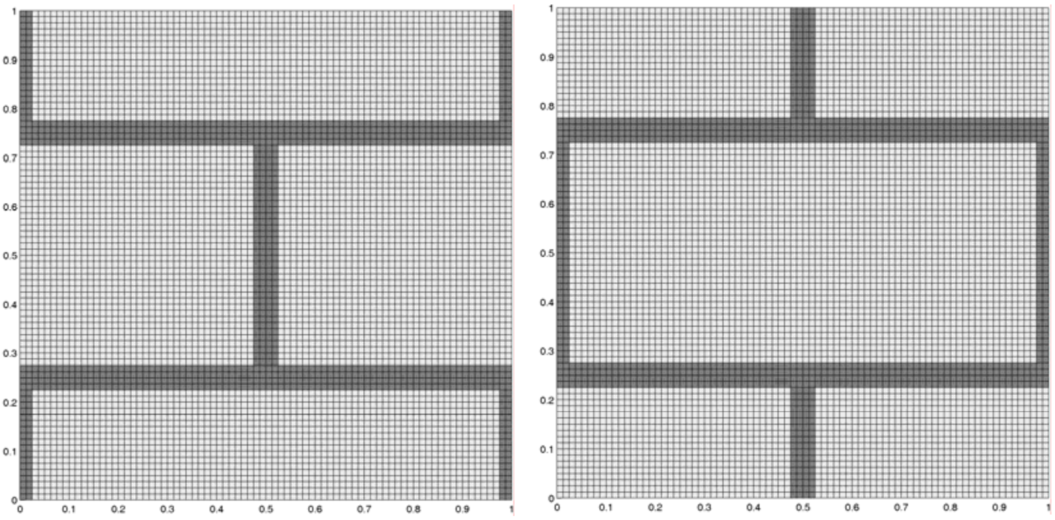

80×80 subcells

Figure 4.5: Finer subcell discretization of RUC I and RUC II

Table 4.2: Homogenized material properties obtained from the FVDM model

RUC	Mesh size	E_{11}	E_{22}	E_{33}	G_{23}	G_{13}	G_{12}	v_{23}	v_{13}	v_{12}
I	40×40	5111	4937	4757	1925	1971	2059	0.2	0.2	0.2
I	80×80	5108	4933	4751	1921	1968	2057	0.2	0.2	0.2
II	40×40	5111	4935	4757	1923	1971	2057	0.2	0.2	0.2
II	80×80	5111	4936	4757	1923	1971	2058	0.2	0.2	0.2

Unit: ksi for all the moduli in the table

As observed in Table 4.2, all the engineering constants from both types of repeating unit cells with different subcell mesh refinements are almost identical, which indicates that the numerical results obtained from either RUC I (40×40) or RUC II (80×80) can represent the homogenized material properties and even the coarser subcell mesh (40×40) can produce a reliable result from the FVDM model. Thus, all the subsequent calculations are performed using the RUC I subcell discretization. When comparing the homogenized material properties with the individual elastic properties of granite stone and cement mortar (Table 4.1), it is found that the homogenized Young's moduli and shear moduli are close to the properties of the granite stone, which is reasonable since the mortar volume fraction (14.5%) is small in this case. The homogenized Poisson's ratios have the same value as that of each constituent, which is expected since both constituents have the same value of Poisson's ratio.

4.5.2 Effect of mortar modulus

To investigate the effects of mortar moduli on the homogenized equivalent material properties of the repeating unit cell, the material properties of the granite stone are kept constant whereas the properties of the mortar are varied. Different stiffness ratios of granite stone to mortar are considered in the analysis. Figure 4.6 shows the plots of the ratios of Young's modulus of granite stone to Young's modulus of mortar (E_g/E_m) ranging from 1 to 20 vs. the normalized homogenized equivalent Young's moduli and shear moduli (E_{eq}/E_g and G_{eq}/G_g). Similar trends for equivalent Young's moduli and shear moduli are observed in Figure 4.6. Both E_{eq}/E_g and G_{eq}/G_g begin with the value of 1.0 when E_g is equal to E_m, and decrease rapidly at the beginning and then slowly with the increase of the modulus ratio E_g/E_m. It also can be seen that the in-plane modulus

E_{11} is greater than the out-of-plane moduli E_{22} and E_{33}, and In-plane shear modulus G_{23} is also less than the out-of plane shear moduli, G_{12} and G_{13}. These observations indicate that the unit cell has higher out-of-plane stiffness than its in-plane stiffness.

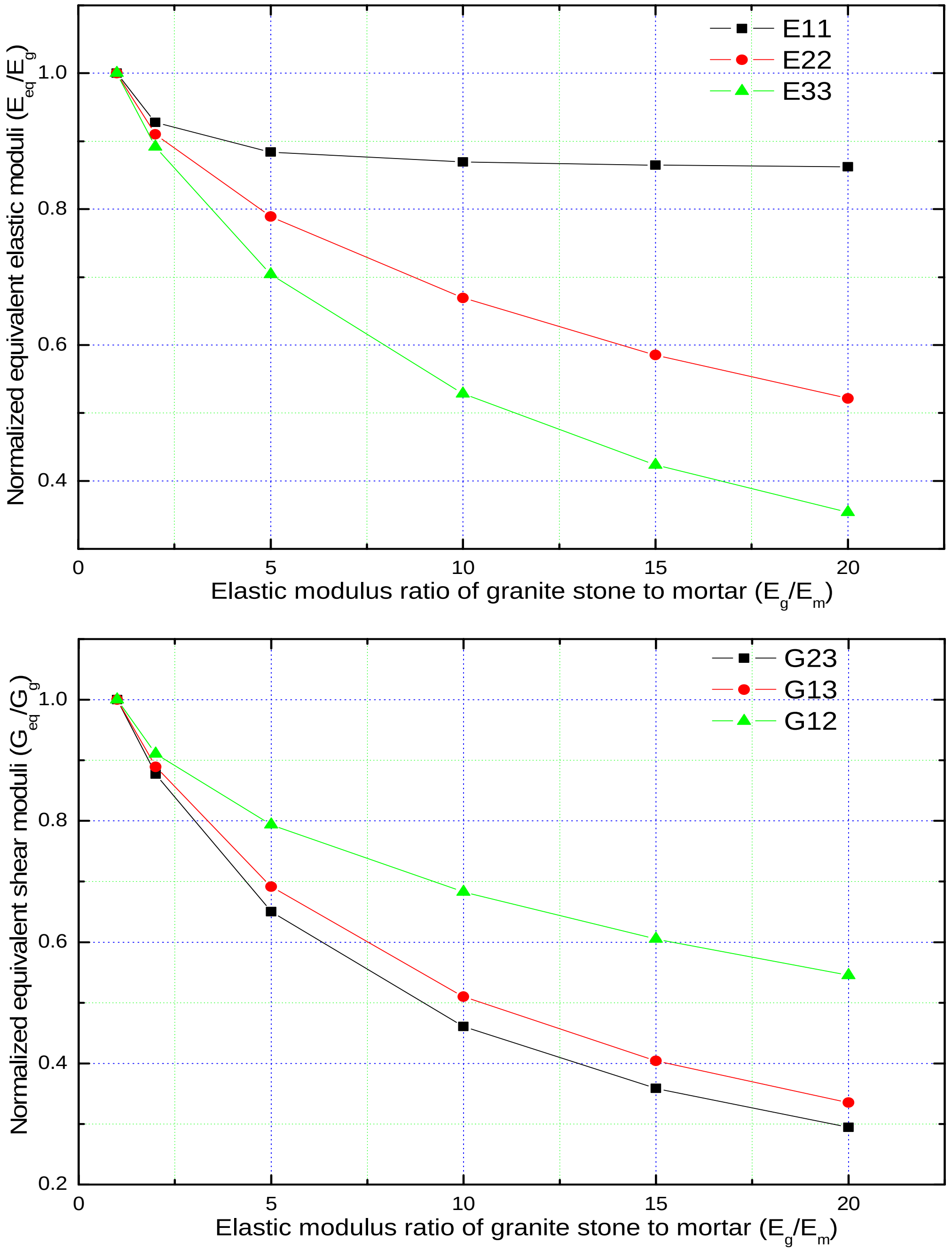

Figure 4.6: Effects of mortar moduli on the homogenized equivalent material properties

4.5.3 Effect of mortar volume fraction

To study the effect of mortar volume fraction on the homogenized equivalent material properties of the masonry structure, another two unit cells with mortar volume fraction of 28% and 40.5% are discretized into 40×40 subcells as shown in Figure 4.7.

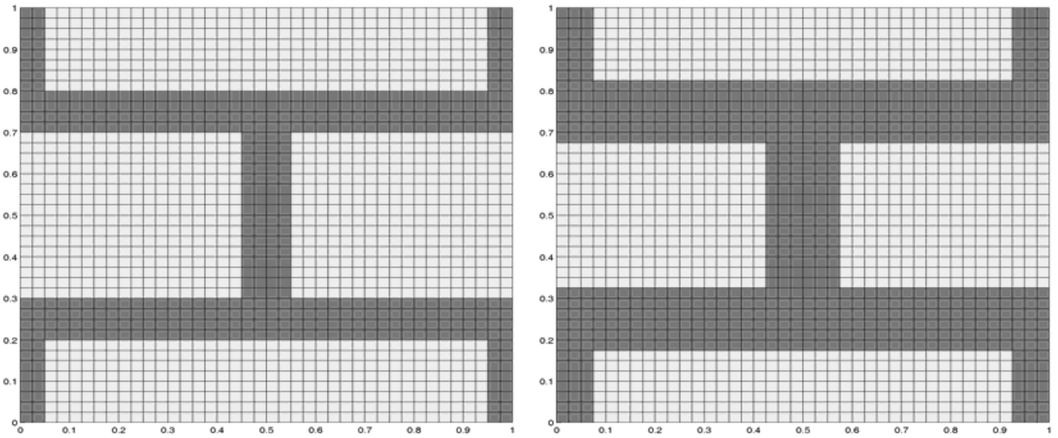

Figure 4.7: Masonry repeating unit cell with mortar volume fraction of (a) 28% and (b) 40.5%

Figure 4.8 shows the variation of normalized homogenized equivalent material moduli (E_g/E_m and G_{eq}/G_g) of the masonry as a function of the mortar volume fraction. It can be seen that the equivalent material moduli in every direction are sensitive to the mortar volume fraction and vary approximately inversely with respect to the increase of the volume fraction.

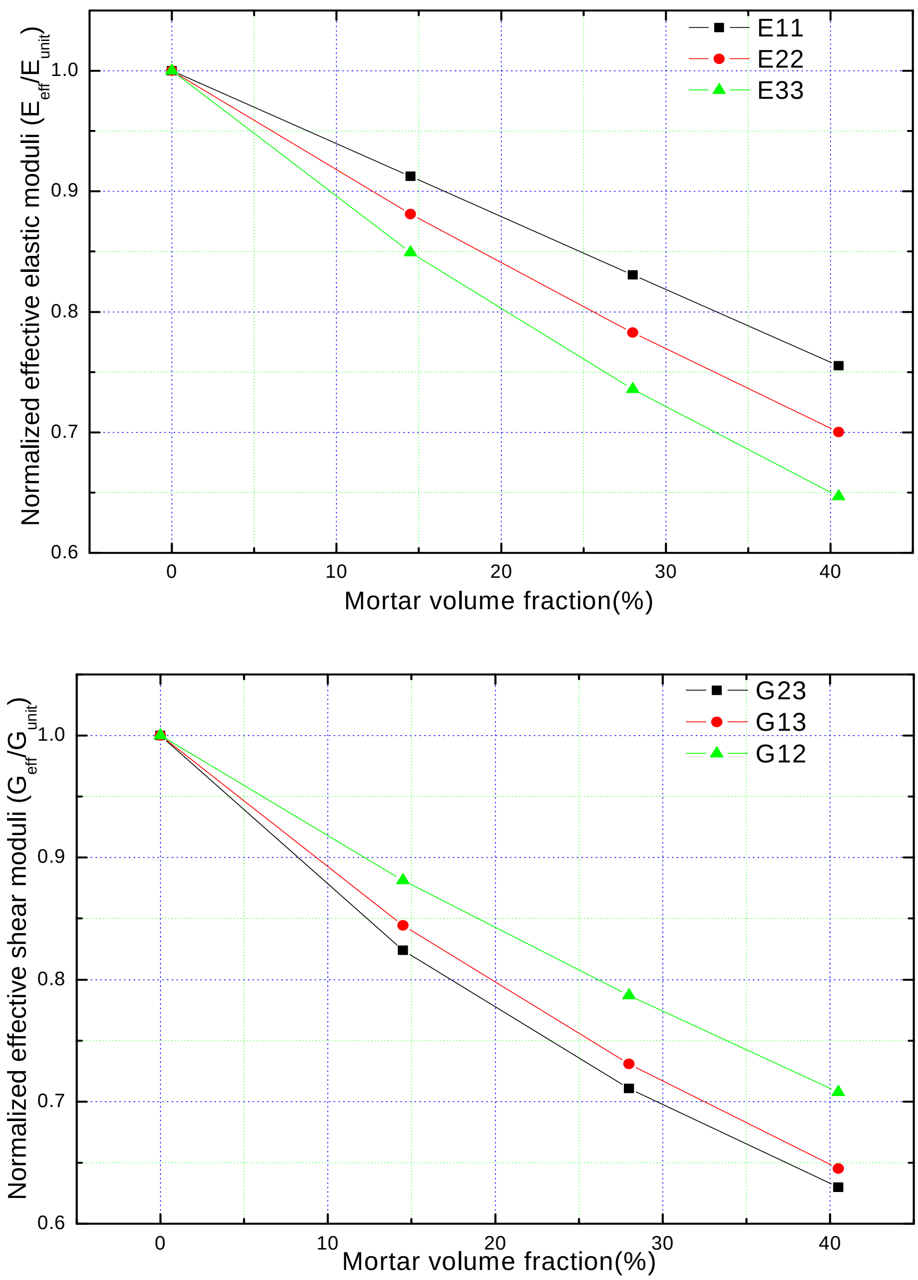

Figure 4.8: Normalized equivalent elastic constants with the variation of mortar volume fraction

4.5.4 Elasto-Plastic modeling and analysis

For the elasto-plastic modeling, the individual material properties for granite and mortar in the FVDAM masonry model was based on the compression tests as shown in Figures 3.6 and 3.8. The granite stone was assumed to be elastic during a uniform displacement loading applied to the model considering granite has a much higher compressive strength than mortar. The mechanical behavior of cement mortar was assumed to be elastic followed by a strain hardening, as observed in the experimental test (see Figure 3.8). It is noted that this elastic-plastic modeling is focused on the modeling of masonry structures before collapse since failure mode of masonry structures are characterized by brittle fracture of the granite unit and thus the fracture strain is hard to predicted, as observed in compression experiment tests (See Figure 3.11). Figure 4.10 show the macroscopic stress-strain comparison from the FVDAM model and the compression tests. In the FVDAM model, the material properties for granite stone and cement mortar are shown in Table 3.1 and 3.3, respectively. There are 3 samples for both granite stone and cement mortar in the compression test, so 9 different FVDAM models were obtained with different combined properties for granite stone and cement mortar. The red line in Figure 4.10 represents their average values and the scatters denote the variations at different strains. As seen in Figure 4.10, the macroscopic stress-strain response predicted by the FVDAM indicate masonry structures exhibit an obvious bilinear strain hardening behavior, which correlates well with the experimental results. This observation also confirms the accuracy and effectiveness of the FVDAM model in predicting the elasto-plastic behavior of the masonry structure if the individual mechanical behavior of its constituents (i.e., unit and mortar) is known.

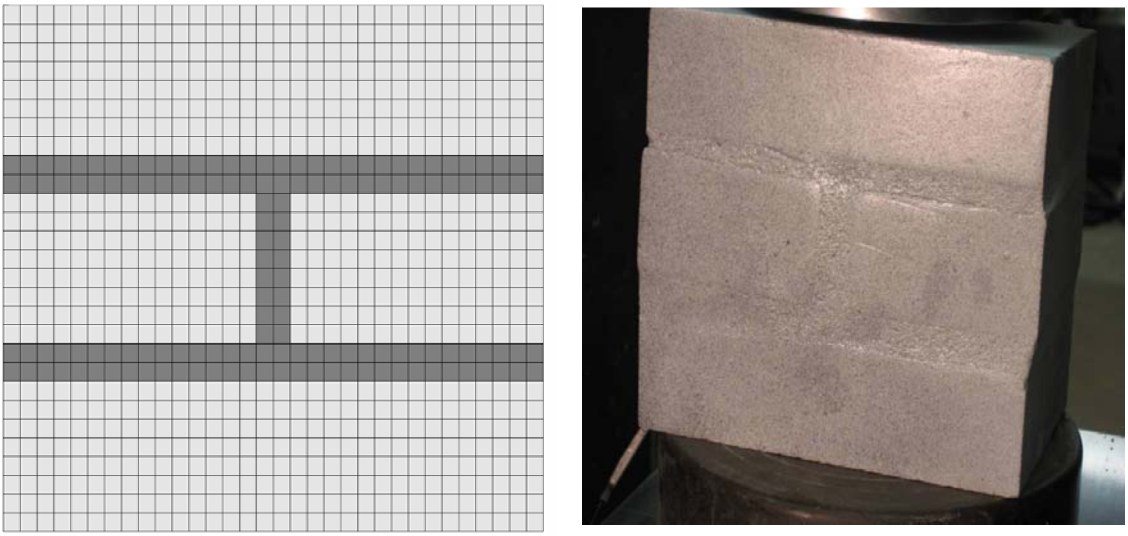

Figure 4.9: The tested masonry specimen (right) and the FVDAM model (left)

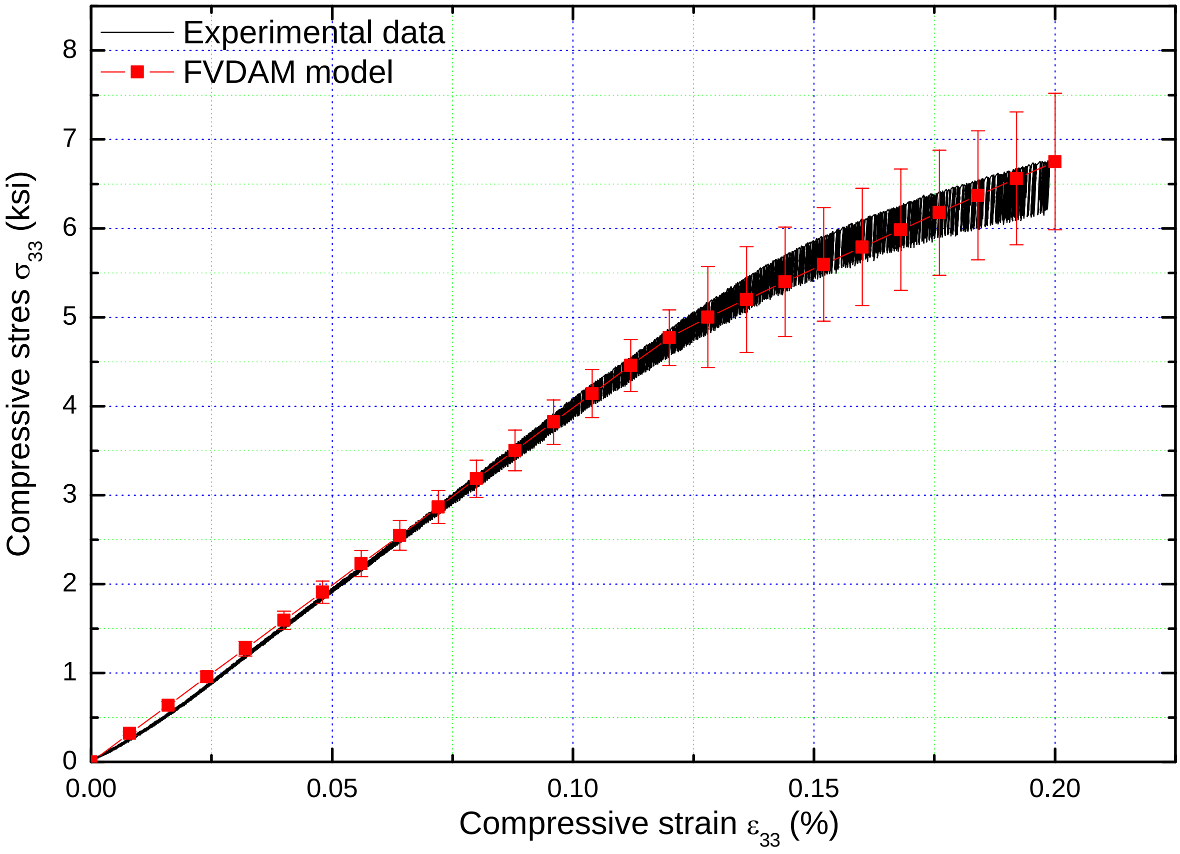

Figure 4.10: Macroscopic elasto-plastic stress-strain responses of the masonry obtained from FVDAM model and compression test

Figure 4.11 gives the initiation and evolution of effective plastic strain distributions during plastic loading from the FVDAM model. Clearly, the granite units don't exhibit any plastic region since granite stone is still in the elastic region, while extensive plastic regions are shown in the mortar zones. With the increase of displacement loading, the intensity of effective plastic strain increases in the mortar layers, which agree well with the observation from the masonry compression test as shown in Figure 3.12 and 3.13. As seen in Figure 3.13, the average vertical strain εyy in the mortar layers has a much more increase compared with the granite layers as loading continuously applied. Local strain variation in the granite and mortar layers observed in the DIC images are due to the inhomogeneous properties of granite and cement mortar, which is different from the assumption of homogenous properties for both granite and mortar in the FVDAM model.

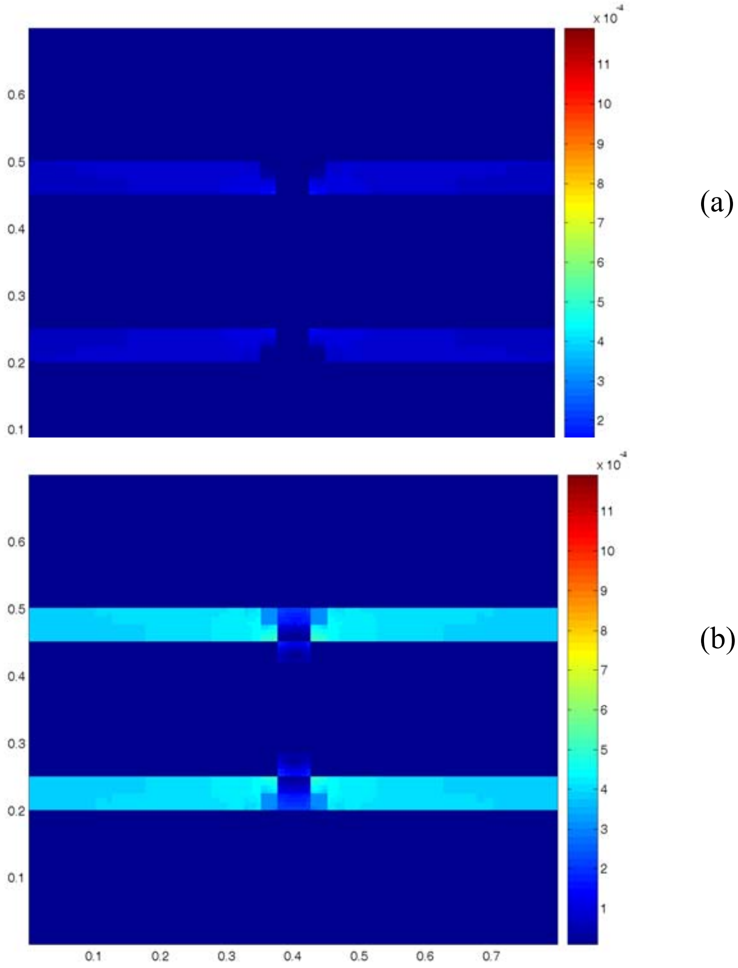

Figure 4.11: Evolution of effective plastic strain distributions in the masonry structure: (a) Initiation of yielding of mortar and (b) subsequent hardening of mortar

4.6. Conclusion

In this study, the micromechanics-based FVDAM model has been modified and enhanced for the mechanical analysis of multiphase material containing elasto-plastic phases. The accuracy and efficiency of the FVDAM model predicting mechanical behavior of multiphase composite material was validated by comparing with FEM results from the commercial software FEMLAB. The results indicate that the FVDAM model is capable of predicting both macroscopic and microscopic response accurately.

The FVDAM model was also applied to masonry structure composed of granite stone and cement mortar at the first time. The extensive parametric analysis was made to understand the effect of the mesh size, cell texture, mortar elastic modulus and mortar volume fraction on the homogenized/effective elastic properties. It was found that mesh size and texture of the repeating unit cell has no much influence on the effective elastic properties of the composites. However, the mortar elastic modulus and the mortar volume fraction will affect the overall effective stiffness of the masonry composite significantly. It was also observed that the mortar elastic modulus has much more effect on the averaged in-plane stiffness than on the out-of-plane stiffness. The overall effective stiffness of the masonry composite is approximately inversely to the mortar volume fraction.

Finally, elasto-plastic analyses were carried out on the granite masonry structure to compare with the experimental results. It was observed that the macroscopic stress-strain response predicted by the FVDAM correlates well with the experimental results. The experimental-analytical correlation also demonstrates the FVDAM model has a good capability in predicting the response of masonry structure if the individual mechanical behavior of its constituents (i.e., granite unit and cement mortar) is known. The initiation and evolution of effective plastic strain distributions was also obtained during vertical compressive plastic loading using the FVDAM model. It was found that plastic zone initiates and propagates through mortar layers and finally the masonry structure fails until mortar failure.

Chapter 5: Macro-modeling of Masonry Structure for Seismic Assessment

5.1 Overview

In the last chapter, a micro-modeling analysis of a masonry panel was modeled by the FVDAM model. However, the use of micro-models becomes unlikely to use for the global analysis of entire buildings or bridges due to the expensive computational cost. In addition, the actual distribution of blocks and joints might be impossible to detect unless many investigations are performed. To overcome this computational difficulty, a macro-modeling approach has to be used to model large-scale masonry structure. The macro-models don't make distinction between blocks and mortar joints and smear the effect of joint presence through the formulation of the constitutive modeling of the equivalent material. The equivalent continuous material was obtained by the micro-modeling in the last chapter.

In this study, the unreinforced masonry tower of the Brooklyn Bridge was macro modeled as a homogeneous material and its seismic behavior was investigated using the Finite Element software ABAQUS. The masonry structure was modeled by the Mohr-Coulomb failure criterion, where the conventional isotropic elastic properties were replaced by the orthotropic elastic properties of masonry structure obtained by the FVDAM model. Modal analysis and the nonlinear time-history analysis were performed on the masonry tower with the seismic ground motions represented by three different historical earthquake records. It was found that the whole tower still retains the global structural stability and some local damages appear in the arch-base connection regions.

The tower drift under the design seismic excitation was also determined to compare with the requirement of the code for seismic performance design objective. It was found that the deformation of the masonry tower is acceptable when it is subjected to the design seismic excitation. Finally, the structural improvement was recommended based on the simulation outcome.

5.2 Introduction

Over the past decade, seismic evaluations of bridges in the northeastern United States have received significant attention. Although the seismic hazard in the eastern United States is significantly lower than that in the west coast, many historic bridges in the east are nevertheless vulnerable to earthquake damage. Taking the lessons from many past major earthquake events such as Northridge earthquake in 1994, New York City Department of Transportation (NYCDOT) initiated the seismic retrofit program for the high-risk bridges to assure that important transportation structures maintain their function after an earthquake. Seismic retrofit of bridges in NYC is also part of the inspection and rehabilitation program mandated by Congress and administrated by FHWA through local authorities. According to the Seismic Design Criteria Guideline (NYCDOT 1998) established by the NYCDOT, the Brooklyn Bridge is classified as a critical bridge and the seismic performance need to be assessed carefully. The Brooklyn Bridge was built to connect the island of Manhattan to Brooklyn in 1883 and remains one of the most important icons of civil engineering in America until now. Its main span has almost 1,600 feet long and was the longest suspension bridge in the world at the time of its completion. The most prominent features of the bridge are the unreinforced masonry towers with a height of 270 feet (see Figure 5.1).

Figure 5.1: Unreinforced masonry tower of the Brooklyn Bridge as its most prominent features

The numerical modeling and analysis of masonry structures represents a very complex problem because of the constitutive nature of masonry. Being composed of two very different materials, i.e. the units (bricks, blocks and etc.) and the mortar joints, masonry structures exhibit a heterogeneous behavior. Based on these considerations, researchers (Saadeghvaziri and Metha 1993; LourencI o 1996) have divided models for masonry into two categories: micro and macro. In micro models, masonry units and mortar are explicitly modeled, whereas in the macro model, masonry is modeled as a single material using average properties of masonry. One modeling strategy cannot be preferred over the other because different application fields exist for micro- and macro-models. Micro-modeling is useful to give a better understanding about the local behavior of masonry structures. However, macro-modeling is more practicable for large-scale masonry structure due to the reduced time and memory requirements as well as a user-friendly mesh generation. As macro modelling of masonry is advantageous when the global behaviour of the structure is of prime importance, in this research project macro modelling has been adopted.

To model masonry as a composite, sound numerical implementations of plasticity models, will be required. Mohr-Coulomb model was used frequently for analyzing numerically the geotechnical problem as described in the Chapter 2 (Desai and Siriwardane 1984; Chen and Saleeb 1994). Considering the capability of predicting the mechanical behaviour of the geotechnical material the Mohr-Coulomb failure criterion will be used in the analysis of masonry structure. In the Mohr-Coulomb material, isotropic idealization is assumed generally; however the constitutive behavior of masonry exhibits anisotropy due to the geometrical arrangement of units and mortar, even if the properties of these constituents are isotropic. Therefore, an orthotropic Mohr-Coulomb model was used to simulate the masonry material in the commercially FEM software ABAQUS. Its orthotropic elastic properties for the masonry structure were obtained by a micro-modeling using the micro-mechanics based FVDAM model (Zeng and Lin 2008).

5.4 Seismic analysis and design criteria in New York City regions

In recent years, there has been a strong shift in seismic design and retrofit philosophy towards so-called performance-based seismic design (Fajfar and Krawinkler 2004). Under such a design philosophy, the primary objective is to design/retrofit structures such that they have predictable level of damage when subjected to different ground motion intensities. A two-level design is usually adopted for critical bridges in New York City as follows:

Functional Evaluation Earthquake (FEE) - A functional evaluation earthquake is defined as one, which has a relatively high probability of occurrence during the lifetime of a structure. The structure should be proportioned to resist the intensity of ground motion produced by this event without significant damage to the basic system, thus allowing it to remain functional immediately following the FEE event.

Safety Evaluation Earthquake (SEE) - A safety evaluation earthquake is defined as the most severe event which can reasonably be expected to ever occur at the site. Because this earthquake has a very low probability of occurrence during the life of a structure, significant structural damage is permitted; however, collapse and serious personal injury or loss of life should be avoided.

To represent the FEE and SEE events, different hazard response spectra have to be selected as specified by NYCOT as follows:

- A 10% probability of exceedance in 50 years (corresponding to an approximated return period of 500 years) ;
- A 2% probability of exceedance in 50 years (approximate 2500 years return period).

Figure 5.2 and 5.3 show ground motion time history curves and the corresponding response spectra in the New York City region, representing a mean return period of 500 and 2500 years, respectively. The rock motions were generated from the AASHTO Spectrum and modified by the NYCDOT to adopt uniformly for the New York City region. These spectra were established using a probabilistic seismic hazard analysis in which the likelihood of seismic events occurring in the region around New York City.

The Seismic Design Criteria for bridges in New York City was based on different levels of performance goals. The required seismic performance of a bridge is to be determined according to its importance category. Following the 1994 AASHTO-LRFD Section 3.10.3, New York City bridges are classified as *Critical*, *Essential* and *Other*. *Critical* bridges are defined as those that must remain open to all traffic after the design earthquake (10% in 50 years probability of exceedance) and be usable by emergency vehicles and for security/defense purposes immediately after a large earthquake, defined as an event having a 2% probability of being exceeded in 50 years. A *Critical* Bridge must provide immediate access after the lower level (functional) event and limited access after the upper level (safety) event and continue to function as a part of the lifeline, social/survival network and serve as an important link for civil defense, police, fire department and/or public health agencies to respond to a disaster situation after the event, providing a continuous route.

Critical structures shall be analyzed for two earthquake levels: a lower (functional) event having 10% probability of being exceeded in 50 years (500 year return period); and an upper (safety) event having a 2% in 50 years probability of exceedance (2500 year return period). *Critical* bridges shall survive the upper level event with *repairable* damage. After the 10% probability of exceedance in 50 years event, the bridge shall suffer *no* damage to primary structural elements and *minimal* damage to other components. According to NYC Seismic Design Criteria Guideline, the Brooklyn Bridge is classified as a critical bridge and thus two earthquake levels will be analyzed in this study.

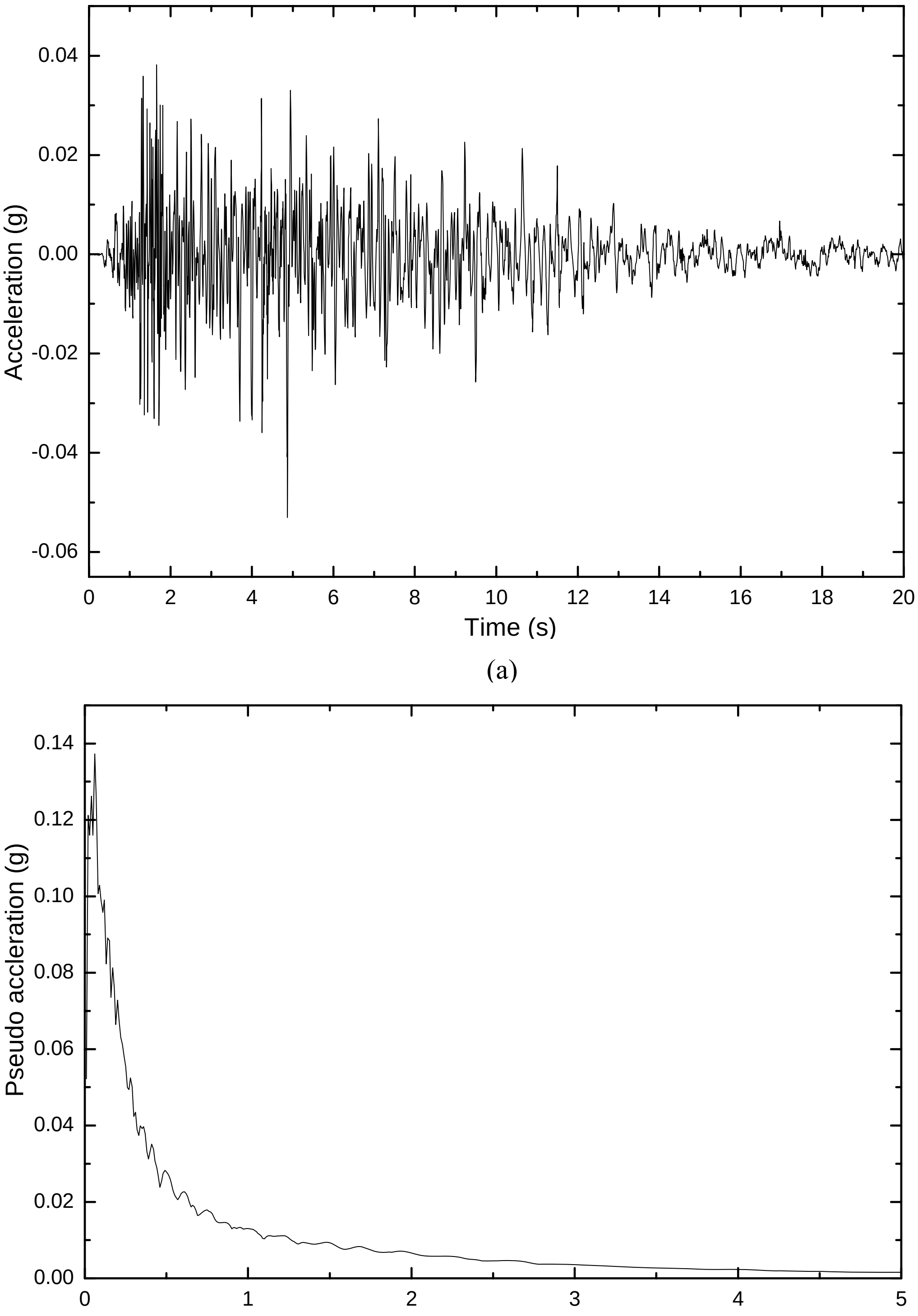

(a)

(b)

Figure 5.2 NYC – ground motion acceleration history curve (a) and response spectra (b) - 5% damping 500-year return period = 10% in 50 years probability of exceedance

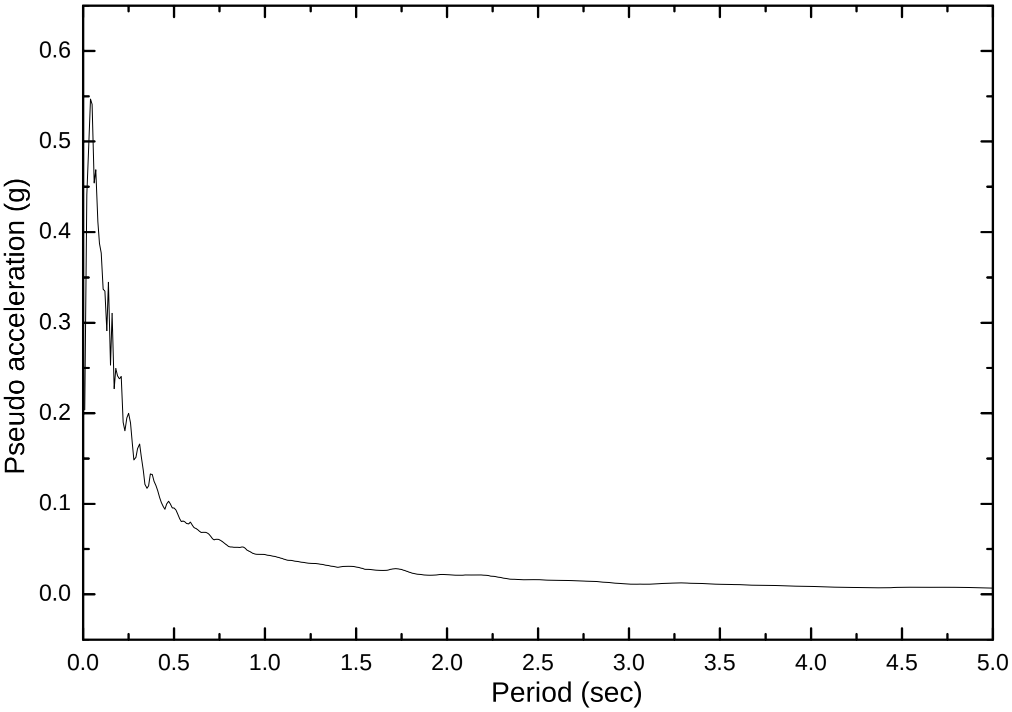

(a)

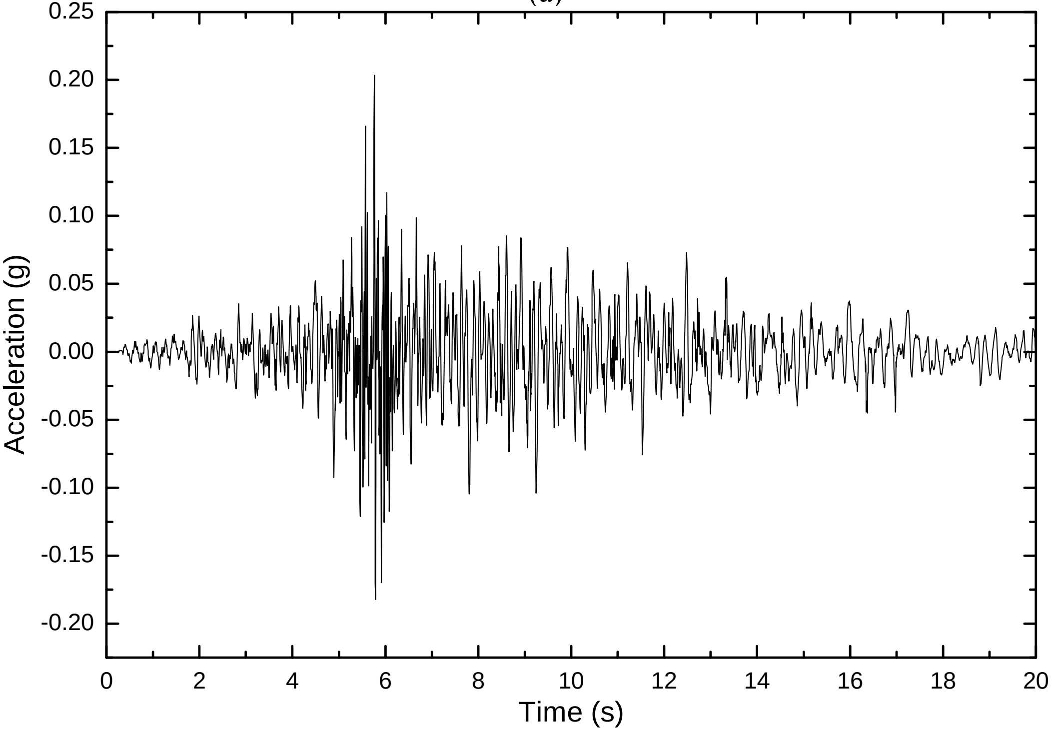

(b)

Figure 5.3: NYC – ground motion acceleration history curve and acceleration response spectra - 5% damping 2500-year return period = 2% in 50 years probability of exceedance

5.5 Nonlinear solution technique for seismic analysis

Seismic response analysis of structures can be evaluated by a number of analysis methods. At present the response spectrum analysis and time-history analysis are two types of usual methods in seismic response analysis. For response spectrum analysis, the peak response is estimated by the application of modal combination rules such as the Square Root of the Sum of the Squares (SRSS) method and the Complete Quadratic Combination (CQC) method (Chopra 2001). Since the peak response in each mode does not occur at the same time, response spectrum analysis reflects an approximation method in estimates of peak response. In contrast, for time-history analysis, the peak response can be obtained directly from the absolute maximum value on a response-history plot. The response-history is normally determined using step-by-step numerical integration of the equation of motion. Consequently, time history analysis is performed using computer software where the ground acceleration is divided into small time steps. The response is calculated at the end of each time step while satisfying dynamic equilibrium. Since the time-history analysis provides a method for obtaining the exact response of a structure as a function of time, the time-history analysis was performed on the masonry tower of the Brooklyn Bridge when subjected to different earthquake records in both the longitudinal and transverse directions. Also, the performance acceptance criteria proposed by FEMA-273 (FEMA 1997) will be implemented to evaluate the performance levels such as target displacements.

The time history analysis is based on the explicit Formulation. The explicit method of structural analysis is essentially suitable for high frequency dynamic events such as earthquake and impact. It is computationally efficient for the analysis of large models with relatively short dynamic response times. This method allows numerical solutions without the formulation of structural stiffness matrices. An explicit central difference time integration rule and diagonal element mass matrices are used in the analysis process. The explicit central difference time integration rule is used to satisfy dynamic equilibrium equations and requires nodal mass to exist at all degrees of freedom.

Dynamic equilibrium is solved at the beginning of the increment as:

$$M \cdot a = P - I \tag{5.1}$$

where 'M' is the nodal mass matrix, 'a' is the nodal acceleration, 'P' is the external applied force, and 'I' is the internal element forces. The accelerations at the beginning of the current increment (at time t) are calculated by the following equation:

$$a_{(t)} = \left(M\right)^{-1} \cdot \left(P - I\right)_{(t)} \tag{5.2}$$

The accelerations of any node are determined completely by its mass and the net force acting on it, making the nodal calculations very simple and inexpensive. The accelerations are integrated through time using the central difference rule, which calculates the change in velocity assuming that the acceleration is constant. This change in velocity is added to the velocity from the middle of the previous increment to determine the velocities at the middle of the current increment by the following relation:

$$V_{\left(t+\frac{\Delta t}{2}\right)} = V_{\left(t-\frac{\Delta t}{2}\right)} + \frac{\Delta t_{(t+\Delta t)} + \Delta t_{(t)}}{2} a_{(t)} \tag{5.3}$$

The velocities are integrated through time and added to the displacement at the beginning of the increment to determine the displacement at the end of the increment as follows:

$$d_{(t+\Delta t)} = d_{(t)} + \frac{\Delta t_{(t+\Delta t)} + \Delta t_{(t)}}{2} V_{\left(t+\frac{\Delta t}{2}\right)} \tag{5.4}$$

The term explicit refers to the fact that the state at the end of the increment is based on the displacement, velocities and accelerations at the beginning of the increment. For the method to produce accurate results, the time increments must be quite small so that the accelerations are nearly constant during an increment. Once displacements are calculated from Equation (5.4), the strains are calculated and in turn element stresses are calculated by applying material constitutive relationships from Equation (5.5):

$$\sigma_{(t+\Delta t)} = f\left(\sigma_{(t)}, d\varepsilon\right) \tag{5.5}$$

5.5. Analytical Procedure

5.5.1 Finite element model

In this study, a detail local finite element model is constructed on the masonry tower as a standalone structure since the towers are the critical components for a suspension bridge and the modeling of a tower is able to capture the important nonlinear response of the bridge. The 8-node brick (C3D8) and 6-node prism (C3D6) element types (ABAQUS 2002) are adapted to mesh the tower. An equivalent lumped mass element was used to represent the tributary mass of the superstructure (bridge deck and girders). The elevation of the masonry tower and the developed finite element meshed tower model are shown in Figure 5.4.

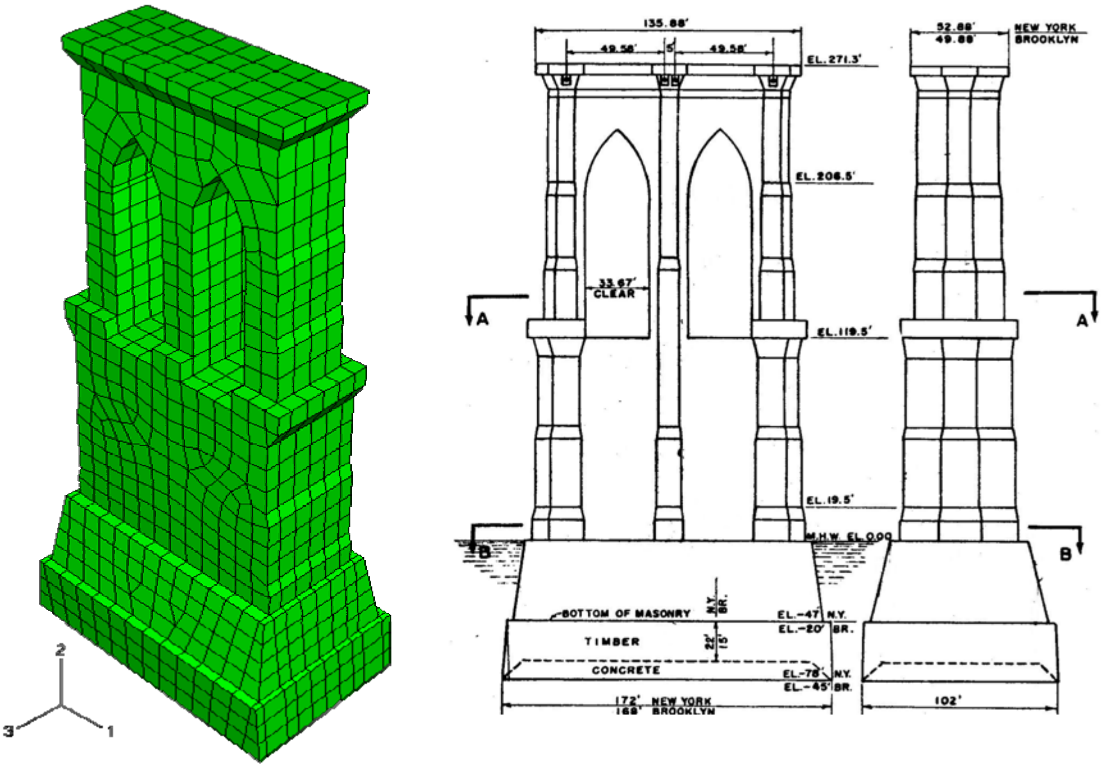

Figure 5.4: The elevation of the masonry tower (right) and the finite element model (left)

5.5.2 Equivalent Material properties

The orthotropic elastic properties of masonry structure were obtained by a micro-modeling using the FVDAM model as described in the last chapter. The plastic parameters such as friction angel ϕ, cohesion strength c and hardening parameter H' are required in the Mohr-Coulomb model. These parameters are related to uniaxial compressive yielding strength f_c' and tensile yielding strength f_t' as shown in Equations 4.6-4.8. The uniaxial compressive yielding strength f_c' was obtained to be 3.2 ksi in the

FVDAM micro-modeling of masonry structure, as shown in Figure 4.14. To obtain the uniaxial tensile yielding strength for the masonry composite, uniaxial tensile strain is applied to the same micro model (see Figure 4.13) and average tensile stress and strain curve for the masonry model are shown in Figure 5.5. The tensile yielding stress for the masonry composite is determined to be 0.28 ksi from the FVDAM model. Once the average compressive yielding strength f_c' and tensile yielding strength f_t' for the small masonry panel are determined, the equivalent material properties for masonry structure can be determined, as listed in Table 5.1.

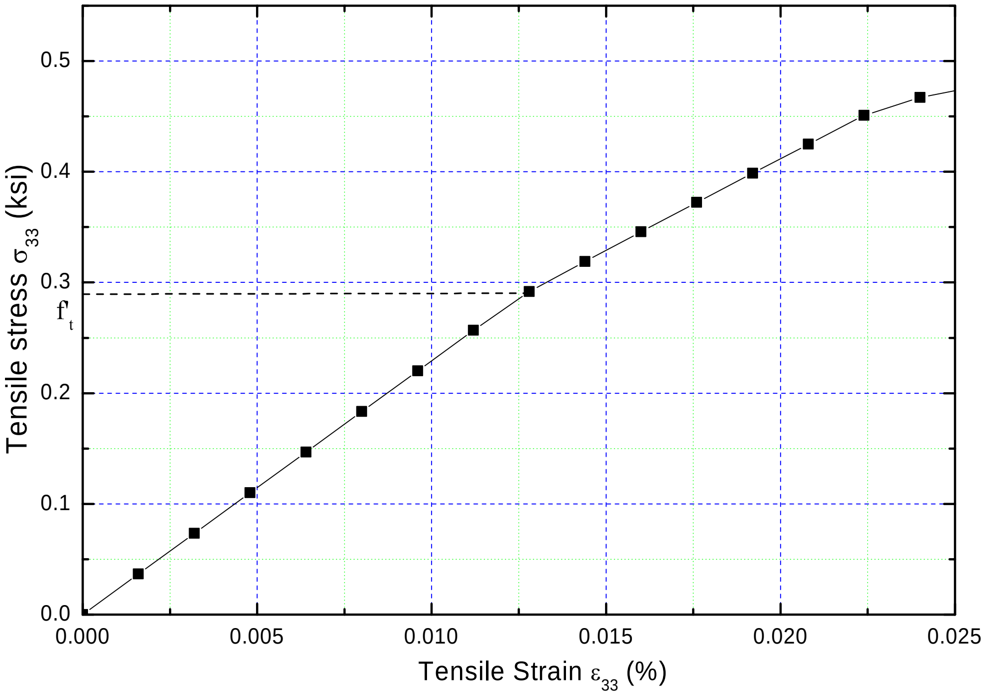

Figure 5.5: Macroscopic tensile stress strain curve of the masonry obtained from FVDAM model

Table 5.1: Equivalent Material properties for masonry structure

E_{11}	E_{22}	E_{33}	G_{23}	G_{13}	G_{12}	ν_{23}	ν_{13}	ν_{12}	C	ϕ	H′
5111	4937	4757	1925	1971	2059	0.2	0.2	0.2	0. 47	56.1^{o}	112

Units: ksi for all the moduli and cohesion strength in the above table.

5.5.3 Modal analysis and loading steps

Before apply loading steps, a modal analysis was performed on the masonry tower resulting in the longitudinal and transverse natural period. The modal analysis performs Eigen value extraction to calculate the natural frequencies and the corresponding mode shapes of a dynamic system. The Lanczos methods are used to determine the Eigen values to extract the natural frequencies of the system. Details of the Lanczos solver can be found in the ABAQUS Theory Manual(Hibbitt and Sorensen 2002). The Eigen value problem for the natural frequencies of an undamped finite element model is given by

$$-\omega^2\left[M^{mn}\right]+\left[K^{mn}\right]=\{\varsigma\} \tag{5.6}$$

where 'M' is a symmetric, positive definite mass matrix, 'K^{mn}' is a stiffness matrix, 'ς ' is the Eigen vector or the mode of vibration, 'ω' is frequency, 'm' and 'n' are degrees of freedom of the system. Once the natural frequency of the system for the lowest mode is determined, the time period of the system is calculated for the static analysis of the system simply by inverting the frequency.

Then the static loading with a combination of gravity loading and hydrostatic pressure was applied on the masonry tower prior to the seismic analysis. In the ABAQUS analysis, these loads are specified in two consecutive static steps. For the subsequent seismic dynamic analysis, all nodes at the base were subjected to the longitudinal and transverse components of the ground accelerations from the three different historical earthquake records.

5.5.4 Seismic loading

For comparison purpose, two different approaches for seismic loading are used. For the first approach, the artificial ground motion history curves for both 500-year event and 2500-years are used for seismic input, as shown in Figures 5.2 and 5.3. For the second approach, the actual ground motion history curves from previous earthquake records are used for seismic input, which is explained in detail in the following.

Three earthquake records were selected in this study since this represents the minimum number of records recommended by current seismic design codes for time history analysis (FEMA 1997). The three earthquake records selected were obtained from strong motion database collected by PPERC (Pacific Earthquake Engineering Research Center). The detail records are as follows: the I-ELC180 component of the El Centro record of the 1940 Imperial Valley, the MU2035 component of the 1994 North Ridge and the CHY006-E component of 1999 Chichi, Taiwan. The reason for selecting these three records was as follows: the El Centro record was selected since the spectral characteristics of this record are known to closely match the design spectral shapes adopted in the design code (Chandler and Mendis 2000); the Chichi, Taiwan record was selected since it was one of the recent major earthquake event and corresponds to a relatively strong earthquake. The Northridge earthquake record was selected since the earthquake caused the partial or complete collapse of five bridges while damaging approximately 200 others (Hall 1995). The ground acceleration records and associated pseudo-acceleration response spectra for each earthquake are plotted to the same scale, as shown in Figure 5.7. It is noted that the published response spectrum by AASHTO (AASHTO 1998) is also included in Figure 5.6. The selected characteristics of the records are shown in Table 5.2. As is evident from Figure 5.6 and Table 5.2, the characteristics of these records have common characteristics such as high amplitude and long duration. The selected three records are scaled to the peak acceleration of design spectrum (0.4g) in New York City region for seismic input (see Figure 5.7). The damping in the tower was characterized by an assumed 5% modal damping for each mode of vibration

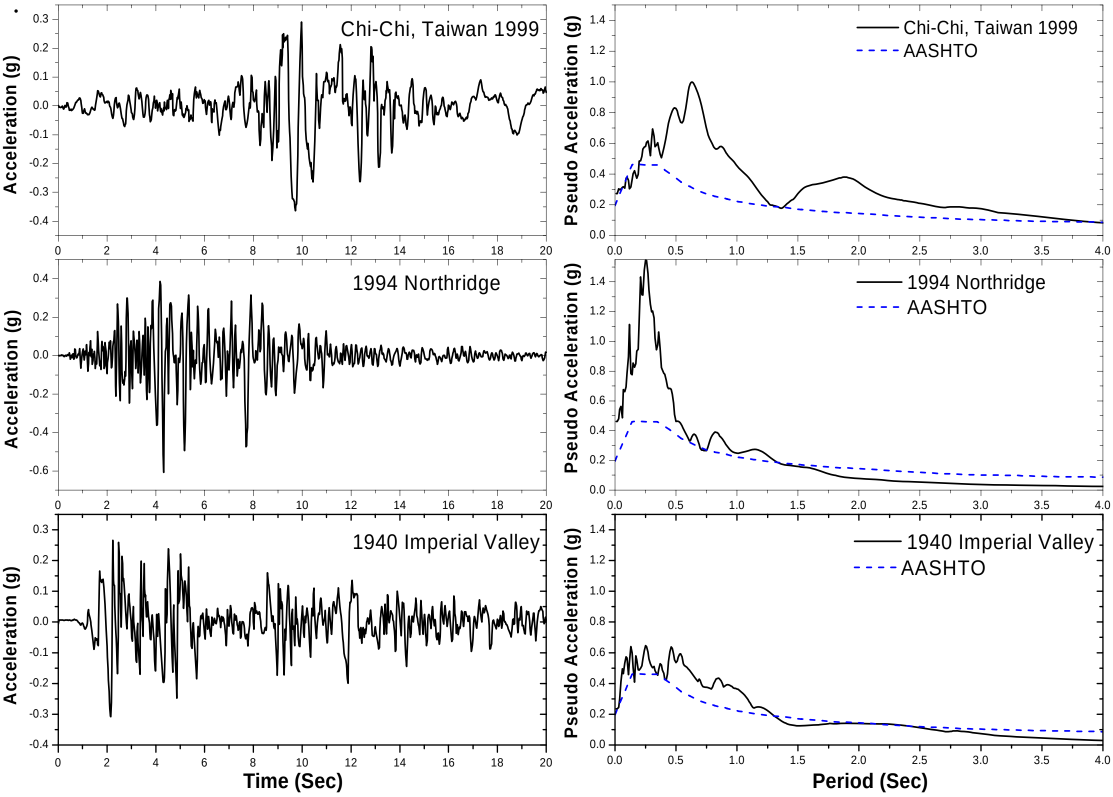

Figure 5.6: Earthquake ground acceleration records used for seismic analysis and associated 5%-damped pseudo-acceleration response spectrums

Table 5.2: Characteristics of earthquake ground motions used in seismic analysis

Earthquake	Component	Magnitude	Epicentral Distance (km)	PGA(g)
1940 Imperial Valley	I-ELC180	7.0	8.3	0.313
1994 Northridge	MU2035	6.7	20.8	0.617
Chi-Chi, Taiwan 1999	CHY006-E	7.6	14.9	0.364

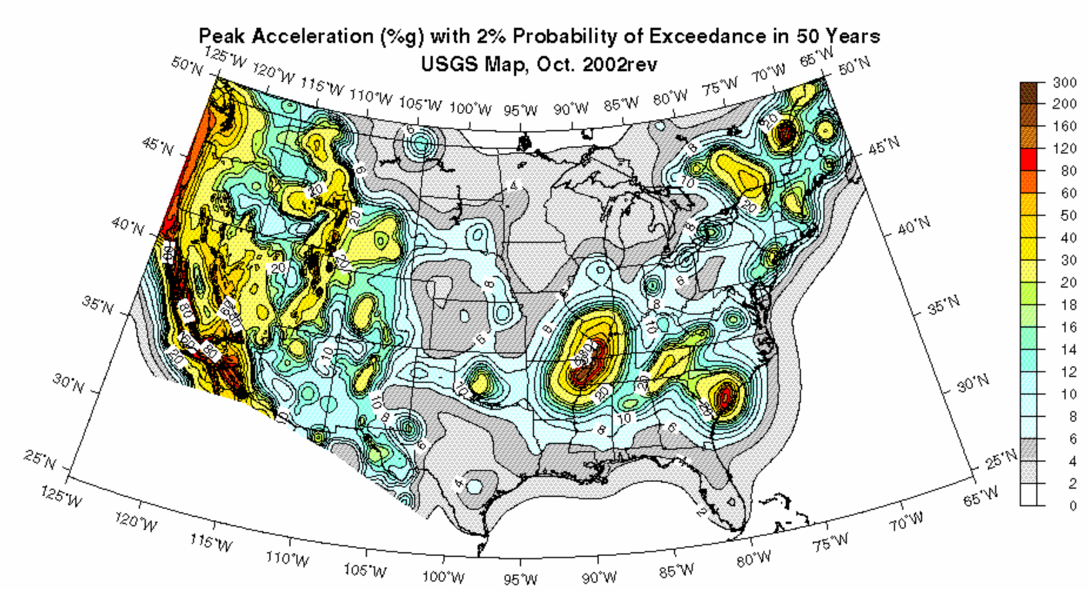

Figure 5.7: Peak acceleration %g) with 2% probability of exceedance in 50 years USGS map.

In ABAQUS, initial time increment, time period of the step, minimum time increment and maximum time increment control the solution for dynamic analysis of structures. The program was also allowed to control the solution automatically adjusting the increments suitably for achieving converged solutions within a minimum period. ABAQUS provides two types of output data, namely field output and history output. In the field output components of stresses and strains for the whole model are extracted, whereas in the history output selected components (stresses, strains and displacements etc.) are extracted during the course of the analysis for specified nodes or elements in the critical regions. For understanding of the stress distribution and potential failure mechanisms of the masonry tower, components of stresses and strains for elements, reactions force and node displacement were extracted for post processing. Results obtained from post processing of the extracted data are presented and discussed in the following section.

5.6 Results and Discussion

5.6.1 Modal analysis result

Prior to the seismic analysis, a modal analysis was performed on the masonry tower resulting in the different natural periods and vibration mode shapes shown in Table 5.3. Only the first six vibration mode shapes are shown in Figure 5.8 since first modes play the controlling role in the analysis of the structural dynamic behaviors. As observed in the Figure 5.8, the first, second, and third modes represent the longitudinal bending, i.e. along bridge span direction (3 direction), transverse bending (1 direction), and twisting of the tower, respectively. The higher modal shapes, respectively, represent the second longitudinal, transverse and torsion mode of the tower.

The formula shown below (FEMA 1997) is used to estimate the allowable target displacement of the top node of the tower:

$$\delta_t = C_0 C_1 C_2 C_3 S_a T_e^2 / (4\pi^2) \tag{5.7}$$

where C_0, C_1, C_2, and C_3 are modification factors to explain modal participation factor, inelastic, hysteresis and P-Δ effects to affect the control node displacement, S_a is response spectrum acceleration and T_e is the effective fundamental period from modal analysis. For more details about the definition of each of the previous parameters and how to estimate it, see FEMA-273 (FEMA 1997). Once various modification factors are determined for the bridge tower, the allowable drift limit was calculated to be 5.4″ .

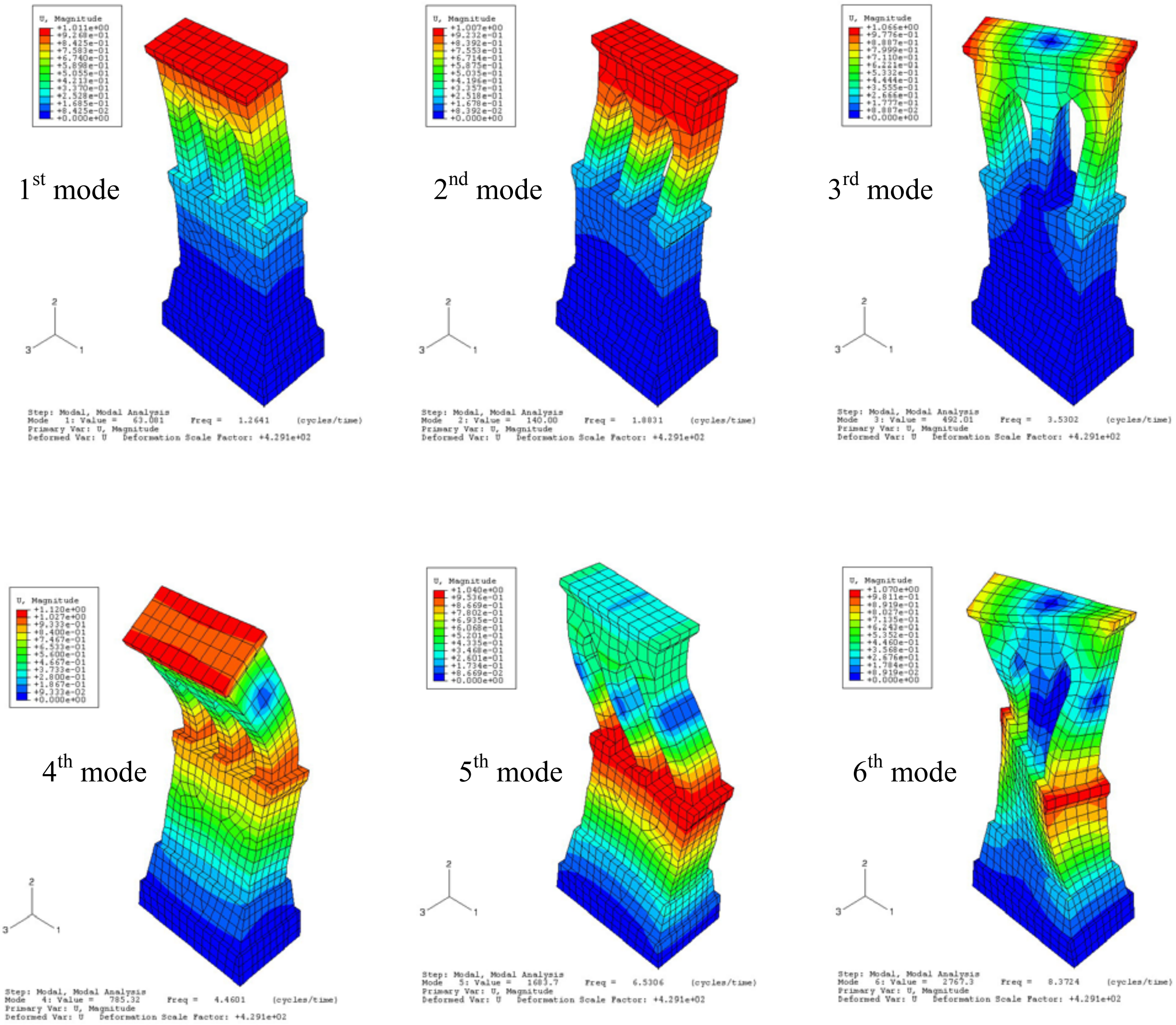

Figure 5.8: The first six mode shapes of the masonry tower

Table 5.3: Natural periods and vibration mode shapes of the tower

Mode Number	Natural periods (Sec)	Mode shape
1	0.791	Longitudinal bending
2	0.531	Transverse bending
3	0.283	Torsion
4	0.224	Longitudinal bending
5	0.153	Transverse bending
6	0.120	Torsion

5.6.2 Seismic analysis results

5.6.2.1 Ground motions excitation from NYCDOT design code

Figures 5.9-5.12 show the longitudinal and transverse displacements at the base node and the top nodes of the masonry tower for the 500-year and 2500-year earthquake input case. The displacement of the base node corresponds to the seismic motion imposed. At the same time, the drift of the top node, which is the displacement difference between the base node and top node, are plotted in the same figure. The maximum drift of the top node in the tower for the longitudinal and transverse direction for three seismic input cases are tabulated in Table 5.4. As seen in Table 5.4, the drift in the longitudinal direction is greater than the transverse direction. This result is consistent with the observation in the modal analysis (see Figure 5.8), where the longitudinal bending controls over the transverse bending. The maximum drift for the top node of the tower for the 2500-year earthquake event is 2.8″ , which is less than the allowable target displacement 5.4″ as shown in the above modal analysis. The maximum drift ratio, defined as the tower drift to height of the tower, is about 0.3%, which is less than the allowed drift ratio (1%) prescribed by FEMA 356 structural performance level (life safety) (FEMA 2000). These observations indicate that the deformation of the masonry tower is acceptable when it is subjected to a design seismic excitation.

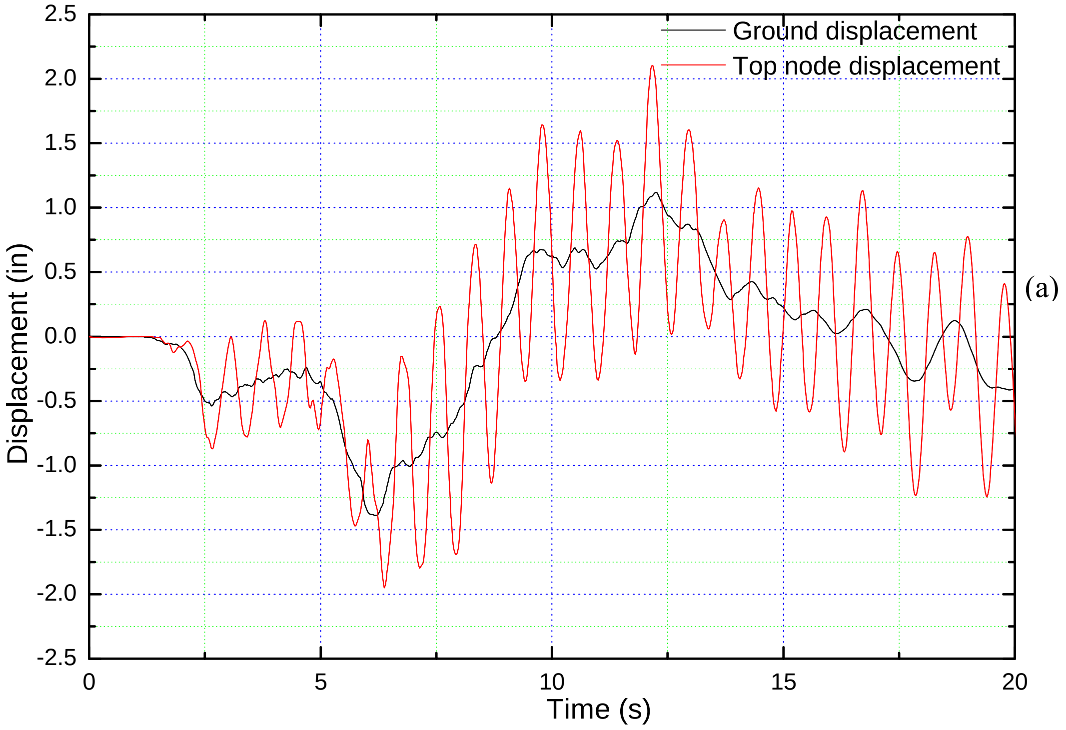

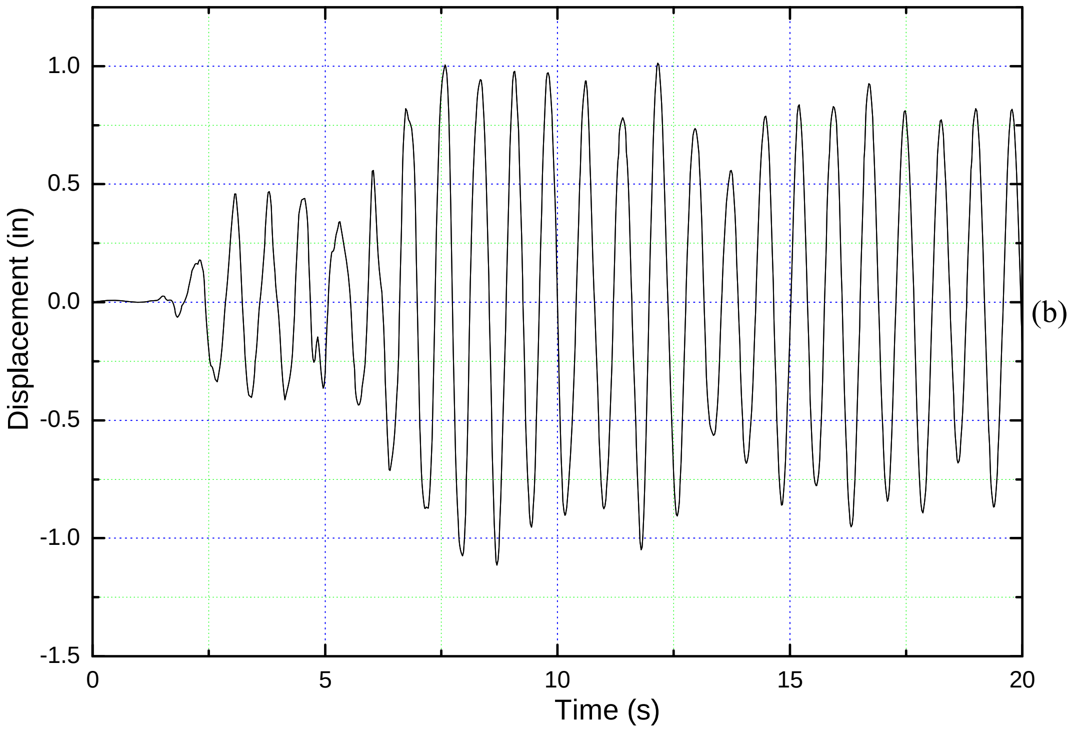

Figure 5.9: (a) Displacement history in the base and top node and (b) drift history of the top node in the longitudinal direction for 500-year earthquake event

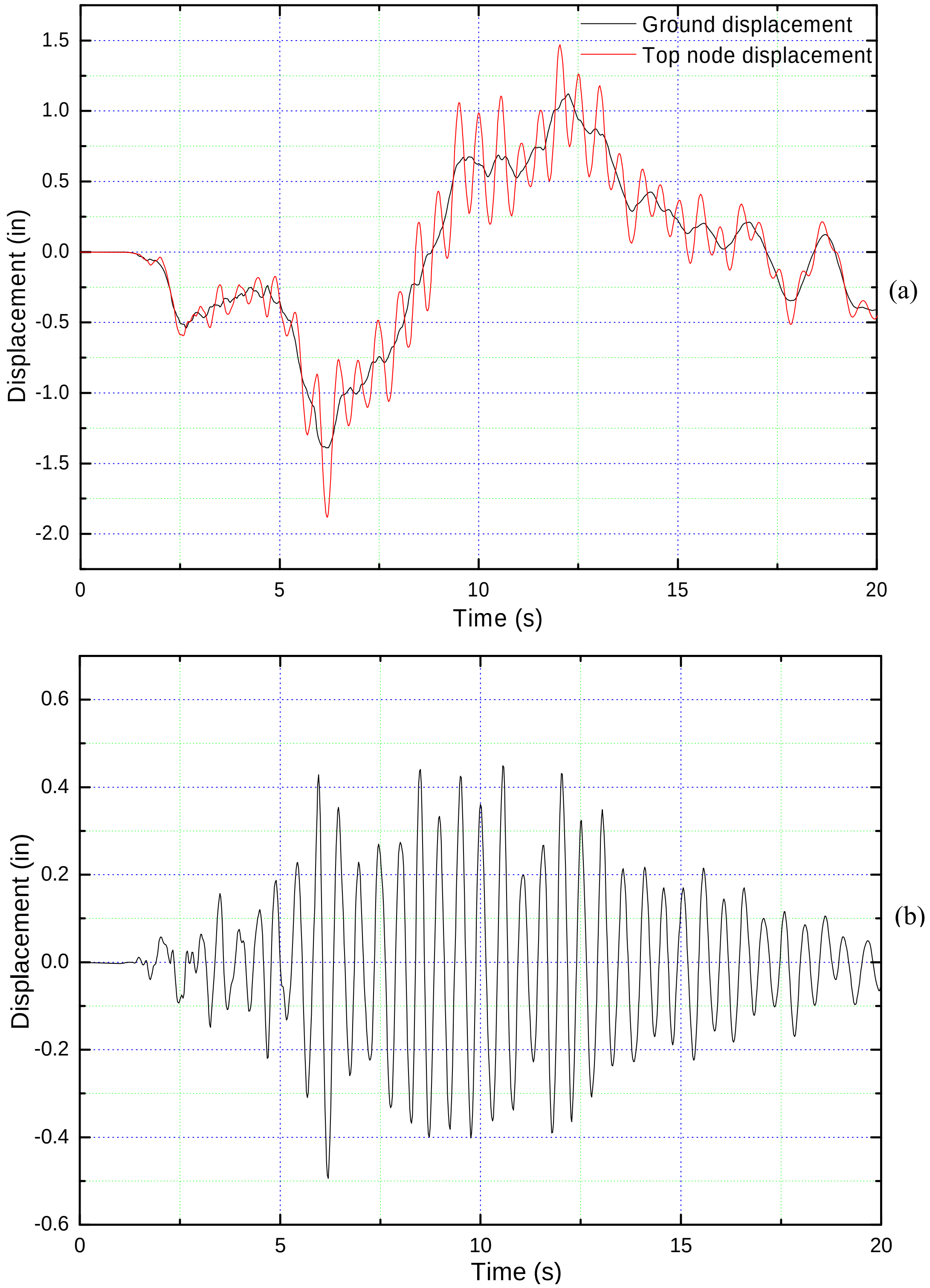

Figure 5.10: (a) Displacement history in the base and top node and (b) drift history of the top node in the transverse direction for 500-year earthquake event

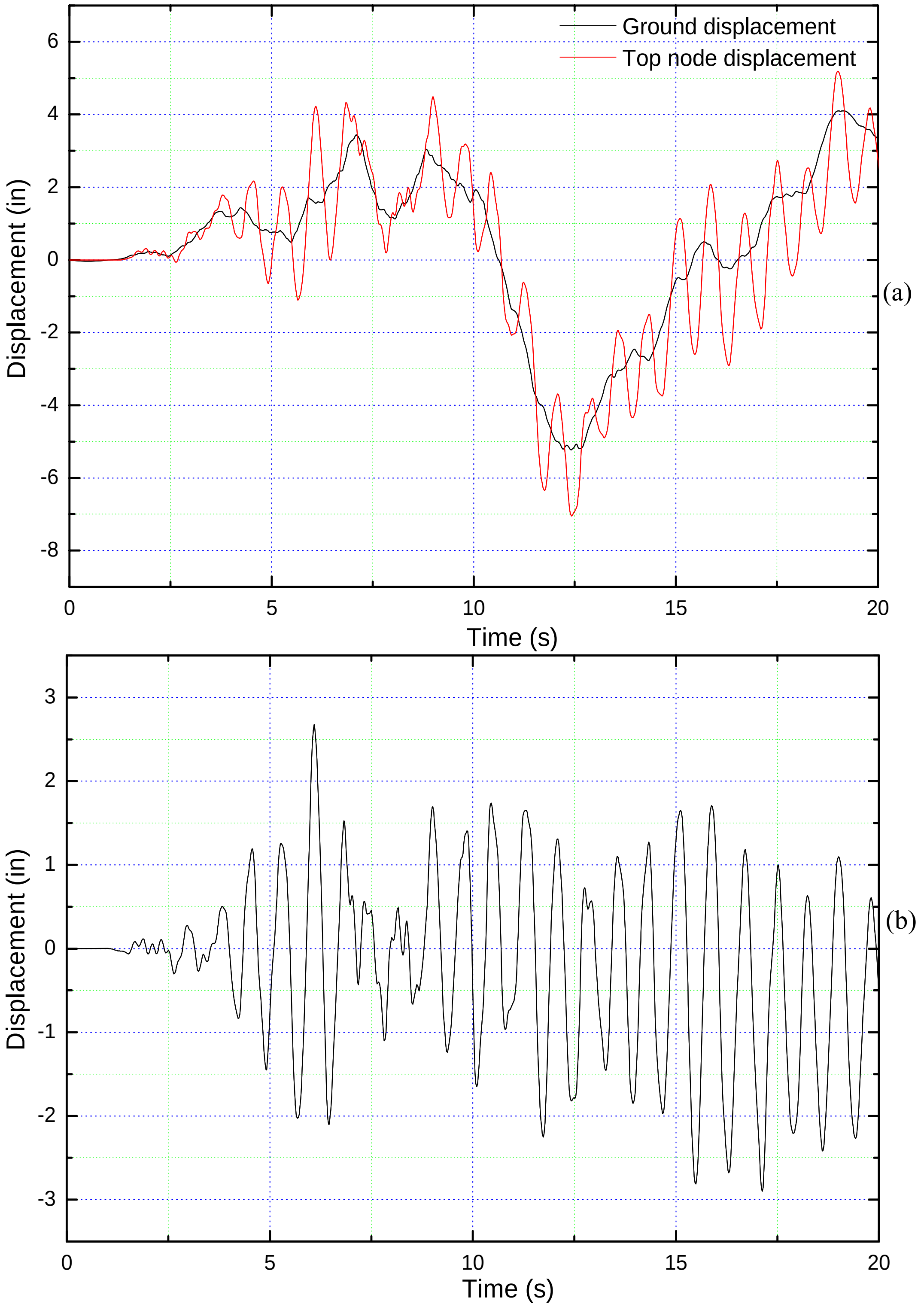

Figure 5.11: (a) Displacement history in the base and top node and (b) drift history of the top node in the longitudinal direction for 2500-year earthquake event

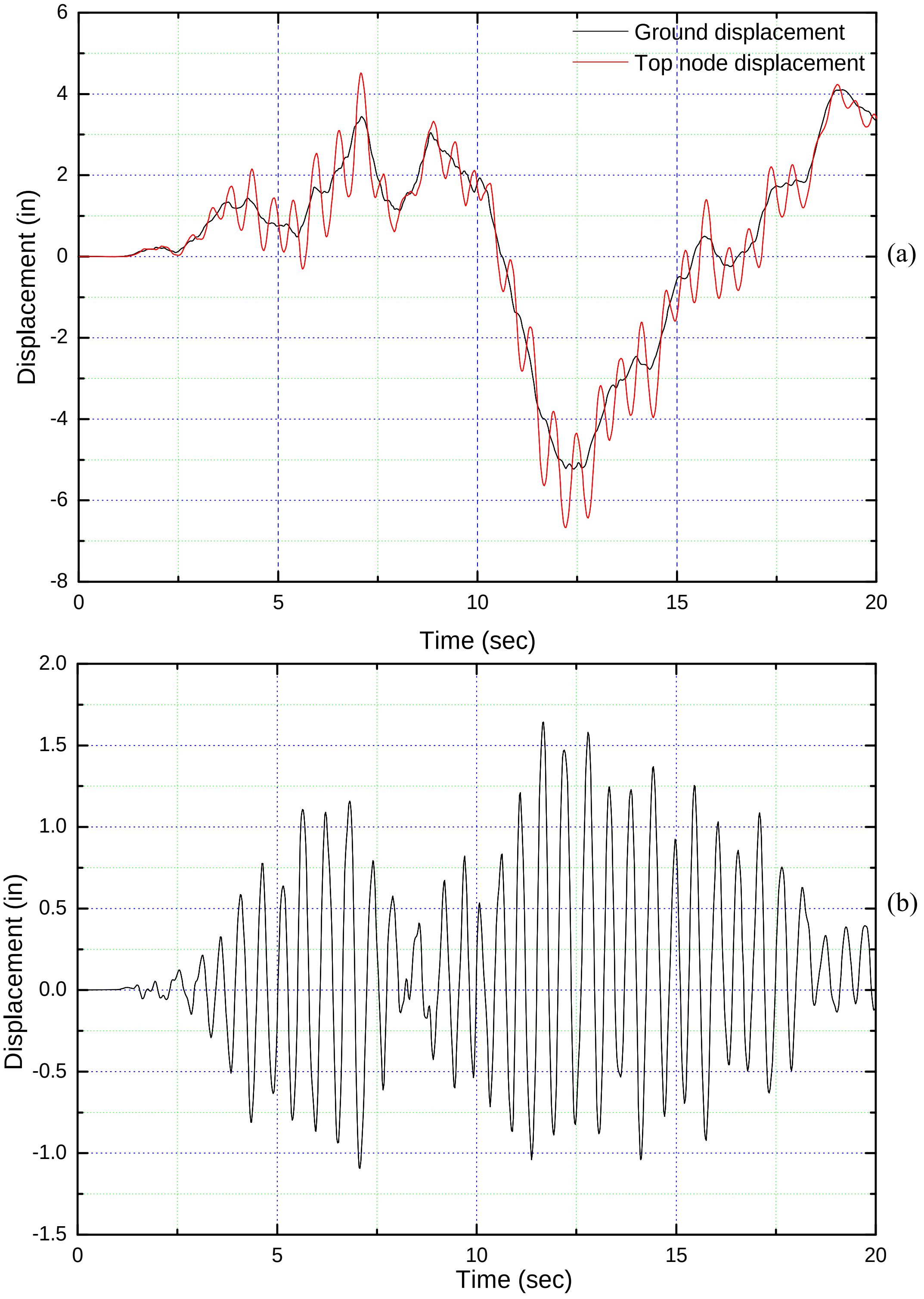

Figure 5.12: (a) Displacement history in the base and the top node; and (b) drift history of the top node in the transverse direction for 2500-year earthquake event

Table 5.4: Maximum drift of the top node in the tower for the 500-year and 2500-year earthquake events

Input motion	Maximum drift in longitudinal direction (in)	Maximum drift in transverse direction (in)
500-year earthquake	1.1	0.5
2500-year earthquake	2.8	1.6

Figure 5.13 displays the contour plots of the tensile damage variables of the masonry tower for the 500-year and 2500-year earthquake events at the time the maximum acceleration of the base nodes occurs. As can be observed from the Figure 5.13a, no tensile damage was observed the 500-year earthquake events, which indicate the bridge tower suffer no damage to primary structural elements under the 500-year earthquake excitation and can satisfy *Functional Evaluation Earthquake (FEE)* design requirements. However, for the 2500-year earthquake events, extensive severe damage was observed in the connection between the arch and base as shown in Figure 5.13b, which suggest that cracks initiate and propagate from these positions, and the tower may collapse eventually. This observation also indicated that the unreinforced masonry structure can not withstand 2500-year earthquake events and can not satisfy the higher seismic design level, i.e. *Safety Evaluation Earthquake (SEE).* Thus, an effective retrofitted measure is demanded to strengthen the tensile resistance of the masonry structure in these positions to overcome the higher level earthquake threat.

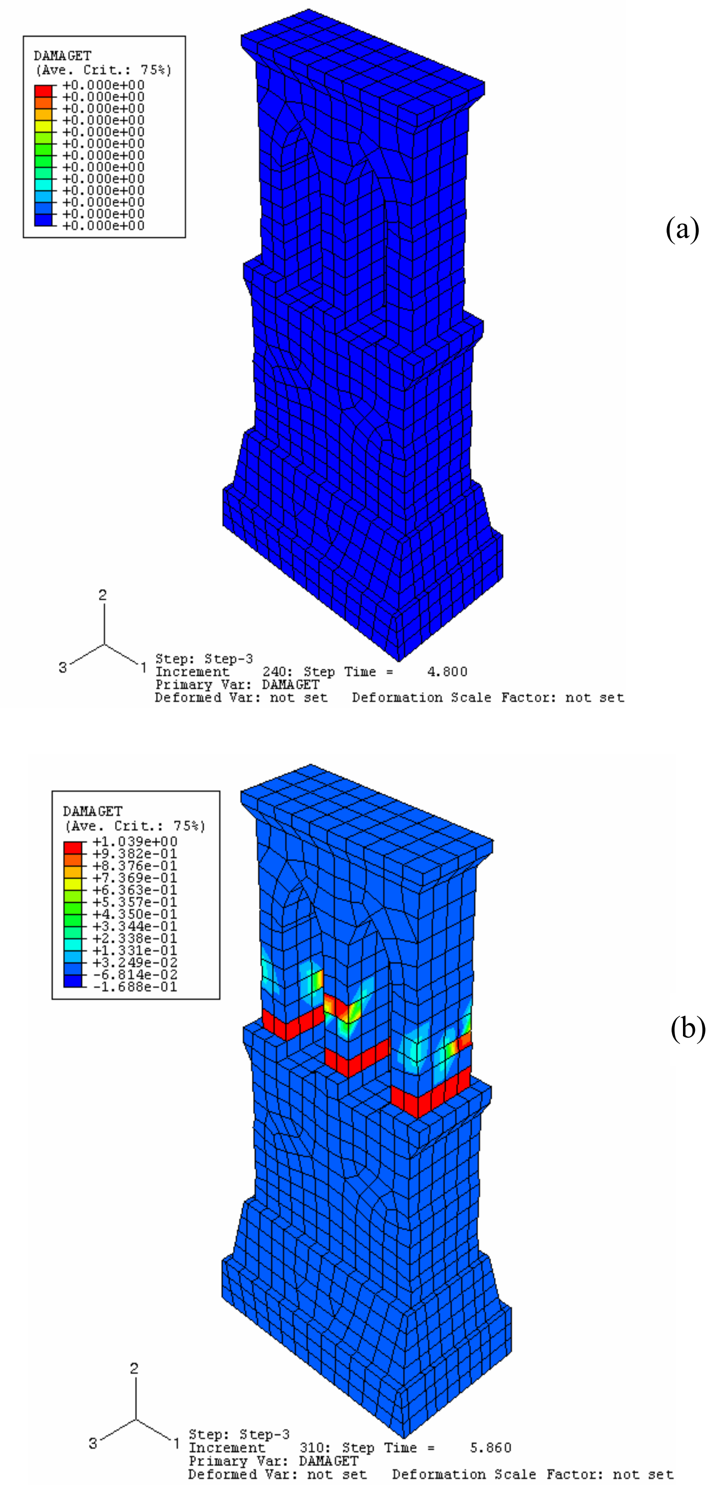

Figure 5.13: Tensile damage distribution at the time with peak acceleration for (a) 500-year earthquake event and (b) 2500-year earthquake event excited in the longitudinal direction.

5.6.2.2 Ground motions excitation from previous earthquake records

Figure 5.14 and 5.15 shows the longitudinal and transverse displacements at the base node and the top nodes of the masonry tower for the Imperial Valley earthquake input case. The displacement of the base node corresponds to the seismic motion imposed. The drift of the top node, which is the displacement difference between the base node and top node, are plotted in the same figure. The maximum drift of the top node in the tower for the longitudinal and transverse direction for three seismic input cases are tabulated in Table 5.5. If compared with Table 5.4 and 5.5, it can be found that the maximum drift for the top node of the tower for all the seismic input cases are bigger than the drift from the 2500-year earthquake event from the NYCDOT seismic design code. This can be attributed to the common characteristics of these earthquake records such as high amplitude and long duration when compared with the response spectrum in the New York City regions (see Figure 5.3 and 5.6). The maximum drift for these three real ground motion records are still less than the allowable target displacement 5.4″. These observations indicate that the deformation of the masonry tower is still acceptable when it is subjected to these seismic excitations.

Table 5.5: Maximum drift of the top node in the tower for the three earthquake inputs

Input motion	Maximum drift in longitudinal direction (in)	Maximum drift in transverse direction (in)
1940 Imperial Valley	4.1	2.2
1994 Northridge	2.8	2.1
Chi-Chi, Taiwan 1999	4.2	2.0

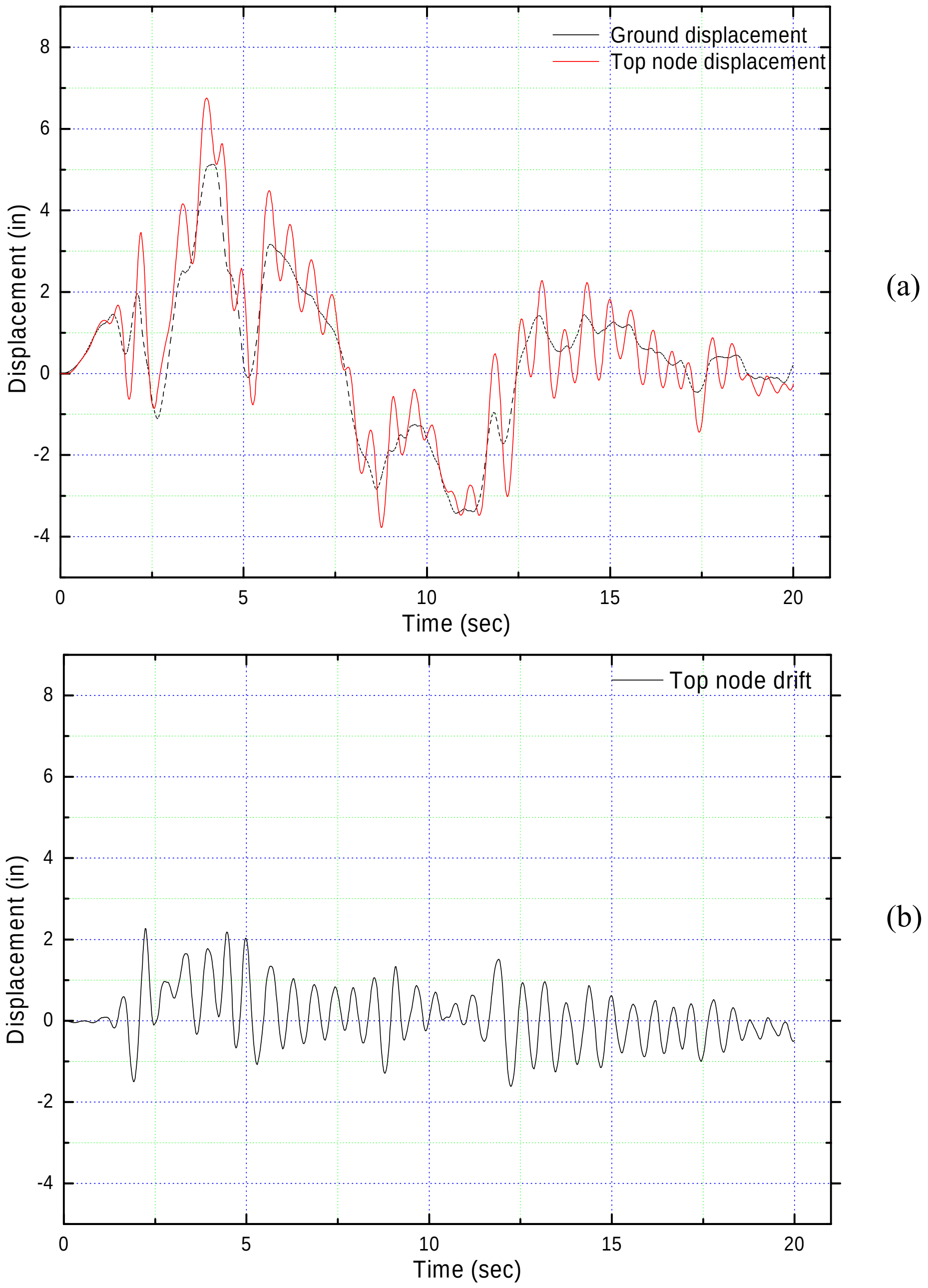

Figure 5.14: (a) Displacement history in the base and the top node; and (b) drift history of the top node in the longitudinal direction for the Imperial Valley earthquake input case

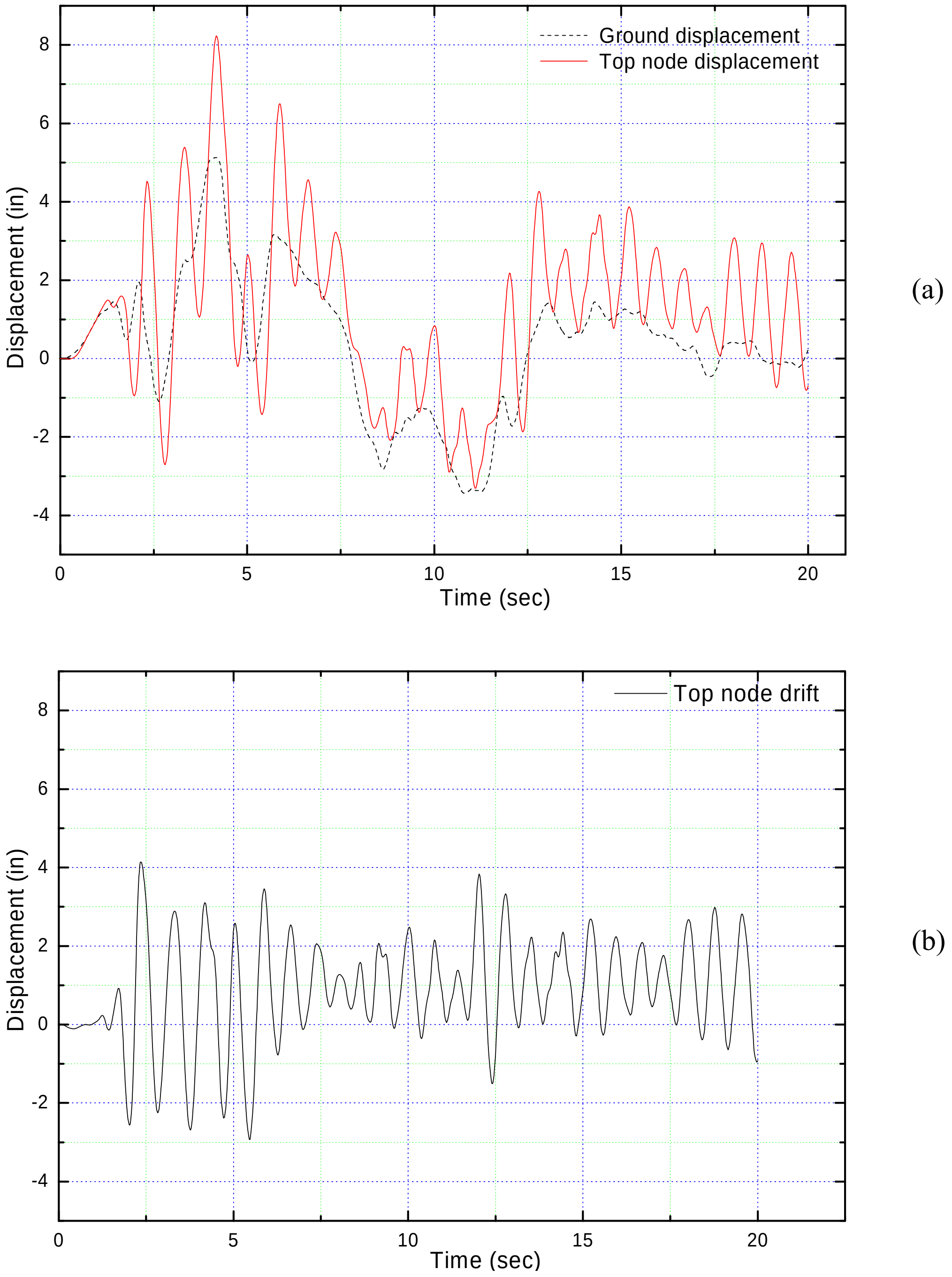

Figure 5.15: (a) Displacement history in the base and the top node; and (b) drift history of the top node in the transverse direction for the Imperial Valley earthquake input case

Figure 5.16 displays the contour plots of the tensile damage variables for the Imperial Valley earthquake case at the time the maximum acceleration of the base nodes occurs. As can be observed from the graphs, an extensive severe damage is also observed in the connection between the arch and base, which further confirms that the weakest regions for the tower appear in the connection regions. This also indicated that an effective retrofitted measure is demanded to strengthen the tensile resistance of the masonry structure in these positions.

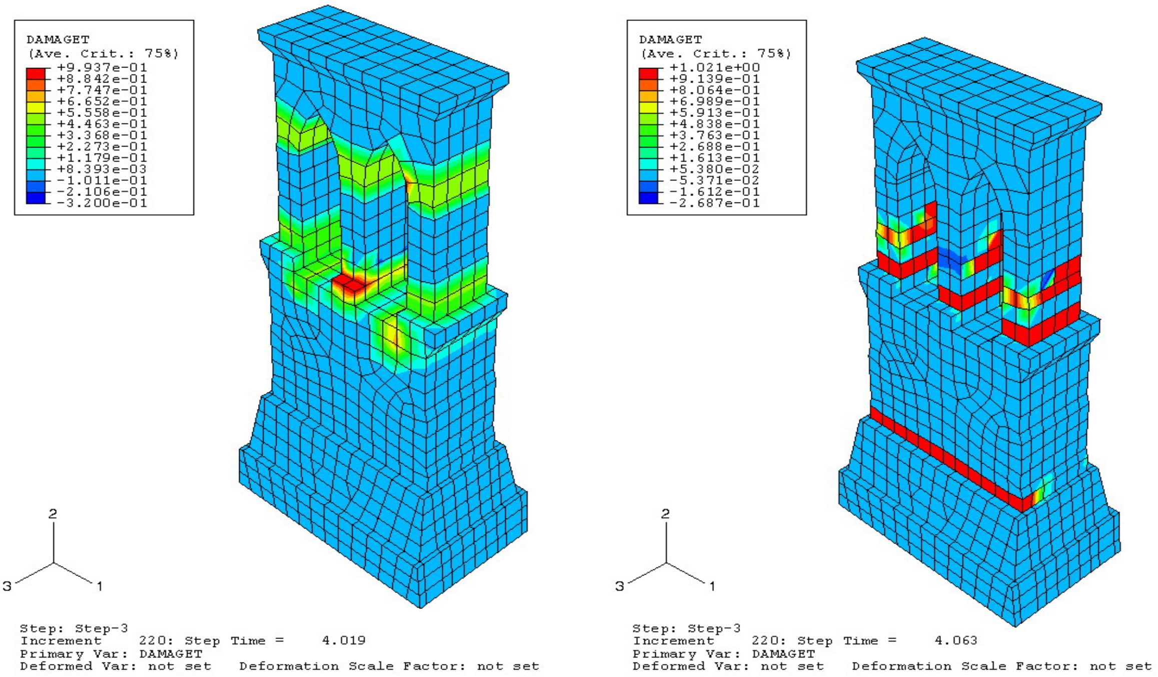

(a) (b)

Figure 5.16: Tensile damage distribution in (a) Longitudinal direction and (b) transverse direction at the time with the peak acceleration for the Imperial Valley earthquake case

5.7. Conclusion

Based on the Mohr-Coulomb models with orthotropic elastic properties of masonry structure obtained by a micro-modeling using the FVDAM model, the seismic response of the unreinforced masonry tower of the Brooklyn Bridge was analyzed using the FEM software ABAQUS. Three different historical earthquake records are scaled to the AASHTO response spectrum in New York City Vicinity and used as the input ground motion in the numerical simulation. The primary mode shapes for the masonry tower were identified with the modal analysis. It was found that longitudinal bending mode is dominant over the transverse bending mode and torsion mode. Time history analyses indicate that the whole tower still retains the global structural stability and some local damages appear. The maximum drift for the tower top is less than the allowable ground vibration amplitudes estimated by FEMA-273. The drift ratio of the tower is about 0.3% and is satisfied with the requirement of the code for seismic performance design objective of life safety. These observations indicate that the deformation of the masonry tower is acceptable when it is subjected to a design seismic excitation. The most severe tensile damages occur in the corner between the arch and base of the tower and crack initiate in these positions, which suggest that cracks initiate from these positions. This observation also indicated that an effective retrofitted measure is demanded to strengthen the tensile resistance of the masonry structure in these positions.

Chapter 6: Conclusion

This dissertation presents an experimental and numerical study of the masonry structure. This study involves: (a) an experimental investigation of granite masonry structure under uniaxial compression; (b) development of a micromechanics-based model to simulate the elastic-plastic behavior of masonry structure; and (c) the macro FEM modeling of masonry structures under seismic excitation. The general conclusion for each section is summarized in the following sections.

Experimental research

Extensive uniaxial compressive tests were performed on granite stone masonry prism and its constituents, granite stone and cement mortar, separately. With the Digital Image Correlation technique, these strain mappings for different loading stages were obtained to track crack initiation and propagation in the masonry structure. For the first time, we experimentally obtain full-field quantitative strain maps of localization in granite masonry structure and we have been able to probe its development in terms of strain. Based on the experimental results, the conclusions can be summarized in the following:

1. Granite stone specimens showed pronounced fragile behaviour after peak load. The failure modes showed that cracks ran continuously through the specimen and the failure through this shear band was the cause of specimen collapse.

2. The mortar specimen exhibits a much less stiffer behavior than granite stone, which was also confirmed by another source from Vibrational Resonance Frequency test.

The stress-strain relation for the mortar specimen showed a strain hardening behaviour, which suggests that mortar has more ductility than granite stone.

3. The stress-strain relation for the masonry prism exposes a bilinear strain hardening behaviour and present much more ductility than the granite stone unit and mortar specimen. The average strength value of the masonry prisms was much higher than the mortar specimens, but less than the average strength of the single granite stone unit, which indicate that the compressive strength of the masonry was highly influenced by the characteristics of the single components, unit and mortar.

4. With the obtained DIC mapping strain contours for the masonry prisms during the different loading phases, it was observed that cracks initiated at the vertical mortar-joint and propagated thereafter through other horizontal mortar join. The initiation of these cracks is due to the formation of multiple shear bands in the unit-mortar interface. Further deformation occurs by the extending the shear bands into all the mortar joint layers. Finally the granite unit split vertically due to the biaxial tensile force induced by the confinement of mortar joints.

5. These strain mappings obtained by Digital Image Correlation was used to o track crack propagation in granite masonry structure, which suggest that Digital Image Correlation is a promising technique in experimental mechanics because it is capable of giving full-field quantitative information of deformation and strain.

Micro modeling

The micromechanics-based FVDAM model has been modified and enhanced for the mechanical analysis of multiphase material containing elasticplastic phases. The accuracy and efficiency of the FVDAM model predicting mechanical behavior of multiphase composite material was validated by comparing with FEM results from the commercial software FEMLAB. The results indicate that the FVDAM model is capable of predicting both macroscopic and microscopic response accurately.

The FVDAM model was also applied to masonry structure composed of granite stone and cement mortar at the first time. The extensive parametric analysis was made to understand the effect of the mesh size, cell texture, mortar elastic modulus and mortar volume fraction on the homogenized/effective elastic properties. It was found that mesh size and texture of the repeating unit cell has no much influence on the effective elastic properties of the composites. However, the mortar elastic modulus and the mortar volume fraction will affect the overall effective stiffness of the masonry composite significantly. It was also observed that the mortar elastic modulus has much more effect on the averaged in-plane stiffness than on the out-of-plane stiffness. The overall effective stiffness of the masonry composite is approximately inversely to the mortar volume fraction.

Finally, elastic-plastic analyses were carried out on the granite masonry structure to compare with the experimental results. It was observed that the macroscopic stress-strain response predicted by the FVDAM correlates well with the experimental results. The experimental-analytical correlation also demonstrates the FVDAM model has a good capability in predicting the response of masonry structure if the individual mechanical behavior of its constituents (i.e., granite unit and cement mortar) is known. The initiation and evolution of effective plastic strain distributions was also obtained during vertical compressive plastic loading using the FVDAM model. It was found that plastic zone initiates and propagates through mortar layers and finally the masonry structure fails until mortar failure.

Macro modeling

Based on the Mohr-Coulomb models with orthotropic elastic properties of masonry structure obtained by a micro-modeling using the FVDAM model, the seismic response of the unreinforced masonry tower of the Brooklyn Bridge was analyzed using the FEM software ABAQUS. Three different historical earthquake records are scaled to the 2500-year AASHTO design earthquake in New York City Vicinity and used as the input ground motion in the numerical simulation. The primary mode shapes for the masonry tower were identified with the modal analysis. It was found that longitudinal bending mode is dominant over the transverse bending mode and torsion mode. Time history analyses indicate that the whole tower still retains the global structural stability and some local damages appear. The maximum drift for the tower top is less than the allowable ground vibration amplitudes estimated by FEMA-273. The drift ratio of the tower is about 0.3% and is satisfied with the requirement of the code for seismic performance design objective of life safety. These observations indicate that the deformation of the masonry tower is acceptable when it is subjected to a design seismic excitation. The most severe tensile damages occur in the corner between the arch and base of the tower and crack initiate in these positions, which suggest that cracks initiate from these positions. This observation also indicated that an effective retrofitted measure is demanded to strengthen the tensile resistance of the masonry structure in these positions.

Appendices

Appendix A: Local stiffness matrix

The surface-averaged tractions can be expressed in terms of the subcell microvariables and applied macroscopic strains as follows:

$$\begin{bmatrix} \overline{t}_1^{2+} \\ \overline{t}_1^{2-} \end{bmatrix}^{(\beta,\gamma)} = C_{66}^{(\beta,\gamma)} \begin{bmatrix} 1 & \frac{3h_\beta}{2} \\ -1 & \frac{3h_\beta}{2} \end{bmatrix} \begin{bmatrix} W_{1(10)} \\ W_{1(20)} \end{bmatrix}^{(\beta,\gamma)} + 2C_{66}^{(\beta,\gamma)} \begin{bmatrix} \overline{\varepsilon}_{12} \\ -\overline{\varepsilon}_{12} \end{bmatrix} - \sum_{m=0}^{\infty} \sqrt{(1+2m)}\,\tau_{21(m0)}^{(\beta,\gamma)} \begin{bmatrix} 1 \\ (-1)^{m+1} \end{bmatrix} \tag{A.1}$$

$$\begin{bmatrix} \overline{t}_1^{3+} \\ \overline{t}_1^{3-} \end{bmatrix}^{(\beta,\gamma)} = C_{55}^{(\beta,\gamma)} \begin{bmatrix} 1 & \frac{3l_\gamma}{2} \\ -1 & \frac{3l_\gamma}{2} \end{bmatrix} \begin{bmatrix} W_{1(01)} \\ W_{1(02)} \end{bmatrix}^{(\beta,\gamma)} + 2C_{55}^{(\beta,\gamma)} \begin{bmatrix} \overline{\varepsilon}_{13} \\ -\overline{\varepsilon}_{13} \end{bmatrix} - \sum_{n=0}^{\infty} \sqrt{(1+2n)}\,\tau_{31(0n)}^{(\beta,\gamma)} \begin{bmatrix} 1 \\ (-1)^{n+1} \end{bmatrix} \tag{A.2}$$

$$\begin{bmatrix} \overline{t}_2^{2+} \\ \overline{t}_2^{2-} \end{bmatrix}^{(\beta,\gamma)} = C_{22}^{(\beta,\gamma)} \begin{bmatrix} 1 & \frac{3h_\beta}{2} \\ -1 & \frac{3h_\beta}{2} \end{bmatrix} \begin{bmatrix} W_{2(10)} \\ W_{2(20)} \end{bmatrix}^{(\beta,\gamma)} + C_{23}^{(\beta,\gamma)} \begin{bmatrix} W_{3(01)} \\ -W_{3(01)} \end{bmatrix}^{(\beta,\gamma)} - \sum_{m=0}^{\infty} \sqrt{(1+2m)}\,\tau_{22(m0)}^{(\beta,\gamma)} \begin{bmatrix} 1 \\ (-1)^{m+1} \end{bmatrix} \tag{A.3}$$

$$\begin{bmatrix} \overline{t}_2^{3+} \\ \overline{t}_2^{3-} \end{bmatrix}^{(\beta,\gamma)} = C_{44}^{(\beta,\gamma)} \begin{bmatrix} 1 & \frac{3l_\gamma}{2} \\ -1 & \frac{3l_\gamma}{2} \end{bmatrix} \begin{bmatrix} W_{2(01)} \\ W_{2(02)} \end{bmatrix}^{(\beta,\gamma)} + C_{44}^{(\beta,\gamma)} \begin{bmatrix} W_{3(10)} \\ -W_{3(10)} \end{bmatrix}^{(\beta,\gamma)} + 2C_{44}^{(\beta,\gamma)} \begin{bmatrix} \overline{\varepsilon}_{23} \\ -\overline{\varepsilon}_{23} \end{bmatrix} - \sum_{n=0}^{\infty} \sqrt{(1+2n)}\,\tau_{32(0n)}^{(\beta,\gamma)} \begin{bmatrix} 1 \\ (-1)^{n+1} \end{bmatrix} \tag{A.4}$$

$$\begin{bmatrix} \overline{t}_3^{2+} \\ \overline{t}_3^{2-} \end{bmatrix}^{(\beta,\gamma)} = C_{44}^{(\beta,\gamma)} \begin{bmatrix} 1 & \frac{3h_\beta}{2} \\ -1 & \frac{3h_\beta}{2} \end{bmatrix} \begin{bmatrix} W_{3(10)} \\ W_{3(20)} \end{bmatrix}^{(\beta,\gamma)} + C_{44}^{(\beta,\gamma)} \begin{bmatrix} W_{2(01)} \\ -W_{2(01)} \end{bmatrix}^{(\beta,\gamma)} + 2C_{44}^{(\beta,\gamma)} \begin{bmatrix} \overline{\varepsilon}_{23} \\ -\overline{\varepsilon}_{23} \end{bmatrix} - \sum_{m=0}^{\infty} \sqrt{(1+2m)}\,\tau_{23(m0)}^{(\beta,\gamma)} \begin{bmatrix} 1 \\ (-1)^{m+1} \end{bmatrix} \tag{A.5}$$

$$\begin{bmatrix} \overline{t}_3^{3+} \\ \overline{t}_3^{3-} \end{bmatrix}^{(\beta,\gamma)} = C_{33}^{(\beta,\gamma)} \begin{bmatrix} 1 & \frac{3l_\gamma}{2} \\ -1 & \frac{3l_\gamma}{2} \end{bmatrix} \begin{bmatrix} W_{3(01)} \\ W_{3(02)} \end{bmatrix}^{(\beta,\gamma)} + C_{23}^{(\beta,\gamma)} \begin{bmatrix} W_{2(10)} \\ -W_{2(10)} \end{bmatrix}^{(\beta,\gamma)} - \sum_{n=0}^{\infty} \sqrt{(1+2n)}\,\tau_{33(0n)}^{(\beta,\gamma)} \begin{bmatrix} 1 \\ (-1)^{n+1} \end{bmatrix} \tag{A.6}$$

Appendix B: Microvariable

Microvariables in terms of surface-averaged fluctuating displacements

$$\begin{bmatrix} W_{1(10)} \\ W_{1(20)} \end{bmatrix}^{(\beta,\gamma)} = \begin{bmatrix} \dfrac{1}{h_\beta} & -\dfrac{1}{h_\beta} \\ \dfrac{2}{h_\beta^2} & \dfrac{2}{h_\beta^2} \end{bmatrix} \begin{bmatrix} \overline{u}_1'^{2+} \\ \overline{u}_1'^{2-} \end{bmatrix}^{(\beta,\gamma)} - \frac{4}{h_\beta^2} \begin{bmatrix} 0 \\ W_{1(00)} \end{bmatrix}^{(\beta,\gamma)} \tag{B(1)}$$

$$\begin{bmatrix} W_{1(01)} \\ W_{1(02)} \end{bmatrix}^{(\beta,\gamma)} = \begin{bmatrix} \dfrac{1}{l_\gamma} & -\dfrac{1}{l_\gamma} \\ \dfrac{2}{l_\gamma^2} & \dfrac{2}{l_\gamma^2} \end{bmatrix} \begin{bmatrix} \overline{u}_1'^{3+} \\ \overline{u}_1'^{3-} \end{bmatrix}^{(\beta,\gamma)} - \frac{4}{l_\gamma^2} \begin{bmatrix} 0 \\ W_{1(00)} \end{bmatrix}^{(\beta,\gamma)} \tag{B(2)}$$

$$\begin{bmatrix} W_{2(10)} \\ W_{2(20)} \end{bmatrix}^{(\beta,\gamma)} = \begin{bmatrix} \dfrac{1}{h_\beta} & -\dfrac{1}{h_\beta} \\ \dfrac{2}{h_\beta^2} & \dfrac{2}{h_\beta^2} \end{bmatrix} \begin{bmatrix} \overline{u}_2'^{2+} \\ \overline{u}_2'^{2-} \end{bmatrix}^{(\beta,\gamma)} - \frac{4}{h_\beta^2} \begin{bmatrix} 0 \\ W_{2(00)} \end{bmatrix}^{(\beta,\gamma)} \tag{B(3)}$$

$$\begin{bmatrix} W_{3(10)} \\ W_{3(20)} \end{bmatrix}^{(\beta,\gamma)} = \begin{bmatrix} \dfrac{1}{h_\beta} & -\dfrac{1}{h_\beta} \\ \dfrac{2}{h_\beta^2} & \dfrac{2}{h_\beta^2} \end{bmatrix} \begin{bmatrix} \overline{u}_3'^{2+} \\ \overline{u}_3'^{2-} \end{bmatrix}^{(\beta,\gamma)} - \frac{4}{h_\beta^2} \begin{bmatrix} 0 \\ W_{3(00)} \end{bmatrix}^{(\beta,\gamma)} \tag{B(4)}$$

$$\begin{bmatrix} W_{2(01)} \\ W_{2(02)} \end{bmatrix}^{(\beta,\gamma)} = \begin{bmatrix} \dfrac{1}{l_\gamma} & -\dfrac{1}{l_\gamma} \\ \dfrac{2}{l_\gamma^2} & \dfrac{2}{l_\gamma^2} \end{bmatrix} \begin{bmatrix} \overline{u}_2'^{3+} \\ \overline{u}_2'^{3-} \end{bmatrix}^{(\beta,\gamma)} - \frac{4}{l_\gamma^2} \begin{bmatrix} 0 \\ W_{2(00)} \end{bmatrix}^{(\beta,\gamma)} \tag{B(5)}$$

$$\begin{bmatrix} W_{3(01)} \\ W_{3(02)} \end{bmatrix}^{(\beta,\gamma)} = \begin{bmatrix} \dfrac{1}{l_\gamma} & -\dfrac{1}{l_\gamma} \\ \dfrac{2}{l_\gamma^2} & \dfrac{2}{l_\gamma^2} \end{bmatrix} \begin{bmatrix} \overline{u}_3'^{3+} \\ \overline{u}_3'^{3-} \end{bmatrix}^{(\beta,\gamma)} - \frac{4}{l_\gamma^2} \begin{bmatrix} 0 \\ W_{3(00)} \end{bmatrix}^{(\beta,\gamma)} \tag{B(6)}$$

Where, the three zeroth order microvariables can be expressed entirely in terms of the surface-averaged fluctuating displacements by satisfying the stress equilibrium equations in each subcell.

$$W_{1(00)}^{(\beta,\gamma)} = \frac{C_{66}^{(\beta,\gamma)}}{2\left(C_{66}^{(\beta,\gamma)} + \frac{h_\beta^2}{l_\gamma^2} C_{55}^{(\beta,\gamma)}\right)} (\bar{u}_1^{2+} + \bar{u}_1^{2-})^{(\beta,\gamma)} + \frac{h_\beta^2 C_{55}^{(\beta,\gamma)}}{2 l_\gamma^2 \left(C_{66}^{(\beta,\gamma)} + \frac{h_\beta^2}{l_\gamma^2} C_{55}^{(\beta,\gamma)}\right)} (\bar{u}_1^{3+} + \bar{u}_1^{3-})^{(\beta,\gamma)} -$$

$$\frac{1}{6\bar{C}_{11}^{(\beta,\gamma)}} \left[h_\beta \sum_{m=1,3,5,\ldots}^{\infty} \sqrt{(1+2m)}\,\tau_{21(m0)}^{in(\beta,\gamma)} + \frac{h_\beta^2}{l_\gamma} \sum_{n=1,3,5,\ldots}^{\infty} \sqrt{1+2n}\,\tau_{31(0n)}^{in(\beta,\gamma)} \right]$$

(B7)

$$W_{2(00)}^{(\beta,\gamma)} = \frac{C_{22}^{(\beta,\gamma)}}{2\left(C_{22}^{(\beta,\gamma)} + \frac{h_\beta^2}{l_\gamma^2} C_{33}^{(\beta,\gamma)}\right)} (\bar{u}_2^{2+} + \bar{u}_2^{2-})^{(\beta,\gamma)} + \frac{h_\beta^2 C_{44}^{(\beta,\gamma)}}{2 l_\gamma^2 \left(C_{22}^{(\beta,\gamma)} + \frac{h_\beta^2}{l_\gamma^2} C_{33}^{(\beta,\gamma)}\right)} (\bar{u}_2^{3+} + \bar{u}_2^{3-})^{(\beta,\gamma)} -$$

$$\frac{1}{6\bar{C}_{22}^{(\beta,\gamma)}} \left[h_\beta \sum_{m=1,3,5,\ldots}^{\infty} \sqrt{(1+2m)}\,\tau_{22(m0)}^{in(\beta,\gamma)} + \frac{h_\beta^2}{l_\gamma} \sum_{n=1,3,5,\ldots}^{\infty} \sqrt{1+2n}\,\tau_{32(0n)}^{in(\beta,\gamma)} \right]$$

(B8)

$$W_{3(00)}^{(\beta,\gamma)} = \frac{C_{44}^{(\beta,\gamma)}}{2\left(C_{33}^{(\beta,\gamma)} + \frac{h_\beta^2}{l_\gamma^2} C_{44}^{(\beta,\gamma)}\right)} (\bar{u}_3^{2+} + \bar{u}_3^{2-})^{(\beta,\gamma)} + \frac{h_\beta^2 C_{55}^{(\beta,\gamma)}}{2 l_\gamma^2 \left(C_{33}^{(\beta,\gamma)} + \frac{h_\beta^2}{l_\gamma^2} C_{44}^{(\beta,\gamma)}\right)} (\bar{u}_3^{3+} + \bar{u}_3^{3-})^{(\beta,\gamma)} -$$

$$\frac{1}{6\bar{C}_{33}^{(\beta,\gamma)}} \left[\frac{l_\gamma^2}{h_\beta} \sum_{m=1,3,5,\ldots}^{\infty} \sqrt{(1+2m)}\,\tau_{23(m0)}^{in(\beta,\gamma)} + \frac{h_\beta^2}{l_\gamma} \sum_{n=1,3,5,\ldots}^{\infty} \sqrt{1+2n}\,\tau_{33(0n)}^{in(\beta,\gamma)} \right]$$

(B9)

where

$$\bar{C}_{11}^{(\beta,\gamma)} = C_{66}^{(\beta,\gamma)} + \frac{h_\beta^2}{l_\gamma^2} C_{55}^{(\beta,\gamma)}, \quad \bar{C}_{22}^{(\beta,\gamma)} = C_{22}^{(\beta,\gamma)} + \frac{h_\beta^2}{l_\gamma^2} C_{33}^{(\beta,\gamma)}, \quad \bar{C}_{33}^{(\beta,\gamma)} = C_{33}^{(\beta,\gamma)} + \frac{l_\gamma^2}{h_\beta^2} C_{44}^{(\beta,\gamma)}$$

Appendix C: Global stiffness matrix

$$\begin{bmatrix} \bar{t}_1^{2+} \\ \bar{t}_1^{2-} \\ \bar{t}_1^{3+} \\ \bar{t}_1^{3-} \end{bmatrix} = \begin{bmatrix} L_{11} & L_{12} & L_{13} & L_{14} \\ L_{21} & L_{22} & L_{23} & L_{24} \\ L_{31} & L_{32} & L_{33} & L_{34} \\ L_{41} & L_{42} & L_{43} & L_{44} \end{bmatrix}^{(\beta,\gamma)} \begin{bmatrix} \bar{u}_1'^{2+} \\ \bar{u}_1'^{2-} \\ \bar{u}_1'^{3+} \\ \bar{u}_1'^{3-} \end{bmatrix} + 2 \begin{bmatrix} C_{66} & 0 \\ -C_{66} & 0 \\ 0 & C_{55} \\ 0 & -C_{55} \end{bmatrix} \begin{bmatrix} \bar{\varepsilon}_{12} \\ \bar{\varepsilon}_{13} \end{bmatrix} + \begin{bmatrix} g_{o1} \\ g_{o2} \\ g_{o3} \\ g_{o4} \end{bmatrix} \tag{C1}$$

$$\begin{bmatrix} \bar{t}_2^{2+} \\ \bar{t}_2^{2-} \\ \bar{t}_3^{2+} \\ \bar{t}_3^{2-} \\ \bar{t}_2^{3+} \\ \bar{t}_2^{3-} \\ \bar{t}_3^{3+} \\ \bar{t}_3^{3-} \end{bmatrix} = \begin{bmatrix} K_{11} & K_{12} & 0 & 0 & K_{15} & K_{16} & K_{17} & K_{18} \\ K_{21} & K_{22} & 0 & 0 & K_{25} & K_{26} & K_{27} & K_{28} \\ 0 & 0 & K_{33} & K_{34} & K_{35} & K_{36} & K_{37} & K_{38} \\ 0 & 0 & K_{43} & K_{44} & K_{45} & K_{46} & K_{47} & K_{48} \\ K_{51} & K_{52} & K_{53} & K_{54} & K_{55} & K_{56} & 0 & 0 \\ K_{61} & K_{62} & K_{63} & K_{64} & K_{65} & K_{66} & 0 & 0 \\ K_{71} & K_{72} & K_{73} & K_{74} & 0 & 0 & K_{77} & K_{78} \\ K_{81} & K_{82} & K_{83} & K_{84} & 0 & 0 & K_{87} & K_{88} \end{bmatrix}^{(\beta,\gamma)} \begin{bmatrix} \bar{u}_2'^{2+} \\ \bar{u}_2'^{2-} \\ \bar{u}_3'^{2+} \\ \bar{u}_3'^{2-} \\ \bar{u}_2'^{3+} \\ \bar{u}_2'^{3-} \\ \bar{u}_3'^{3+} \\ \bar{u}_3'^{3-} \end{bmatrix} + \begin{bmatrix} C_{11} & C_{22} & C_{23} & 0 \\ -C_{12} & -C_{22} & -C_{23} & 0 \\ 0 & 0 & 0 & 2C_{44} \\ 0 & 0 & 0 & -2C_{44} \\ 0 & 0 & 0 & 2C_{44} \\ 0 & 0 & 0 & -2C_{44} \\ C_{13} & C_{23} & C_{33} & 0 \\ -C_{13} & -C_{23} & -C_{33} & 0 \end{bmatrix}^{(\beta,\gamma)} \begin{bmatrix} \bar{\varepsilon}_{11} \\ \bar{\varepsilon}_{22} \\ \bar{\varepsilon}_{33} \\ \bar{\varepsilon}_{23} \end{bmatrix} + \begin{bmatrix} g_{i1} \\ g_{i2} \\ g_{i3} \\ g_{i4} \\ g_{i5} \\ g_{i6} \\ g_{i7} \\ g_{i8} \end{bmatrix} \tag{C2}$$

In the above equations, Elements of Gloabla Stiffness Matrices are displayed below:

$$\begin{aligned}
K_{11}^{(\beta,\gamma)} &= K_{22}^{(\beta,\gamma)} = \frac{C_{22}^{(\beta,\gamma)}}{h_\beta}\left(4-3\frac{C_{22}^{(\beta,\gamma)}}{\bar{C}_{22}^{(\beta,\gamma)}}\right) \\
K_{12}^{(\beta,\gamma)} &= K_{21}^{(\beta,\gamma)} = \frac{C_{22}^{(\beta,\gamma)}}{h_\beta}\left(2-3\frac{C_{22}^{(\beta,\gamma)}}{\bar{C}_{22}^{(\beta,\gamma)}}\right) \\
K_{15}^{(\beta,\gamma)} &= K_{16}^{(\beta,\gamma)} = K_{25}^{(\beta,\gamma)} = K_{26}^{(\beta,\gamma)} = -\frac{3C_{22}^{(\beta,\gamma)}C_{44}^{(\beta,\gamma)}h_\beta}{\bar{C}_{22}^{(\beta,\gamma)}l_\gamma^2} \\
K_{17}^{(\beta,\gamma)} &= -K_{18}^{(\beta,\gamma)} = -K_{27}^{(\beta,\gamma)} = K_{28}^{(\beta,\gamma)} = \frac{C_{23}^{(\beta,\gamma)}}{l_\gamma}
\end{aligned} \tag{C3}$$

$$\begin{aligned}
K_{33}^{(\beta,\gamma)} &= K_{44}^{(\beta,\gamma)} = \frac{C_{44}^{(\beta,\gamma)}}{h_\beta}\left(4-3\frac{l_\gamma^2C_{44}^{(\beta,\gamma)}}{h_\beta^2\bar{C}_{33}^{(\beta,\gamma)}}\right) \\
K_{34}^{(\beta,\gamma)} &= K_{43}^{(\beta,\gamma)} = \frac{C_{44}^{(\beta,\gamma)}}{h_\beta}\left(2-3\frac{l_\gamma^2C_{44}^{(\beta,\gamma)}}{h_\beta^2\bar{C}_{33}^{(\beta,\gamma)}}\right) \\
K_{35}^{(\beta,\gamma)} &= -K_{36}^{(\beta,\gamma)} = -K_{45}^{(\beta,\gamma)} = K_{46}^{(\beta,\gamma)} = -\frac{C_{44}^{(\beta,\gamma)}}{l_\gamma} \\
K_{37}^{(\beta,\gamma)} &= K_{38}^{(\beta,\gamma)} = K_{47}^{(\beta,\gamma)} = K_{48}^{(\beta,\gamma)} = -\frac{3C_{33}^{(\beta,\gamma)}C_{44}^{(\beta,\gamma)}}{h_\beta\bar{C}_{33}^{(\beta,\gamma)}}
\end{aligned} \tag{C4}$$

$$\begin{aligned}
K_{51}^{(\beta,\gamma)} &= K_{52}^{(\beta,\gamma)} = K_{61}^{(\beta,\gamma)} = K_{62}^{(\beta,\gamma)} = -\frac{3C_{22}^{(\beta,\gamma)}C_{44}^{(\beta,\gamma)}}{l_\gamma\bar{C}_{22}^{(\beta,\gamma)}} \\
K_{53}^{(\beta,\gamma)} &= -K_{54}^{(\beta,\gamma)} = -K_{63}^{(\beta,\gamma)} = K_{64}^{(\beta,\gamma)} = \frac{C_{44}^{(\beta,\gamma)}}{h_\beta} \\
K_{55}^{(\beta,\gamma)} &= K_{66}^{(\beta,\gamma)} = \frac{C_{44}^{(\beta,\gamma)}}{l_\gamma}\left(4-3\frac{h_\beta^2C_{44}^{(\beta,\gamma)}}{l_\gamma^2\bar{C}_{22}^{(\beta,\gamma)}}\right) \\
K_{56}^{(\beta,\gamma)} &= K_{65}^{(\beta,\gamma)} = \frac{C_{44}^{(\beta,\gamma)}}{l_\gamma}\left(2-3\frac{h_\beta^2C_{44}^{(\beta,\gamma)}}{l_\gamma^2\bar{C}_{22}^{(\beta,\gamma)}}\right)
\end{aligned} \tag{C5}$$

$$
\begin{aligned}
K_{71}^{(\beta,\gamma)} &= -K_{72}^{(\beta,\gamma)} = -K_{81}^{(\beta,\gamma)} = K_{82}^{(\beta,\gamma)} = \frac{C_{23}^{(\beta,\gamma)}}{h_\beta} \\
K_{73}^{(\beta,\gamma)} &= K_{74}^{(\beta,\gamma)} = K_{83}^{(\beta,\gamma)} = K_{84}^{(\beta,\gamma)} = -\frac{3C_{33}^{(\beta,\gamma)}C_{44}^{(\beta,\gamma)}l_\gamma}{\bar{C}_{33}^{(\beta,\gamma)}h_\beta^2} \\
K_{77}^{(\beta,\gamma)} &= K_{88}^{(\beta,\gamma)} = \frac{C_{33}^{(\beta,\gamma)}}{l_\gamma}\left(4-3\frac{h_\beta^2 C_{33}^{(\beta,\gamma)}}{l_\gamma^2 \bar{C}_{33}^{(\beta,\gamma)}}\right) \\
K_{78}^{(\beta,\gamma)} &= K_{87}^{(\beta,\gamma)} = \frac{C_{33}^{(\beta,\gamma)}}{l_\gamma}\left(2-3\frac{C_{33}^{(\beta,\gamma)}}{\bar{C}_{33}^{(\beta,\gamma)}}\right)
\end{aligned}
\tag*{C(6)}
$$

The elements of the plastic force vectors are given next:

$$
\begin{aligned}
g_{o1}^{(\beta,\gamma)} &= \frac{C_{66}^{(\beta,\gamma)}}{\bar{C}_{11}^{(\beta,\gamma)}}\left[\sum_{m=1,3,5,\ldots}^{\infty} m'\tau_{21(mo)}^{in(\beta,\gamma)} + \frac{h_\beta}{l_\gamma}\sum_{n=1,3,5,\ldots}^{\infty} n'\tau_{31(0n)}^{in(\beta,\gamma)}\right] - \sum_{m=0}^{\infty} m'\tau_{21(m0)}^{in(\beta,\gamma)} \\
g_{o2}^{(\beta,\gamma)} &= \frac{C_{66}^{(\beta,\gamma)}}{\bar{C}_{11}^{(\beta,\gamma)}}\left[\sum_{m=1,3,5,\ldots}^{\infty} m'\tau_{21(mo)}^{in(\beta,\gamma)} + \frac{h_\beta}{l_\gamma}\sum_{n=1,3,5,\ldots}^{\infty} n'\tau_{31(0n)}^{in(\beta,\gamma)}\right] - \sum_{m=0}^{\infty} (-1)^{m+1}\, m'\tau_{21(m0)}^{in(\beta,\gamma)} \\
g_{o3}^{(\beta,\gamma)} &= \frac{h_\beta C_{55}^{(\beta,\gamma)}}{l_\gamma \bar{C}_{11}^{(\beta,\gamma)}}\left[\sum_{m=1,3,5,\ldots}^{\infty} m'\tau_{21(mo)}^{in(\beta,\gamma)} + \frac{h_\beta}{l_\gamma}\sum_{n=1,3,5,\ldots}^{\infty} n'\tau_{31(0n)}^{in(\beta,\gamma)}\right] - \sum_{n=0}^{\infty} n'\tau_{31(0n)}^{in(\beta,\gamma)} \\
g_{o4}^{(\beta,\gamma)} &= \frac{h_\beta C_{55}^{(\beta,\gamma)}}{l_\gamma \bar{C}_{11}^{(\beta,\gamma)}}\left[\sum_{m=1,3,5,\ldots}^{\infty} m'\tau_{21(mo)}^{in(\beta,\gamma)} + \frac{h_\beta}{l_\gamma}\sum_{n=1,3,5,\ldots}^{\infty} n'\tau_{31(0n)}^{in(\beta,\gamma)}\right] - \sum_{n=0}^{\infty} (-1)^{(n+1)}\, n'\tau_{31(0n)}^{in(\beta,\gamma)}
\end{aligned}
\tag*{C(7)}
$$

$$
\begin{aligned}
g_{i1}^{(\beta,\gamma)} &= \frac{C_{22}^{(\beta,\gamma)}}{\bar{C}_{22}^{(\beta,\gamma)}}\left[\sum_{m=1,3,5,\ldots}^{\infty} m'\tau_{22(mo)}^{in(\beta,\gamma)} + \frac{h_\beta}{l_\gamma}\sum_{n=1,3,5,\ldots}^{\infty} n'\tau_{32(0n)}^{in(\beta,\gamma)}\right] - \sum_{m=0}^{\infty} m'\tau_{21(m0)}^{in(\beta,\gamma)} \\
g_{i2}^{(\beta,\gamma)} &= \frac{C_{22}^{(\beta,\gamma)}}{\bar{C}_{22}^{(\beta,\gamma)}}\left[\sum_{m=1,3,5,\ldots}^{\infty} m'\tau_{22(mo)}^{in(\beta,\gamma)} + \frac{h_\beta}{l_\gamma}\sum_{n=1,3,5,\ldots}^{\infty} n'\tau_{32(0n)}^{in(\beta,\gamma)}\right] - \sum_{m=0}^{\infty} (-1)^{m+1}\, m'\tau_{22(m0)}^{in(\beta,\gamma)} \\
g_{i3}^{(\beta,\gamma)} &= \frac{l_\gamma C_{44}^{(\beta,\gamma)}}{h_\beta \bar{C}_{33}^{(\beta,\gamma)}}\left[\frac{l_\gamma}{h_\beta}\sum_{m=1,3,5,\ldots}^{\infty} m'\tau_{23(mo)}^{in(\beta,\gamma)} + \sum_{n=1,3,5,\ldots}^{\infty} n'\tau_{33(0n)}^{in(\beta,\gamma)}\right] - \sum_{m=0}^{\infty} m'\tau_{23(m0)}^{in(\beta,\gamma)} \\
g_{i4}^{(\beta,\gamma)} &= \frac{l_\gamma C_{44}^{(\beta,\gamma)}}{h_\beta \bar{C}_{33}^{(\beta,\gamma)}}\left[\frac{l_\gamma}{h_\beta}\sum_{m=1,3,5,\ldots}^{\infty} m'\tau_{23(mo)}^{in(\beta,\gamma)} + \sum_{n=1,3,5,\ldots}^{\infty} n'\tau_{33(0n)}^{in(\beta,\gamma)}\right] - \sum_{m=0}^{\infty} (-1)^{(m+1)}\, m'\tau_{23(m0)}^{in(\beta,\gamma)}
\end{aligned}
\tag*{C(8)}
$$

$$
\begin{aligned}
g_{i5}^{(\beta,\gamma)} &= \frac{h_\beta C_{44}^{(\beta,\gamma)}}{l_\gamma \bar{C}_{22}^{(\beta,\gamma)}}\left[\sum_{m=1,3,5,\ldots}^{\infty} m'\tau_{22(mo)}^{in(\beta,\gamma)} + \frac{h_\beta}{l_\gamma}\sum_{n=1,3,5,\ldots}^{\infty} n'\tau_{32(0n)}^{in(\beta,\gamma)}\right] - \sum_{n=0}^{\infty} n'\tau_{321(0n)}^{in(\beta,\gamma)} \\
g_{i6}^{(\beta,\gamma)} &= \frac{h_\beta C_{22}^{(\beta,\gamma)}}{l_\gamma \bar{C}_{22}^{(\beta,\gamma)}}\left[\sum_{m=1,3,5,\ldots}^{\infty} m'\tau_{22(mo)}^{in(\beta,\gamma)} + \frac{h_\beta}{l_\gamma}\sum_{n=1,3,5,\ldots}^{\infty} n'\tau_{32(0n)}^{in(\beta,\gamma)}\right] - \sum_{n=0}^{\infty} (-1)^{n+1}\, n'\tau_{32(0n)}^{in(\beta,\gamma)} \\
g_{i7}^{(\beta,\gamma)} &= \frac{C_{33}^{(\beta,\gamma)}}{\bar{C}_{33}^{(\beta,\gamma)}}\left[\frac{l_\gamma}{h_\beta}\sum_{m=1,3,5,\ldots}^{\infty} m'\tau_{23(mo)}^{in(\beta,\gamma)} + \sum_{n=1,3,5,\ldots}^{\infty} n'\tau_{33(0n)}^{in(\beta,\gamma)}\right] - \sum_{n=0}^{\infty} n'\tau_{33(0n)}^{in(\beta,\gamma)} \\
g_{i8}^{(\beta,\gamma)} &= \frac{C_{33}^{(\beta,\gamma)}}{\bar{C}_{33}^{(\beta,\gamma)}}\left[\frac{l_\gamma}{h_\beta}\sum_{m=1,3,5,\ldots}^{\infty} m'\tau_{23(mo)}^{in(\beta,\gamma)} + \sum_{n=1,3,5,\ldots}^{\infty} n'\tau_{33(0n)}^{in(\beta,\gamma)}\right] - \sum_{n=0}^{\infty} (-1)^{(n+1)}\, n'\tau_{33(0n)}^{in(\beta,\gamma)}
\end{aligned}
\qquad \text{C(9)}
$$

where $m' = \sqrt{(1+2m)}$ and $n' = \sqrt{(1+2n)}$ in the above expressions.

Reference

AASHTO (1998). "Bridge Design Specifications." American Association of State Highway and Transportation Officials, Washington, DC.

Abaqus. “Mohr-Coulomb plasticity,” Section 11.3.3 of the ABAQUS Analysis User's Manual.

ABAQUS (2002). "Theory Manual." Version 6.2, Hibbit, Karlson, and Sorenson.

Aboudi, J. (1989). "Micromechanical Analysis of Composites by The Method of Cells." Appl. Mech. Rev 42(7): 193-221.

Aboudi, J., M. Asme, et al. (2001). "Linear Thermoelastic Higher-Order Theory for Periodic Multiphase Materials." Journal of Applied Mechanics 68: 697.

ACI (1999). "530/ASCE 5/TMS 402-Building Code Requirements for Masonry Structures", American Concrete Institute International.

Anthoine, A. (1995). "Derivation of The In-Plane Elastic Characteristics of Masonry through Homogenization Theory." lnternational Joural of Solid Structures 32(2): 137-163.

Anthoine, A. (1997). "Homogenization of Periodic Masonry: Plane Stress, Generalized Plane Strain or 3d Modelling?" Communications In Numerical Methods In Engineering **13**: 319-326.

ASTM (2000) "Standard Test Method for Compressive Strength of Cylindrical Concrete Specimens." Annual Book of ASTM Standards, Concrete and Aggregates: 18-22.

Atkinson, R. H., Noland, J. L. et al. (1985). "A Deformation Failure Theory for Stack-bond Brick Masonry Prisms in Compression." Proc. 3 rd NAMC, Arlington, Texas.

Azevedo, J., M. Erri, et al. (2000). "Seismic analysis and blocky masonry structure." Earthquake Spectra 16(2).

Bansal, Y. (2005). "Finite Volume Direct Averaging Micromechanics of Heterogeneous Media." University of Virginia, Ph.D. Dissertation.

Bansal, Y. and M. J. Pindera (2006). "Finite-volume Direct Averaging Micromechanics of Heterogeneous Materials with Elastic–plastic Phases." International Journal of Plasticity 22(5): 775-825.

Bazant, Z. P. and F. Lin (1988). "Non-local yield limit degradation." International journal for numerical methods in engineering 26(8): 1805-1823.

Bevington, P. R. (1969). "Data Reduction and Error Analysis for the Physical Sciences 1McGraw-Hill." New York.

Binda, L., A. Fontontana, et al. (1988). "Mechanical Behavior of Brick Masonries Derived from Unit and Mortar Characteristics." Proc. 8th Int. Brick and Block Masonry Conf., eds. J.W. de Courcy, Elsevier Applied Science, London, UK,: 205-216.

Binda, L., Mirabella, R. G., et al. (1996). "Measuring Masonry Material Properties." Abrams, Daniel P., ed.

CEN (1995). Eurocode 6: Design of masonry structures,ENV 1996-1-1. Brussels, Belgium.

Chandler, A. M. and P. A. Mendis (2000). "Performance of reinforced concrete frames using force and displacement based seismic assessment methods." Engineering Structures **22**(4): 352-363.

Chen, W. F. and A. F. Saleeb (1994). Constitutive equations for engineering materials, Elsevier New York.

Chopra, A. K. (2001). "Dynamics of structures." Prentice Hall, New Jersey.

Consultants, G. (1995). Seismic investigation of the Bronx Whitestone Bridge, Brinckerhoff Quade & Douglas, Inc./Imbsen Consulting Engineer, A Joint Venture.

Cundall, P. A. (1971). "A Computer Model for Simulating Progressive Large Scale Movements in Blocky Rock Systems." Proceedings of the Symposium of the International Society of Rock Mechanics 1: 2-8.

Cundall, P. A. (1979). "A discrete numerical model for granular assemblies." Geotechnics 29(1): 47-65.

Desai, C. S. and H. J. Siriwardane (1984). "Constitutive Laws for Engineering Materials with Emphasis on Geologic Materials." New Jersey, PrenticeHall, Englewood Cliffs: 344-403.

Dhanasekar, M., Page, A. W., et al. (1985). "The Failure of Brick Masonry under Biaxial Stresses." Proceedings Institution of Civil Engineers. 2(79): 295-313.

Dhanasekar, M., P. W. Kleeman, et al. (1985). "Biaxial stress-strain relations for brick masonry." J. Struct. Div. ASCE 111: 1083-1100.

Eberhardt, E., Stead,D., et al. (1999). "Quantifying progressive pre-peak brittle fracture damage in rock during uniaxial compression." International Journal of Rock Mechanics and Mining Sciences 36(361): 380.

Fairhurst, C. E. and Hudson, J. A. (1999). "Draft ISRM Suggested Method for the Complete Stress-Strain Curve for Intact Rock in Uniaxial Compression." International Journal of Rock mechanics and mining sciences (1997) 36(3): 279-289.

Fajfar, P. and H. Krawinkler (2004). "Performance-based seismic design concepts and implementation." Proceedings of the international workshop.

FEMA (1997). "NEHRP guidelines for the seismic rehabilitation of buildings,." FEMA 273, Federal Emergency Management Agency, Washington, D.C.

FEMA (2000). "Prestandard and commentary for the seismic rehabilitation of buildings." FEMA 356, Federal Emergency Management Agency,Washington, D.C.

Femlab, V. (2004). "3.1. COMSOL." Inc., Burlington, MA, USA.

Ganz, H. R. and B. Thurlimann (1982). "Tests on the biaxial strength of masonry." Report No. 7502 3.

Guggisberg, R. and B. Thurlimann (1987). Experimental Determination of Masonry Strength Parameters, Report No. 7502-5, Institute of Structural Engineering, ETH Zurich, Zurich, Switzerland.

Hall, J. F. (1995). "Northridge Earthquake Reconnaissance Report." Earthquake Spectra 11(1 Supplement C): 523.

Hendry, A. W., B. P. Sinha, et al. (1981). An introduction to loading bearing brickwork design. UK, Ellis Horwood.

Hibbitt, K. and I. Sorensen (2002). "ABAQUS Theory Manual." User Manual and Example Manual, Version 6(3).

Hill, R. (1950). The Mathematical Theory of Plasticity, Oxford University Press.

Hilsdorf, H. K. (1969). Investigation into the failure mechanism of brick masonry loaded in axial compression, in: Designing, engineering and constructing with masonry products. Houston, Texas, Gulf Publishing Company.

Idriss, I. M. (1996). "Study of seismic hazard at John F." Kennedy Airport, Prepared for the New Jersey and New York Port Authorities.

Jacob, K., S. Horton, et al. (1996). "Seismic retrofit study of the Queensboro Bridge, NY: rock motions and mode ID by ambient vibration measurements." Proc. Eleventh World Conference on Earthquake Engineering [Proceedings], Pergamon, Elsevier Science Ltd., [Oxford, England], Disc **3**.

Jones, R. M. (1999). Mechanics of Composite Materials, Taylor & Francis.

Jukes, P. and J. R. Riddington (1997). "A review of masonry joint shear strength test methods." Masonry International, 11(2): 37-41.

Klingner, R. E. and P. M. Ferguson. (2006). "Performance of Masonry in the Northridge Earthquake., http://www.cement.org/masonry/pp_wind_northridge.asp.

Klopp, G. M. and M. C. Griffith (1994). "The earthquake design of unreinforced masonry structures in areas of low seismic risk." Proc., 3rd National Masonry Seminar, Queensland University of Technology, Brisbane, Australia: 19.1-19.9.

Lajtai, E. Z. (1998). "Microscopic Fracture Processes in a Granite." Rock Mechanics and

Rock Engineering 31(4): 237-250.

Lankulovski, E. and S. Parsanejad (1994). "Earthquake resistance assessment of masonry buildings." Proc., 3rd National Masonry Seminar, Queensland University of Technology, Brisbane, Australia: 16.1-16.12.

Larovere, H. (1990). "Nonlinear analysis of reinforced concrete masonry walls under simulated seismic loadings." PhD thesis, University of California, San Diego, Califonia.

Lemos, J. V. (1995). "Assessment of the Ultimate Load of a Masonry Arch Using Discrete Elements." 3rd International Symposium on Computer Methods in Structural Masonry ,Lisbon, Portugal.

Lemos, J. V., R. D. Hart, et al. (1985). "A Generalized Distinct Element Program for Modeling Jointed Rock Mass." Proceedings of the International Symposium on Fundamentals of Rock Joints: 335-343.

Lin, F. B., G. Yan, et al. (2002). "Nonlocal strain-softening model of quasi-brittle materials using boundary element method." Engineering Analysis with Boundary Elements 26(5): 417-424.

Lofti, H. R. and P. B. Shing (1994). " Interface model applied to fracture of masonry structures." J. Struct. Eng., ASCE 120(1): 63-80.

Loo, Y. C. and Y. Yang (1991). "Cracking and failure analysis of masonry arch bridges." Journal of Structural Engineering 117(6): 1641-1659.

Lorig, L. J. (1984). "A Hybrid Computational Model for Excavation and Support Design in Jointed Media." Ph.D. Thesis, University of Minnesota.

Lotfi, H. R. and P. B. Shing (1994). " Interface model applied to fracture of masonry structures." J. Struct. Eng., ASCE 120(1): 63-80.

LourencI o, P. (1996). Computational strategies for masonry structures, Technische Universiteit Delft.

Luciano, R. and Sacco, E. (1997). "Homogenization technique and damage model for old masonry material." International Journal of Solids and Structures 34(24): 3191-3208.

Lourenco, P. B., J. G. Rots, et al. (1998). "Continuum model for masonry: Parameter estimation and validation." J. Struct. Eng., ASCE 124(6): 642-652.

Lurati, F., H. Graf, et al. (1990). "Experimental Determination of the Strength Parameters of Concrete Masonry." Report No. 8401-2, Institute of Structural Engineering, ETH Zurich, Zurich, Switzerland.

Ma, G., H. Hao, et al. (2001). "Homogenization Of Masonry Using Numerical Simulations." Journal of Engineering Mechanics: 421-431.

McNary, W. S. and Abrams, D. P. (1985). "Mechanics of Masonry in Compression." Journal of Structural Engineering 111(4): 857-870.

Mann, W. and M. Betzler (1994). "Investigations on the Effect of Different Forms of Test Samples to Test the Compressive Strength of Masonry." 10th International Brick and Block Masonry Conference, Calgary: 1305-13.

Mann, W. and H. Muller (1982). Failure of shear-stressed masonry - an enlarged theory, tests and application to shear walls. Proc. British Ceramic Society.

Meguro, K., F. Uehan, et al. (2004). "Damage to Masonry Structures." Retrieved 12/10, 2004, from http://www.st.hirosaki-u.ac.jp/~tamao/Gujarat/web/Gujarat_7_3.pdf.

Mendelson, A. (1983). Plasticity: Theory and Application, Krieger Pub Co.

Molins, C. and P. Roca (1998). "Capacity of masonry arches and spatial frames." Journal of Structural Engineering (ASCE) 124(6): 653-663.

NEHRP (2000). "NEHRP Recommended Provisions for Seismic Regulations for New Buildings and Other Structures." Report FEMA 368.

Ng, K. N., C. A. Fairfield, et al. (1991). "Finite element analysis of masonry arch bridges." Proc. Inst. Civ. Eng., Struct. Build. 134: 119-127.

NYCDOT (1998). "Seismic Design Criteria Guideline." New York City Department of Transportation.

Owen, D. R. J. and E. Hinton (1980). Finite elements in plasticity, Pineridge Press Swansea, UK.

Page, A. W. (1978). "Finite element model for masonry." J. Struct. Div., ASCE **104**(8): 1267-1285.

Page, A. W. (1981). "The Biaxial Compressive Strength of Brick Masonry." Proc. Instn. Civ. Engrs., **2**(71): 893-906.

Page, A. W. (1983). "The strength of brick masonry under biaxial compression-tension." International Journal of Masonry Construction **3**(1): 26-31.

Paley, M. and Aboudi, J. (1992). "Micromechanical Analysis of Composites by the Generalized Cells Model." Mechanics of Materials (The Netherlands) 14(2): 127-139.

Panantonopoulos, D., I. Psycharis, et al. (1998). "Predictability of experiments on the seismic response of classical monuments." Proc. 11th European conf . on Earthquake Eng., Balkema, Paris.

Pande, G. N., J. X. Liang, et al. (1989). "Equivalent Elastic Moduli for Brick Masonry." Comp. Geotec. 8: 243-265.

Papa, E. (1996). "A Unilateral Damage Model for Masonry Based on a Homogenisation Procedure." Mechanics of Cohesive - frictional Materials 1(4): 349-366.

Pietruszczak, S. and X. Niu (1991). "A Mathematical Description of Macroscopic Behavior of Brick Masonry." International Journal Solids Structures 29(5): 531-546.

Plesha, M. E. and E. C. Aifantis. (1983). "On the Modeling of Rocks with Microstructure." Rock Mechanics — Theory-Experiment-Practice,Proceedings of the 24th U.S. Symposium on Rock Mechanics, Texas A&M University: 27-35.

RILEM (1994). "Technical recommendations for the testing and use of constructions materials:LUMA1 - Compressive strength of masonry units." Chapman & Hall, UK.

Roca, P., Oliveira, D., et al. (2001). "Mechanical Response of Dry Joint Masonry." Studies in ancient structures, Yildiz Teknik Universitesi, Istanbul: 571-579.

Rots, J. G. (1991). "Numerical Simulation of Cracking in Structural Masonry." Heron 36(2): 49-63.

Saadeghvaziri, M. A. and S. S. Metha (1993). "An analytical model for URM structures." Proc. 6th North American Masonry Conf., Philadelphia, USA: 409-418.

Samarasinghe, W. (1980). "The in-plane failure of brickwork" , PhD thesis, University of Edinburgh, Edinburgh, U.K.

Sarangapani, G., V. Reddy, B. V., et al. (2005). "Brick-Mortar Bond and Masonry Compressive Strength." Journal of Materials in Civil Engineering 17(2): 229-237.

Shabawi, A. and T. Verdel (1995). "Failure modes of old masonry walls and arches under seismic loading." European Seismic Design Practicem Elnashai(ed.), Balkema, Totterdam: 463-468.

So, J. and Leissa, A. W. (1997). "Free Vibrations of Thick Hollow Circular Cylinders From Three-Dimensional Analysis." Journal of Vibration and Acoustics 119: 89.

Subramaniam, K. V., Popovics, J. S., et al. (2001). "Determining Elastic Properties of Concrete Using Vibrational Resonance Frequencies of Standard Test Cylinders." the American Society for Testing and Materials: 81-89.

Sutton, M. A., Wolters, W. J., et al. (1983). "Determination of Displacements Using an Improved Digital Correlation Method." Image Vision Computing 1(3): 133-139.

Tomazevic, M., M. Lutman, et al. (1996). "Seismic behavior of masonry walls: experimental simulation." J. Struct. Enrg., ASCE 122(9): 1040-1047.

Vermeltfoort, A. T. (1997). Effects of the width and boundary conditions on the mechanical properties of masonry prisms under compression. Proc. 11th Int. Brick/Block Masonry Conference, Shangai.

Vratsanou, V. (1991). "Determination of the behaviour factors for brick masonry panels subjected to earthquake actions." Proc., Int. Conf. on Soil Dyn. and Earthquake Engrg., Computational Mechanics Publ., Southampton, England: 565-575.

Weidlinger Associates, P. C. (1996). "Brick masonry testing report-main bridge approach arches".

Weidlinger Associates, P. C. (1998). "New York City Seismic Hazard Study and Its Engineering Applications." Prepared for New York City Department of Transportation.

Wesche, K. and A. Ilantis (1980). "General Recommendations for Methods of Testing Load Bearing Walls." Materials and Structures 13(78): 433-445.

Wu, C. and H. Hao (2006). "Derivation of 3D masonry Properties Using Numerical Homogenization Technique." International Journal For Numerical Methods In Engineering 66(11): 1717.

Zeng, F. and Lin, F. B. (2009). "Elastic-plastic Modeling of Masonry Structure via Micromechanics Approach." in preparation.

Zeng, F., F.-B. Lin, and K. Subramanium et al. (2009). "Experimental Investigation on Granite Masonry Behavior under Compression." ASCE Structures Congress , Austin.

List of Publications

---

1. Fei Zeng, Feng-Bao Lin and Kolluru V. Subramaniam, “Experimental Investigation and Homogenization Modeling of Granite Masonry”, Submitted to ACI Materials Journal.

2. Fei Zeng, Feng-Bao Lin and Kolluru V. Subramaniam, “Experimental Investigation on Granite Masonry under Compression”, Proceedings of the SEI 2009 Structures Congress, Texas, May 2009.

3. Fei Zeng and Feng-Bao Lin, “Modeling and Analysis of Unreinforced Masonry Structure for Seismic Assessment”, Proceeding of the 15th U.S. National Congress of Theoretical and Applied Mechanics, Colorado, June, 2006.

4. Fei Zeng and Feng-Bao Lin, “Homogenized Modeling of Masonry Structure via Micromechanics Approach”, in preparation.

5. Fei Zeng and Feng-Bao Lin, “Seismic Assessment and Retrofit of Unreinforced Masonry Structrue”, 7th Annual Celebration of Science, Mathematics, and Engineering, Graduate Center of the City University of New York, April, 2006.

6. Fei Zeng and Feng-Bao Lin, “Ultrasonic Characterization of Microstructure for High Purity Metals”, 195-196, the Junior Scientist Conference 2006, Vienna, Austria, April 2006.

7. Fei Zeng, Sean R. Agnew, and Ganapati R. Myneni, “Ultrasonic Attenuation Due to Grain Boundary Scattering in Pure Niobium”, The Journal of NDE, in publication.

8. Sean R. Agnew, Fei Zeng, and Ganapati R. Myneni, “Ultrasonic Velocity and Texture of High RRR Niobium”, Materiaux et Techniques, No. 7-8-9: 38-44, 2003.

9. Fei Zeng, Shisheng Hu and Yi Pan, “Evaluation of Cushioning Properties and Energy-absorption Capability of Foam Aluminum”, Explosion and Shock Waves, Vol.22, No. 4: 358-362, 2002.